Characterizing and Modelling Tailings Hydrogeochemistry Under a Composite Cover at the Abandoned Kam Kotia Mine, ON

by

Aria (Tingxian) Zhang

A thesis

presented to the University of Waterloo

in fulfillment of the

thesis requirement for the degree of

Master of Science

in

Earth Sciences - Water

Waterloo, Ontario, Canada, 2022

Author’s Declaration

I hereby declare that I am the sole author of this thesis. This is a true copy of the thesis, including any required final revisions, as accepted by my examiners.

I understand that my thesis may be made electronically available to the public.

Abstract

A principal environmental concern associated with mining is the weathering of mine waste in the presence of oxygen and water that generates acid mine drainage (AMD) concentrated in toxic elements. Installation of composite covers on mine waste is a remedial option to prevent the generation of AMD. Consisting of layers of materials of contrasting grain sizes, composite covers can inhibit oxygen and water ingress. Despite extensive studies on the design of composite covers, there is limited information available on the field performance of composite covers on legacy tailings. This thesis investigates the hydrogeochemistry of a legacy tailings impoundment remediated with a five-layer composite cover in 2008 and evaluates the long-term field performance of the cover. To investigate the hydrogeology and gas transport processes in the cover and tailings, groundwater flow, vadose zone hydrology, stable water isotopes, and pore-gas concentrations were monitored over multiple years, and numerical modelling of the variably saturated flow and calculations of gas flux were conducted. To characterize the geochemistry and mineralogy of the tailings under the composite cover, pore-water and groundwater sampling and geochemical analysis, selective chemical extractions, optical and electron microscopic study of thin sections, and synchrotron-based X-ray absorption spectroscopy experiments were conducted. To quantitatively assess the hydrogeochemical processes in the tailings from deposition to remediation by a composite cover, 1-D reactive transport simulations were implemented using the multi-component reactive transport code MIN3P. Characterization and modelling of the cover hydrogeology and gas transport indicate that during the summer, fall, and spring, the capillary barrier effect of the cover functioned well. The clay maintained saturation except for temporary desiccation during summer droughts. Potential local cover defects enabled oxygen advection into the tailings at one out of three monitoring locations. A seasonal change in the hydrology of the cover system occurred in the spring when snowmelt infiltrated deep into the tailings and reduced both oxygen diffusion and advection via cover defects, resulting in depleted pore-gas oxygen concentrations. Overall, the cover was effective in reducing infiltration and oxygen flux into the tailings. Mineralogical studies suggest that due to the high pyrite content (up to 74 wt%), sulfide oxidation depleted pyrites to a depth of 0.1-0.25 m. Aqueous geochemical results suggest that at one monitoring

location, the cover reduced AMD generation and improved pore-water quality. The presence of a peat layer rich in organic carbon below the tailings facilitated sulfate reduction, albeit limited in capacity. In contrast, at another monitoring location, potential cover imperfections facilitated continued sulfide oxidation, resulting in low pore-water pH and elevated aqueous concentrations of sulfate, Fe, Zn, Cu, and As. Crystalline oxyhydroxides are a major sink for trace elements and may release them through desorption, acidic dissolution, and potential reductive dissolution under strongly reducing conditions. The complex geochemical processes indicate that sulfate, As, Zn, and Mn may remain long-term contaminants of concern. 1-D reactive transport simulations that incorporated transient infiltration, post-cover hydrogeochemical changes, a dynamic temperature regime, sulfide-mineral oxidation, acid neutralization, secondary-mineral precipitation, and sorption processes resulted in good agreement with the field results. Simulated temporal changes in reaction rates and geochemical parameters indicate that where intact, the cover lessened sulfide oxidation by both oxygen and Fe(III) and improved pore-water quality over time. Sulfate, Zn, and As persisted regardless of cover performance, whereas Cu and Al were the most sensitive to cover imperfections. The combined results from hydrogeochemical characterization and modelling suggest that even though the composite cover was effective in controlling infiltration and oxygen transport a decade after placement, complex geochemical processes in legacy tailings resulted in the persistence of deteriorated water quality and several elements may remain of long-term concern. This study can provide insight into cover design and mine remediation.

Acknowledgements

This study was funded by Natural Sciences and Engineering Research Council of Canada Strategic Partnership Grants for Networks, Toward Environmentally Responsible Resource Extraction Network (NSERC-TERRE-NET, NETGP 479708-15, D.W. Blowes, Principal Investigator), Ontario Research Fund, and an NSERC Alexander Graham Bell Canada Graduate Scholarship-Master's (CGS M), award to the author. The author thanks the Ontario Ministry of Northern Development, Mines, Natural Resources and Forestry (NDMNRF) for the logistic support. This research used resources of the Advanced Photon Source, a U.S. Department of Energy (DOE) Office of Science user facility operated for the DOE Office of Science by Argonne National Laboratory under Contract No. DE-AC02-06CH11357. Part of the research was performed at the Canadian Light Source, a national research facility of the University of Saskatchewan, which is supported by the Canada Foundation for Innovation (CFI), NSERC, the National Research Council (NRC), the Canadian Institutes of Health Research (CIHR), the Government of Saskatchewan, and the University of Saskatchewan.

The author would like to acknowledge the following individuals from the Groundwater Geochemistry and Remediation (GGR) group at the University of Waterloo (UW) and external partners for their generous assistance on this project: fieldwork training and support - Jeff Bain, Remi Boucher (NDMNRF), Alexei Tarnopolski, David Wilson, Lisa Kester, Emily Dodsworth, Nikita van Loon, Hannah Starzynski, and Yizhi Yuan; laboratory analyses - Jeff Bain, Sara Fellin, Joy Hu, and Michael Forte; mineralogical characterization - Majak Agau, Zhongwen Bao, David Hilger, Shuhuan Li (UW Ecohydrology), and Emily Saurette; synchrotron experiments: Alana Ou Wang, Liana Smith, Hannah Starzynski, Debora Meira (APS), Mohsen Shakouri (CLS), Qunfeng Xiao (CLS), and Alisa Paterson (CLS); reactive transport modelling – Andrea Brookfield (UW) and David Wilson.

The author appreciates the invaluable advice and guidance provided by the supervisors David W. Blowes and Carol J. Ptacek throughout the research, as well as advice from thesis committee members Walter Illman (UW) and Richard Amos (Carleton University).

Table of Contents

List of Figures

List of Tables

List of Symbols

θ_w volumetric water content

θ_a volumetric air content

Ψ matric suction

ψ pressure head

h hydraulic head

ϕ porosity

S water saturation

ρ_p particle density

ρ_b dry bulk density

d_{10}, d_{60} effective particle diameters

C_u uniformity coefficient

K hydraulic conductivity

K_{sat}: saturated hydraulic conductivity

θ_r residual volumetric water content

θ_s saturated volumetric water content ($=\phi$)

α, n van Genuchten (1980) parameters for water retention curves

D_e: effective O_2 diffusion coefficient

K_r pyrite oxidation rate coefficient

F: gas flux

C_p pyrite weight fraction

H Henry's Law coefficient

Chapter 1
Background and introduction

1.1 Research background

The long history of mining in Canada resulted in more than 10,000 abandoned mines (Mackasey 2000), around 6,000 of which are in Ontario (Hamblin 2003). Contamination of groundwater and surface water by acid mine drainage (AMD) is among the most severe environmental concerns associated with abandoned mines. Acid mine drainage originates from the oxidation of sulfide minerals in mine wastes in the presence of O_2 and water. The series of complex reactions of pyrite oxidation can be simplified as (Blowes et al. 2014):

$$FeS_2 + 15/4\ O_2 + 7/2\ H_2O \rightarrow Fe(OH)_3 + 2H_2SO_4 \qquad \text{(eq. 1-1)}$$

Under acidic conditions such as those observed in oxidized tailings, ferric ions can more readily oxidize sulfide minerals with the mediation of acidophilic bacteria (Blowes et al. 2014).

AMD mitigation remains a technical challenge at mine sites, especially at old mines where AMD has occurred for decades. For abandoned and orphaned mines, AMD remediation is estimated to cost tens of billions of dollars in North America (INAP 2012). In addition to complex site characteristics and biogeochemical processes, a lack of funding for abandoned and orphaned sites further confounds their remediation.

Several mitigating and remedial techniques exist to reduce the availability of O_2 and water in eq. 1-1 to lower AMD generation. Among them, composite covers are a potential option for decreasing rates of water infiltration and O_2 flux into the underlying wastes. In a multi-layer cover system, a layer of fine-grained low-permeability material, such as clay and silt, with a high degree of saturation, or a geomembrane, acts as a barrier to O_2 and water ingress. A low-permeability layer can be placed between layers of coarse-grained material, such as sand and gravel, to maximize capillary barrier effects (Nicholson et al. 1989, Aubertin et al. 2009).

A typical target of O_2 flux is ≤ 50 g m^{-2} yr^{-1} to prevent AMD production in fresh tailings (MEND 1999). Gas transport processes include convection, advection, aqueous dissolution, and adsorption (Aubertin et al. 2000). Kim and Benson (2004) calculated that gas diffusion

represents 99% of total O_2 flux at steady state with an advection-diffusion model, whereas Binning et al. (2007) demonstrated that gas advection accounts for 23% of total O_2 flux at steady state if O_2 consumption occurs without CO_2 generation. Most previous studies on soil and cover systems assumed that advection is negligible and diffusion is the dominant process in porous media and cover systems (Kimball and Lemon 1971, Collin and Rasmuson 1988, Nicholson et al. 1989, Aubertin et al. 2000, Mbonimpa et al. 2003, Aachib et al. 2004). Gas diffusion can occur in both air and water, but it is more rapid in air-filled pores than in water-filled pores (Aubertin et al. 2000).

One potential geochemical concern of placing covers on oxidized tailings is the remobilization of trace elements previously sequestered in secondary minerals. A change in the water balance of the site caused by the cover can result in the dissolution or precipitation of water-soluble minerals (Holmström et al. 2001). Covers can also increase the pH via a decrease in AMD production, which can cause desorption of trace metal(loid)s from (oxy)hydroxides, especially oxyanions. A shift to more reducing redox conditions caused by the cover can cause reductive dissolution of Fe(III) (oxy)hydroxides, which has been demonstrated in field studies (*e.g.*, Lovley et al. (1989), McCreadie et al. (2000)). Although reductive dissolution of Fe(III) oxides in unremediated oxidized tailings under a cover was proposed (Ribet et al. 1995, Gunsinger et al. 2006), it has not been field-verified.

Despite a large body of research on the design and performance of composite covers (MEND 2004), most studies focused on unoxidized tailings, whereas few studies examined their application to old tailings that were subjected to oxidation (Pabst et al. 2017, 2018). Moreover, the existing studies are all laboratory-based and there is a lack of field-based studies. Additionally, characterization of the tailings geochemistry and mineralogy have not been conducted for AMD-producing tailings under a composite cover.

1.2 Site descriptions

The study site is the abandoned Kam Kotia mine, a former Cu and Zn mine located 20 km northwest of Timmins, Ontario (Figure 1-1). The site is characterized by a continental climate with a typical annual temperature range of -23°C to 24°C and annual precipitation of approximately 835 mm, according to measurements at a weather station in Timmins airport 17 km east of the site from 1981 to 2010 (Environment and Climate Change Canada 2021).

The mine operated from 1942 to 1972, after which it was abandoned without rehabilitation, leaving behind 6 million tonnes of tailings covering over 500 hectares of land. Over the decades, the tailings have oxidized considerably, resulting in the production of AMD with a drainage pH of around 2.3 (SENES Consultants Ltd. et al. 2000). North Impounded Tailings (NIT) was one of the three tailings deposition areas at the mine (Figure 1-1). Most of the NIT tailings overlie an unconfined quaternary sand aquifer, while in some areas the tailings directly overlie bedrock outcrops. Since the unconfined sand aquifer is in direct contact with the tailings, AMD in the tailings migrated to the unconfined aquifer and resulted in a fully developed plume. Topography alteration by mining activities led to hydraulic head built-up at NIT, causing acidic mine-impacted waters to migrate in all directions (SENES Consultants Ltd. et al. 2000). The unconfined aquifer pinches out to the south as well as northeast of NIT, resulting in the discharge of AMD-impacted groundwater to surface seeps, ponds, bogs, and rivers (SENES Consultants Ltd. et al. 2000).

In 2001, the Ontario Ministry of Ministry of Northern Development, Mines, Natural Resources and Forestry (NDMNRF) began a five-stage rehabilitation project at the site. As a part of the rehabilitation, a composite cover with a geosynthetic clay liner (GCL) layer was placed on the NIT in 2008 (Hamblin 2008). From top to bottom, the cover consists of sand, clay, GCL, sand, and waste rock (Figure 1-2).

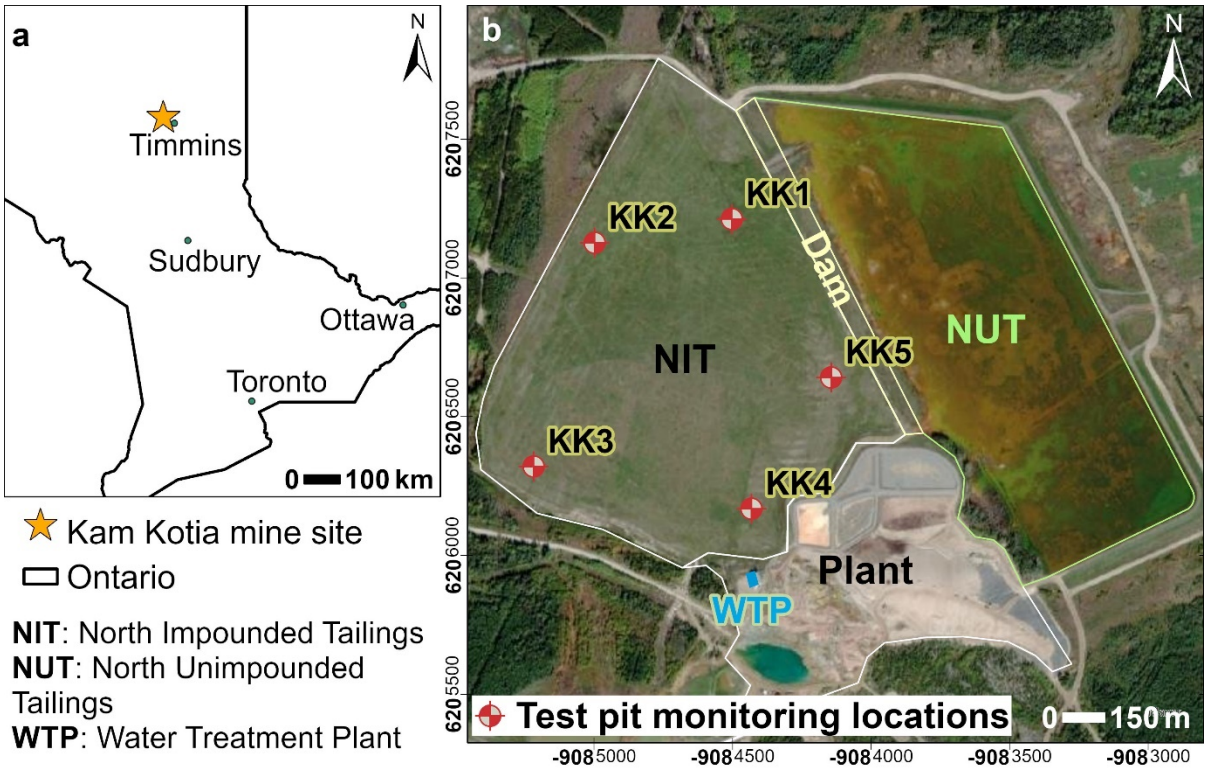

Figure 1-1. (a) Location of Kam Kotia mine. (b) Aerial image of the mine site including NIT and five test pits excavated in 2017 at NIT.

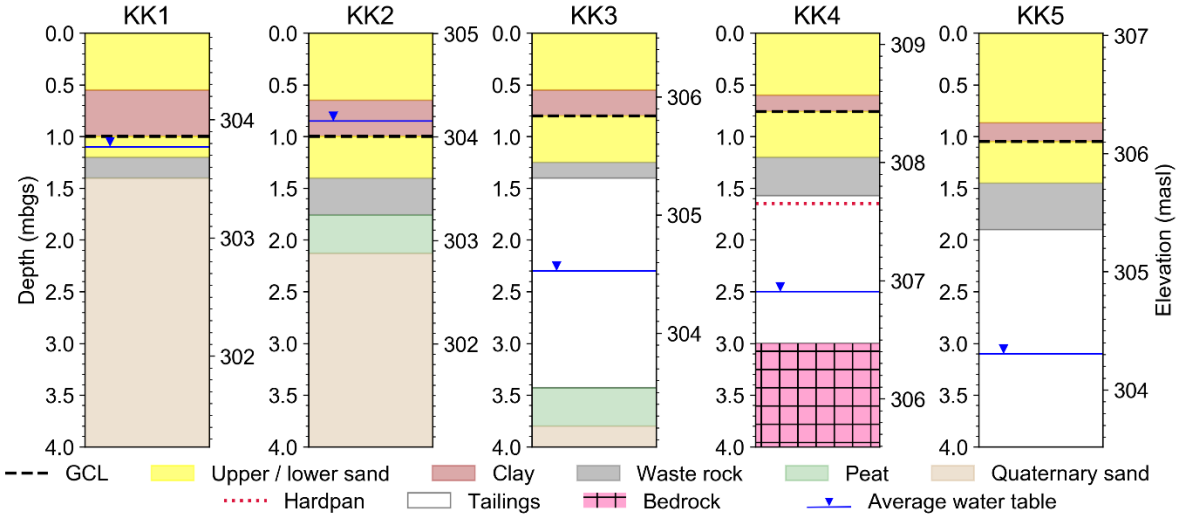

Figure 1-2. Cross-sectional lithology of five test pits at NIT with the composite cover.

1.3 Summary of previous research activities

Field and laboratory characterization studies have been conducted at the Kam Kotia mine site since 2017 as reported by Schmall (2020) and summarized in Table 1-1. Five test pits were excavated in September 2017 across the NIT. Cores were collected for selected depths of covers and tailings using the piston coring method (Starr and Ingleton 1992). Piezometer nests below the water table and lysimeters (soil water solution samplers (SWSS)) above the water table were installed at various depths to provide samples of groundwater and pore water. Gas-sampling ports at 10 cm intervals were installed to facilitate pore-gas sampling. Each port consists of a polyethylene tube that extends to the surface and is separated from the ports above and below it with bentonite.

Four test pits (KK1, KK3, KK4, and KK5) were instrumented with soil moisture sensors (5TE-ECH_2O; METER Group, Ltd.) at different depths of the vadose zone to continuously monitor soil moisture content, temperature, and electrical conductivity (EC) year-round at 2-hour intervals. Jet-filled soil moisture tensiometers (Soilmoisture Equipment Corp.) were also installed at different depths of the vadose zone to continuously monitor matric suction at 30-minute intervals during summer and fall since freezing conditions would damage tensiometers. Instruments were wired to data loggers (Data Dolphin, Optimum Instruments Inc.).

Four rounds of water sampling were completed in October 2017, May, July, and September 2018. Water levels from piezometers were recorded. Water samples were subjected to field measurements of pH, Eh, EC, and alkalinity as well as analyses of major and trace cations, major anions, stable water isotopes ($\delta^{18}O$ and $\delta^{2}H$), dissolved organic carbon (DOC), and $\delta^{13}C$ (DIC). Two rounds of gas sampling were completed in July and September 2018 to determine O_2 and CO_2 concentrations.

Cores were frozen and split into 20-30 cm sections before laboratory sampling. Mineralogical and elemental composition analyses include C/S analysis using an Eltra CS-2000 carbon/sulfur analyzer, X-Ray Fluorescence (XRF) using a Siemens SRS 3000 sequential X-ray fluorescence spectrometer, and X-ray diffraction (XRD) using a Siemens

D500 X-ray diffractometer at the United States Geological Survey (USGS) laboratory in Boulder, Colorado

Microbiological studies, including Most Probable Number (MPN) and 16S rRNA gene sequencing, were previously published (Pakostova et al. 2020). Microbiological data indicate that the cover has reduced the activity of sulfide-oxidizing microorganisms (Pakostova et al. 2020).

Table 1-1. Summary of previous research activity conducted by Schmall (2020), the results of which were included in the present thesis.

Type	Detail
Field instrumentation	Piezometers, lysimeters, soil moisture sensors, tensiometers, and gas ports instrumented in Fall 2017
Sampling	Groundwater monitoring, aqueous and pore-gas sampling between 2017 and 2018, and cored samples of tailings and cover collected in 2017
Laboratory characterization	C/S, X-ray diffraction (XRD) and X-ray fluorescence (XRF) analysis of tailings samples

1.4 Research objectives

The overall objective of the proposed study is to evaluate the long-term performance of the composite cover with GCL at NIT of Kam Kotia Mine, which involves characterization and modelling of hydrogeochemistry.

One hypothesis of the study is that the composite cover lessens sulfide oxidation reaction by reducing O_2 ingress and water infiltration. This hypothesis was evaluated by collecting data on the following: 1) pore-gas concentrations, 2) physical properties of the cover and tailings that affect water and gas transport, 3) aqueous geochemistry of the cover and tailings, 4) the extent of sulfide oxidation in the tailings via mineralogical studies, and 5) simulated reaction rates from reactive transport modelling.

A second hypothesis is that the composite cover destabilizes secondary-mineral phases, such as Fe(III) oxyhydroxides, which affects the mobility of adsorbed and co-precipitated

metal(loid)s. This hypothesis was evaluated by the following: 1) aqueous geochemical conditions, i.e., pH and redox conditions, in the tailings, 2) secondary minerals and association of metal(loid)s via mineralogical studies, 3) susceptibility of secondary phases and metal(loid) to remobilization via selective chemical extractions; and 4) simulated elemental concentration changes from reactive transport modelling.

1.5 Thesis organization

This thesis is organized into three research chapters. Chapter 2 characterizes and models the variably saturated hydrogeology and gas transport in the cover and the underlying tailings. Chapter 3 examines the aqueous and solid-state geochemistry and mineralogy of the tailings under the composite cover. Chapter 4 focuses on using reactive transport simulations to quantitatively assess relevant hydrogeochemical processes.

Chapter 2
Seasonal hydrogeology and gas transport patterns in a composite cover on legacy tailings

2.1 Summary

A five-layer composite cover consisting of sand, clay, geosynthetic clay liner, and waste rock was implemented on legacy tailings in northern Ontario, Canada in 2008 to reduce the production of acid mine drainage. To evaluate the effectiveness of the cover in reducing water and O_2 ingress, groundwater and vadose zone hydrology monitoring, physical property characterization, stable water isotope analysis, pore-gas measurements, O_2 flux calculations, and variably saturated flow modelling were conducted. Investigations reveal that the clay stayed nearly saturated except for temporary desiccation during summer dry periods. During the summer, fall, and winter, the capillary barrier effect of the cover functioned well and inhibited infiltration. Compared to uncovered tailings, the cover significantly lowered diffusive O_2 flux. Atmospheric pore-gas O_2 concentrations at one out of three monitoring locations indicate potential cover imperfections that enabled O_2-gas advection into the tailings. In the spring and early summer, snowmelt infiltration resulted in a perched water table, lateral drainage, and breakthroughs in the capillary barrier effect. The resulting increase in water saturation in the cover limited both O_2-gas diffusion and advection. The seasonal pattern suggests that the composite cover was overall effective in reducing O_2 and water ingress a decade after placement.

2.2 Introduction

2.2.1 Covers for mine waste remediation

Mine waste generated from mining activities can lead to undesirable environmental effects. Among them, the contamination of groundwater and surface water by acid mine drainage (AMD) is a principal concern. Acid mine drainage results from the oxidation of sulfide minerals in mine waste in the presence of O_2 and water.

Covers are a common option for mine waste remediation to reduce water and O_2 availability for sulfide oxidation. Fine-grained low-permeability material with a high degree of

saturation can serve as a good water infiltration barrier. Typical low-permeability materials include clay, silt, and geomembranes (MEND 2004, Aubertin et al. 2016). This low-permeability layer can be placed between layers of coarse-grained material to capitalize on the capillary barrier effect to further enhance the moisture retention capacity of the fine-grained layer (Nicholson et al. 1989, Aubertin et al. 2009). The capillary barrier effect occurs when high capillary tension in the fine-grained material limits downward movement of water into the underlying coarse-grained material. Capillary barriers are most effective when the coarser-grained layers remain unsaturated and non-conductive. In addition, having a coarse-grained layer above the low-permeability layer can reduce water loss due to evapotranspiration and protect against freeze-thaw (Benson et al. 1995, Stormont and Anderson 1999).

Gas transport mechanisms in the subsurface include advection driven by gas-pressure gradients, diffusion driven by concentration gradients, convection driven by heat-induced density differences, aqueous dissolution, adsorption, and non-Darcian turbulent flow (Aubertin et al. 2000, Webb 2006, Amos et al. 2015). Adsorption and aqueous dissolution of O_2 are negligible. Gas advection is controlled by gas permeability; advection becomes important when high air turbulence (i.e., strong wind) creates pressure difference in coarse gravels (Kimball and Lemon 1971), and when significant gas consumption in the subsurface occurs, e.g., due to active sulfide oxidation (Binning et al. 2007). Convection is relevant when a large amount of heat is generated, e.g., due to active sulfide oxidation (Amos et al. 2015). Non-Darcian flow becomes relevant when the flow velocity is high. For non-reactive soil covers containing low-permeability materials, it can be assumed that O_2 consumption and temperature differences are insufficient to cause notable gas advection or convection within the cover. Development of fractures or punctures may provide conduits for advective gas transport or non-Darcian flow through partially saturated porous media (Persoff 2006). When water saturation is high, gas flow through fractures is limited (Persoff 2006).

For an ideal cover, diffusion is the dominant gas transport process, constituting up to 99% of the total O_2 flux (Collin and Rasmuson 1988, Collin 1998, Aubertin et al. 2000, Kim and Benson 2004). Gas diffusion can occur in both air and water, but diffusion is more rapid in air-filled pores than in water-filled pores (Aubertin et al. 2000). Gas diffusion can be described by Fick's first law:

$$\mathrm{F} = -D_e \frac{\partial C}{\partial z} \qquad \text{eq. 2-1}$$

where F is O_2 flux [M L^{-2} T^{-1}], D_e is effective O_2 diffusion coefficient [L^2 T^{-1}], C is concentration of O_2 [M L^{-3}], and Z is depth [L]. To prevent O_2 ingress, the typical target of O_2 flux is ≤ 50 g m^{-2} yr^{-1} to prevent AMD production in fresh tailings (MEND 1999).

Effective gas diffusion coefficient is related to the physical properties of the porous medium, such as air-filled porosity and tortuosity (Millington 1959). Although D_e can be directly measured in field and laboratory experiments, several empirical calculations have been developed, which can simplify the determination of D_e (e.g. Millington and Quirk 1961, Collin and Rasmuson 1988, Mbonimpa et al. 2003, Aachib et al. 2004). Calculations of D_e and O_2 flux in eq. 2-1 suggest that fine-grained material with a high degree of saturation and sufficient thickness can act as effective barriers to O_2 diffusion. Thus, in a mine waste cover, fine-grained materials of high saturation and sufficient thickness can act as barriers to both water and O_2.

Due to the benefits of incorporating multiple soil layers of different permeability in a cover, composite covers are being utilized more frequently (Aubertin et al. 2016). Many composite covers are flat, but some are gently sloped to promote lateral drainage and further impede infiltration into the underlying mine waste (Aubertin et al. 2009).

One concern of composite covers is breakthroughs in capillary water retention. With high infiltration, water content increases near the interface between the fine-grained and coarse-grained material, which causes a decrease in suction and results in water entry into the coarse-grained material (Baker and Hillel 1990). Examples of high infiltration include spring snowmelt infiltration and large precipitation events.

Another geotechnical concern of composite covers is their likelihood of defects, which can cause deterioration in the long-term performance of covers. Clay is susceptible to desiccation-induced joints (Albrecht and Benson 2001) and cracking due to freeze-thaw cycles (Graham and Au 1985, Othman and Benson 1993). Insulating the clay from freezing and adding overburden materials can help prevent the development of cracks (Othman and Benson 1993). Punctures are common in liners such as HDPE liners and other geomembranes (Power et al. 2021). These failures in the fine-grained and low-permeability

layers can lead to the development of preferential flow paths that increase hydraulic conductivity values. These failures can also become conduits for the advective or non-Darcian transport of O_2 into the underlying mine waste.

Despite extensive research on the design and performance of composite covers (MEND 2004), most studies focused on fresh unoxidized tailings. Few studies examined their application to legacy tailings that have already undergone oxidation (Pabst et al. 2017, 2018). Field sampling and monitoring data are essential to examining the long-term effectiveness of covers. Nevertheless, most existing studies are laboratory-based.

2.2.2 Geosynthetic clay liner

Among the low-permeability materials used in a cover, geosynthetic clay liners (GCL), an innovative liner material, are increasingly utilized in mining applications. Comprised of a thin bentonite layer bonded to geotextiles or geomembranes (Bouazza 2002), GCL displays very low hydraulic conductivity values in the range of 10^{-12} to 10^{-10} m s^{-1} (Bouazza 2002), so they can serve as an effective infiltration or drainage barrier. If GCL remains saturated, gas diffusion can be effectively mitigated (Aubertin et al. 2000). In geotechnical application, GCL can be a more favourable choice than clay liners due to the lower cost and greater resistance to freeze-thaw induced cracking (Koerner and Daniel 1997). Like other liners, GCL is susceptible to accidental punctures (Bouazza 2002, Power et al. 2021). Additionally, internal erosion and cation exchange processes can increase the hydraulic conductivity of GCL (Bouazza 2002).

The field performance of GCL as cover liners is variable. Hosney and Rowe (2013) exhumed and tested three types of GCLs placed directly on tailings or over a sand and gravel layer one to two years after placement; they found all GCLs to perform well as a hydraulic barrier. In contrast, Benson et al. (2007) examined a cover consisting of GCL between silty sand layers for a coal ash landfill, where hydraulic conductivity of the GCL increased significantly with time to as high as 4.8×10^{-5} cm s^{-1} due to cation exchange processes and dehydration in the GCL. These two studies did not evaluate the effectiveness of GCL as a gas migration barrier.

Some GCL covers are ineffective in limiting O_2 transport, especially when susceptible to desiccation. Renken et al. (2005a, 2005b) compared the cover performance of GCL

between sand and gravel layers against other barrier materials; it was found that although GCL effectively reduced O_2 concentrations in the underlying tailings in the first year, its performance declined in the second year due to GCL drying out in the summer. Renken et al. (2005b) also found the GCL not as effective as bentonite as an infiltration barrier. Similarly, Adu-Wusu and Yanful (2006) compared the 3-year field performance of GCL under gravelly sand as a cover on waste rock; they found that GCL did not significantly reduce the O_2 gradient due to its limited thickness, although it remained more effective than bentonite and sandy silt as an infiltration barrier. Additionally, the GCL layer was likely dehydrated in the summer and froze in the winter, which significantly increased the percolation rate due to preferential flow paths (Adu-Wusu and Yanful 2006).

The existing field studies on GCL focused on its application as a single layer of low-permeability barrier material. The combination of clay and GCL as the barrier was not reported in the literature. In addition, except for Benson et al. (2007), existing studies only evaluated field test plots instead of full-scale field implementations.

2.2.3 Objective

The objective of this study was to characterize the hydrogeology and gas transport characteristics of a composite cover incorporating a GCL on a legacy tailings impoundment in northern Ontario, Canada, to evaluate the effectiveness of the composite cover. This objective was addressed through a combination of field monitoring, laboratory characterization, and numerical simulation studies of variably saturated flow through the cover and tailings.

2.3 Site description

The abandoned Kam Kotia mine (48°36'N, 81°37'W) is a former Cu and Zn mine 20 km northwest of Timmins, Ontario (Figure 2-1a). The site is characterized by a continental climate. According to the data collected between 1981 and 2010 at the Timmins Victor M Power Airport (Environment and Climate Change Canada 2021), 17 km east of the site, the mean annual air temperature is 1.8 °C. January is the coldest month with an average temperature of -16.8 °C and July is the warmest month with an average temperature of 17.5 °C. The mean annual precipitation is approximately 835 mm, with 558 mm as rain.

The mine was abandoned in 1972 without rehabilitation, leaving behind 6 million tonnes of tailings in three main areas of deposition, North Impounded Tailings (NIT), North Unimpounded Tailings (NUT), and South Unimpounded Tailings (SUT) (SENES Consultants Ltd. et al. 2000). At NIT, most areas of the tailings overlie an unconfined aquifer of glaciofluvial sand except the south end, which is a topographically high point and overlies bedrock outcrop. Over the decades, oxidation of the tailings resulted in AMD that migrated downward and contaminated the groundwater in the unconfined aquifer (SENES Consultants Ltd. et al. 2000). Because the NIT is topographically higher than its surroundings with hydraulic head buildup from its impoundment, AMD-impacted groundwater plume migrated to the south and southeast (SENES Consultants Ltd. et al. 2000). Discharge of AMD-impacted groundwater to nearby wetlands and streams also contaminated the surface water.

In 2008, the Ontario Ministry of Ministry of Northern Development, Mines, Natural Resources and Forestry (NDMNRF) constructed a composite cover on the NIT (Hamblin 2008). From the top to the bottom, the cover is composed of an upper sand layer (0.6 m), clay (0.3 m), GCL (0.008 m), lower sand (0.3 m), and waste rock (0.3 m) overlying the weathered tailings (Figure 2-2). GCL was included because laboratory characterization revealed that the clay developed cracks after a freeze-thaw cycle (Wardrop Engineering Inc. 2005). After cover construction, the ground surface at NIT is gently to moderately inclined towards the north with an average slope of 10%. The composite cover was subsequently vegetated primarily with grass.

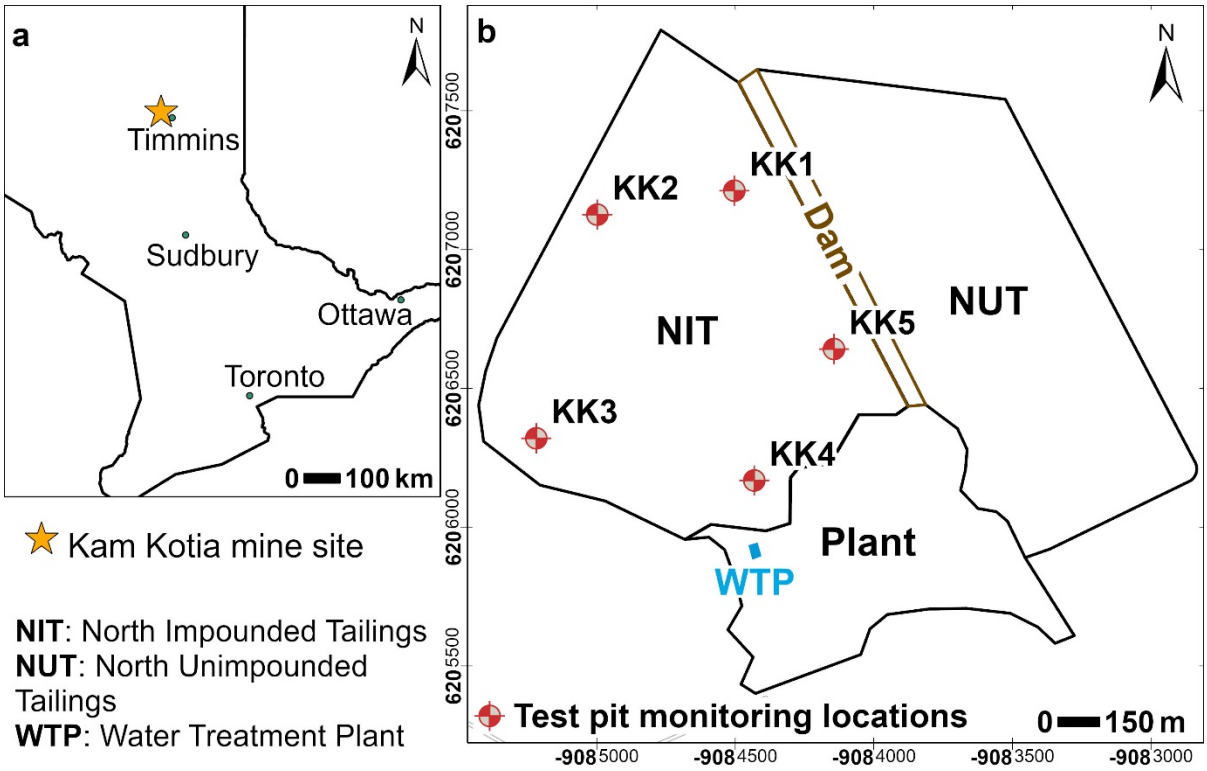

Figure 2-1. (a) Location of Kam Kotia mine within Ontario, Canada. (b) Aerial image of the mine site with UTM coordinates and the five test pits excavated in 2017 at NIT.

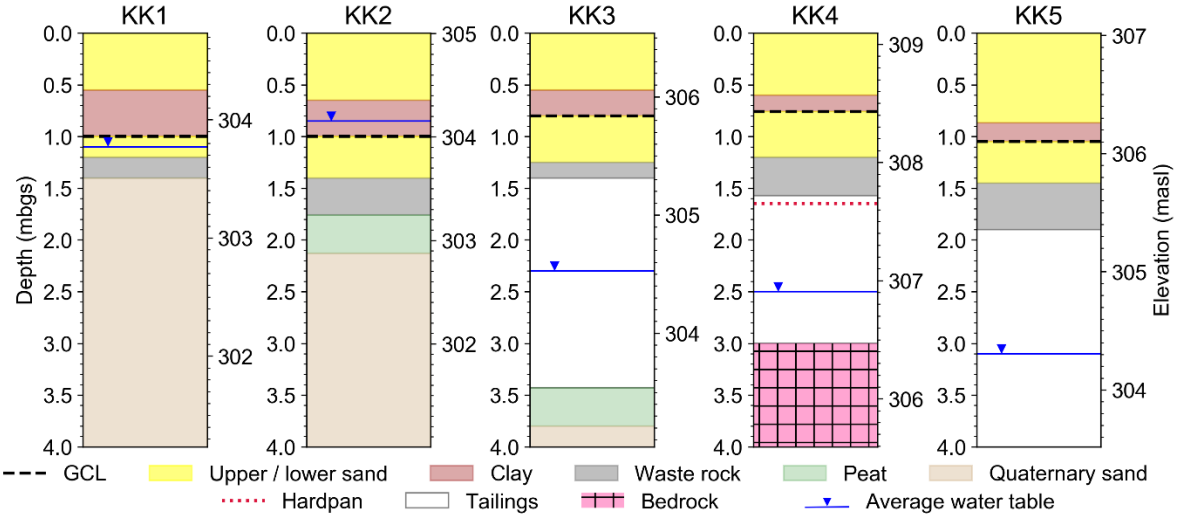

Figure 2-2. Cross-sectional lithology of five test pits at NIT with the five-layer composite cover in both depth (meters below ground surface, mbgs) and elevation (meters above sea level, masl)

2.4 Methods

2.4.1 Groundwater monitoring and field instrumentation

Instrument installation, site investigation, and sampling previously conducted by Schmall (2020) are summarized in §1.3 and Table 1-1. Additional water-level data from nested piezometers at the five test pit locations were collected during three subsequent monitoring events from 2021 to 2022. Water-table elevations at each test pit in meters above sea level (masl) were calculated using surveyed top of casing and ground elevations. These water-table elevations were interpolated using inverse distance weighting (IDW) and contoured in ArcGIS Pro (Esri) for lateral groundwater flow at NIT. Vertical hydraulic gradients at each location were calculated from nested piezometers.

To determine the potential presence of a perched water table and horizontal flow in the upper sand layer, one shallow piezometer above the clay layer was installed at each test pit in May 2022. Additionally, four piezometers were also installed around the perimeter of the NIT impoundment to delineate potential linkages between groundwater inside and outside the impoundment. Leveloggers® (Solinst) were also placed in three piezometers to continuously monitor water-level changes from May to September 2022.

Continuous records of *in situ* soil moisture and temperature were available from September 2018 to May 2019 for three test pit locations (KK1, KK4, and KK5). Data collection was interrupted in 2019-2021 due to COVID-19-related travel restrictions. Measurements resumed in 2021-2022. Over half of the soil moisture sensors became unresponsive between May 2019 and July 2021. Several tensiometers also became leaky. Replacement and additional instrumentation, including soil moisture probes (TEROS 12, METER Group, Ltd.) and tensiometers (Soilmoisture Equipment Corp.) were installed above the GCL at KK3, KK4, and KK5 in May 2022 in the clay and sand layers. Replacement and additional instruments were not installed below the GCL to prevent the perforation of the liner. TEROS 12 sensors were recorded by ZL6 data loggers (METER Group, Ltd.) and tensiometer transducers by Data Dolphin loggers, both at 4-hour intervals.

All *in situ* instrumentation data were processed as daily mean values to smooth out erratic changes and diurnal fluctuations in the recorded data. Data from soil moisture sensors were converted from dielectric permittivity to volumetric water content (θ_w) using the Topp et al.

(1980) equation. Matric suction (Ψ) in centibar measured by tensiometers was converted to meters. Because matric suction is equivalent to negative pressure head (ψ), total hydraulic head (h) was calculated using elevation data. Soil water retention curves for different layers of the cover were constructed from θ_w and Ψ to estimate corresponding hydraulic parameters for unsaturated soil: α and n, residual volumetric water content (θ_r), and saturated volumetric water content (θ_s), according to the van Genuchten (1980) equation:

$$\theta_w = \frac{\theta_s - \theta_r}{(1 + (\alpha|\Psi|)^n)^{1-\frac{1}{n}}} + \theta_r \qquad \text{eq. 2-2}$$

Meteorological data, including daily mean air temperature, daily precipitation, and depth of snow on the ground, were downloaded from two weather stations near Timmins Victor M Power Airport approximately 17 km east of Kam Kotia (Environment and Climate Change Canada 2022). The snowmelt period was estimated from air temperature and snow on ground data.

2.4.2 Physical property characterization

Hydraulic conductivity (K) tests were conducted at piezometer KK5-4 in May 2022 via rising-head tests. Water in the piezometer was pumped dry and the rising water-level responses were recorded manually using a water-level tape over 30-second intervals for 20-30 minutes. The data were analyzed using the Hvorslev (1951) method and K was calculated using the following equation:

$$K = -\frac{r^2 \ln\left(\frac{L}{r}\right)}{2L} \frac{1}{t} \ln\left(\frac{\Delta H}{\Delta H_0}\right) \qquad \text{eq. 2-3}$$

where r is the radius of the piezometer and the piezometer screen (0.375''), L is the length of the screen (6''), ΔH_0 is the initial displacement, and ΔH is the displacement at time t, the elapsed time.

Cores of cover layers and tailings collected in October 2017 (Starr and Ingleton 1992) were split into halves, sectioned, and sampled for physical and material properties. A total of nine samples for upper sand, two samples for clay, and 25 samples for tailings were collected. Wet bulk density (ρ_w) was determined by coring and weighing the samples with a small aluminum tube of a known inner diameter. Dry bulk density (ρ_b), gravimetric water

content (θ_g), and θ_w were determined after oven-drying the samples at 105 °C for 24 hours. Particle density (ρ_p) was obtained using an air compaction pycnometer. Porosity (ϕ) was calculated as:

$$\phi = 1 - \frac{\rho_b}{\rho_p} \quad \text{eq. 2-4}$$

Particle-size distribution was analyzed for 19 tailings samples by mechanical sieving method (ASTM 2017) using sieves #18 (1 mm), #35 (0.5 mm), #60 (0.25 mm), #120 (0.125 mm), #230 (0.063 mm), #325 (0.045 mm), and pan (<0.045 mm). Particle-size distribution curves were plotted to determine effective particle diameters d_{10} and d_{60}, as well as the uniformity coefficient (C_u) for each sample.

Saturated hydraulic conductivity values (K_{sat}) for tailings were determined in the laboratory by rigid-wall falling head permeameter tests (ASTM 2015). Tailings samples were retrieved from cores and oven-dried overnight at 80°C before being packed into sample cells for falling head tests. The samples were saturated with degassed water from the bottom up. The water level in the manometer tube that was connected to the top of the permeameter cell was monitored over time. Hydraulic conductivity was calculated as:

$$K = \frac{aL}{\mathrm{At}} \ln\left(\frac{H_0}{H_1}\right) \quad \text{eq. 2-5}$$

where *a* is the cross-sectional area of the manometer tube, *L* is the sample length, *A* is the cross-sectional area of the sample cell, *t* is the elapsed time, H_0 is the initial head in the manometer, and H_1 is the final head in the manometer. Results were reported as the mean of three tests. Detailed permeameter tests for cover sand and clay were previously conducted in a design report (Wardrop Engineering Inc. 2005) during the cover design phase. These results were considered reliable and permeameter tests were not conducted for the cover layers.

2.4.3 Stable water isotopes

Three additional field sampling events were conducted for pore water and groundwater at KK3, KK4, and KK5; samples for stable water isotopes were collected without filter or preservation. Stable water isotopes ($\delta^{18}O$ and $\delta^{2}H$) analysis was performed with a Picarro L2130-i Isotope and Gas Concentration Analyzer. Results were reported relative to Vienna

standard mean ocean water (‰ VSMOW). Results from three previous sampling events in 2018 were also incorporated into the data analysis.

Local Meteoric Water Line (LMWL) at Bonner Lake, the closest Global Network of Isotopes in Precipitation (GNIP) station approximately 95 km northwest of Kam Kotia, was obtained from the GNIP dataset (IAEA/WMO 2022) to represent stable water isotope composition of the rainwater at Kam Kotia. Local Evaporation Line (LEL) was obtained by the least squares regression of the isotopic composition of field-collected pore-water and groundwater samples.

2.4.4 Numerical modelling of variably saturated flow

The water balance of the composite cover system can be represented as:

$$P = ET + R + NP + \Delta S \qquad \text{eq. 2-6}$$

where P is precipitation (both rain and snowmelt), ET is evapotranspiration, R is runoff (surface runoff and throughflow), NP is net percolation into underlying tailings, and ΔS is the change in storage.

For cover with permeable material (sand) as the top layer, surface runoff is negligible. A simplified water balance at the surface of the cover is:

$$P = ET + I \qquad \text{eq. 2-7}$$

where I represents infiltration.

ET was calculated with the FAO-56 modified Penman-Monteith model (Allen et al. 1998):

$$ET_0 = \frac{0.408\Delta(R_n - G) + \gamma \frac{900}{T + 273} u_2 (e_s - e_a)}{\Delta + \gamma(1 + 0.34u_2)} \qquad \text{eq. 2-8}$$

where ET_0 is the reference potential evapotranspiration rate (mm d^{-1}), T is daily mean air temperature (°C), u_2 is the wind speed at 2 m above the ground (m s^{-1}), R_n is net radiation (MJ m^{-2} d^{-1}), G is soil heat flux density (MJ m^{-2} h^{-1}) assumed to be 0 for daily calculations, e_s is saturation vapour pressure (kPa), e_a is actual vapour pressure, Δ is the slope of the vapour pressure versus temperature curve (kPa $ºC^{-1}$), and γ is psychrometric constant.

Since some of the required parameters, such as R_n, were not directly measured at the weather stations, these parameters were estimated using available meteorological data according to the procedures outlined in FAO-56 (Allen et al. 1998). Parameters such as hourly temperature, wind speed, and relative humidity were downloaded from two weather stations near Timmins Victor M Power Airport (Environment and Climate Change Canada 2022), which were subsequently processed as daily means, maximums, and minimums to facilitate parameter calculation. A complete description of Penman-Monteith input parameters and calculations can be found in Appendix A. Because the cover is vegetated with grass, an albedo of 0.23 was assigned (Allen et al. 1998) and reference evapotranspiration was adopted as actual evapotranspiration, except in the winter. Because evapotranspiration is minimal under a snow cover (Allen et al. 1998), actual evapotranspiration was modified as zero during winter conditions.

One-dimensional numerical modelling of variably saturated flow through the composite cover and tailings was carried out using the Hydrus 1-D software (Šimůnek et al. 2013). This program uses the finite element method to solve Richard's equation for saturated-unsaturated water flow. For one-dimensional heat transfer without vapour transport, the program solves the convection-dispersion equation with the finite element method.

Simulations were conducted for the four locations KK1, KK3, KK4, and KK5, over the corresponding periods of *in situ* instrumentation. Simulated processes included water flow, heat transport, and snow hydrology. Pore-water freezing and associated changes in hydraulic conductivity was not accounted for in the Hydrus simulations. The domains were constructed as 1.4 m (for KK1), 3 m (for KK3 and KK4) and 3.5 m (for KK5) 1-D vertical columns with 1 cm discretization. The duration of the first simulation was 249 days (September 12th, 2018 to May 18th, 2019), consistent with the available *in situ* sensor data in 2018 and 2019, whereas the duration of the second simulation was 268 days (January 1st to September 25th, 2022) to account for snowmelt processes in 2022. Six distinct layers (upper sand, clay, GCL, lower sand, waste rock, and tailings) were defined according to the corresponding lithology (Figure 2-2).

For water flow, the top boundary was assigned as an atmospheric boundary with daily precipitation and calculated evapotranspiration fluxes (eq. 2-8). The bottom boundary was

assigned as a constant head boundary to match the average field-measured water-table depths at each location. Water-table elevations were set to depths of 1.6 m, 3.0 m, 3.0 m, and 3.2 m for KK1, KK3, KK4, and KK5, respectively, to correspond to field measurements. For heat transfer, the temperatures at the top and bottom boundary were derived from continuous temperature measurements from the shallowest and deepest *in situ* sensors. Heat transport parameters (solid volume fraction, longitudinal thermal dispersivity, and coefficients for the thermal conductivity function) were adopted from Chung and Horton (1987) and assigned to each layer.

To facilitate model calibration, the depths of transient θ_w output were assigned to correspond with the depths of *in situ* soil moisture sensors to allow direct comparison between simulated and measured θ_w. The same set of hydraulic parameters (van Genuchten α and n, θ_r, θ_s, K_{sat}, L) was used across all four test pit locations. Tortuosity (L) was assumed to be 0.5 for all layers. K_{sat} derived from permeameter tests (this study or Wardrop Engineering Inc. (2005)) were applied where available. For the upper sand, the clay, and the lower sand layers, van Genuchten α, n, θ_r, and θ_s derived from fitting the *in situ* soil water retention curve were applied. Hydraulic parameters for GCL were adopted from Benson et al. (2007). All other hydraulic parameters were initially estimated using the pedotransfer functions in Rosetta Lite v. 1.1 (Schaap et al. 2001) and adjusted during model calibration. Hysteresis in the retention curve and hydraulic conductivity was included in the simulation with the hydraulic parameters describing the initial drying curve. Calibration was conducted until a reasonable agreement between simulated and measures θ_w was achieved at all depths.

2.4.5 Pore-gas measurements and O_2 flux calculations

Between 2021 and 2022, three additional sampling events were conducted for pore gas. Pore-gas (O_2 and CO_2) concentrations from gas ports were measured by a field O_2/CO_2 analyzer (Quantek Instruments 902P). Alternatively, gas samples were collected with Exetainers™ and analyzed using gas chromatography (GC, SRI 8610A). To obtain gas concentrations from shallow depths in the upper sand layer, hollow-stem steel rods were inserted into the ground at fixed depths and attached under suction to a field O_2/CO_2 analyzer for pore-gas measurements.

Using the physical property characterization results, including ϕ and θ_w, effective O_2 diffusion coefficient (D_e) values were estimated with the equation (Aubertin et al. 2000, Mbonimpa et al. 2003, Aachib et al. 2004):

$$D_e = \frac{1}{\phi^2}(D_a^0 {\theta_a}^{3.3} + H D_W^0 {\theta_w}^{3.3}) \quad \text{eq. 2-9}$$

where the free O_2 diffusion coefficient in the air $D_\alpha^0 \approx 2.07 \times 10^{-5} \mathrm{m^2 s^{-1}}$ at 25°C and the free O_2 diffusion coefficient in the water $D_w^0 \approx 2.38 \times 10^{-9} \mathrm{m^2 s^{-1}}$at 25°C (Gliński and Stępniewski 1985), θ_a is air-filled porosity or volumetric air content ($\theta_a = \phi - \theta_w$), and H is Henry's Law coefficient ($H \approx 0.03$ at 20°C).

Values of D_e were also estimated using *in situ* continuously measured θ_w by assuming constant ϕ for a layer (adopted from physical property characterization and numerical modelling). This enabled calculation of continuous D_e time series and seasonal mean D_e corresponding to the availability of instrumentation records.

Equivalent D_e for the composite cover was estimated as the harmonic mean (Aubertin et al. 2000):

$$\overline{D}_e = \frac{\sum z_i}{\sum \frac{z_i}{D_{ei}}} \quad \text{eq. 2-10}$$

where z_i is the thickness of a uniform layer i, and D_{ei} is D_e of a uniform layer i.

Maximum O_2 flux at the interface between the cover and tailings occurs when O_2 is depleted at the base of the cover. Assuming that diffusion is the only O_2 transport process, which is valid for ideal covers without imperfections, this maximum flux can be calculated using the steady-state solution to Fick's first law:

$$F_{max} = \frac{\overline{D}_e (C_0 - C_1)}{z_c} \quad \text{eq. 2-11}$$

where z_c is the total thickness of the cover, C_0 is atmospheric O_2 concentration (0.278 kg m^{-3}), and C_1 is 0 kg m^{-3} at the base of the cover.

To evaluate cover efficiency, calculated O_2 flux is typically compared to estimated O_2 flux through uncovered tailings (Nicholson et al. 1989). Oxygen flux through uncovered tailings

was estimated using the following equation modified from Fick's second law of diffusion assuming a first-order rate of O_2 consumption with rate coefficient K_r, and that D_e and θ_w are independent of time and depth (z) in the tailings (Nicholson et al. 1989):

$$(\theta_a + H\theta_w)\frac{\partial C}{\partial t} = D_e\frac{\partial^2 C}{\partial z^2} - K_r C \qquad \text{eq. 2-12}$$

where K_r can be estimated from the following equation (Collin 1998):

$$K_r = K'\frac{6}{D_H}(1-\phi)C_p \qquad \text{eq. 2-13}$$

C_p is pyrite weight fraction (g g^{-1}) from quantitative mineralogical analysis such as X-ray diffraction (XRD), K' = 5 x 10^{-10} m^3 O_2 m^{-2} pyrite s^{-1} (Collin 1998), and D_H is the effective particle size estimated as (Aubertin et al. 1998):

$$D_H = (1 + 1.17\ logC_U)d_{10} \qquad \text{eq. 2-14}$$

A steady-state condition can be rapidly achieved, especially when K_r/D_e ratio is large (Nicholson et al. 1989). Assuming steady-state conditions, i.e., $\frac{\partial C}{\partial t} = 0$, eq. 2-12 can be written as:

$$\frac{\partial^2 C}{\partial z^2} = \frac{K_r}{D_e}C \qquad \text{eq. 2-15}$$

with the following boundary conditions

$$\begin{cases} C = C_0\ when\ z = 0\ (ground\ surface) \\ C = 0\ when\ z = z_0\ (depth\ at\ which\ O_2\ is\ depleted) \end{cases}$$

the solution to eq. 2-15 can be written as:

$$C = A\exp\left(\sqrt{\frac{K_r}{D_e}}z\right) + B\exp\left(-\sqrt{\frac{K_r}{D_e}}z\right) \qquad \text{eq. 2-16}$$

where

$$A = \frac{C_0\exp\left(-\sqrt{\frac{K_r}{D_e}}z_0\right)}{\exp\left(-\sqrt{\frac{K_r}{D_e}}z_0\right) - \exp\left(\sqrt{\frac{K_r}{D_e}}z_0\right)}$$

$$B = \frac{-C_0 \exp\left(\sqrt{\frac{K_r}{D_e}} z_0\right)}{\exp\left(-\sqrt{\frac{K_r}{D_e}} z_0\right) - \exp\left(\sqrt{\frac{K_r}{D_e}} z_0\right)}$$

Accordingly, using Fick's first law, the flux at the surface of tailings (z=0) is:

$$F_0 = D_e \left(B \sqrt{\frac{K_r}{D_e}} - A \sqrt{\frac{K_r}{D_e}} \right) \qquad \text{eq. 2-17}$$

2.5 Results and discussion

2.5.1 Hydrogeological characteristics and processes

2.5.1.1 Groundwater flow

Multi-year groundwater monitoring data reveal a consistent seasonal pattern in groundwater flow in the NIT flow system. May 2022 groundwater elevation data represent a typical spring groundwater flow system, including perched groundwater, at NIT (Figure 2-3, Figure 2-4), whereas November 2021 is representative of a late summer and fall groundwater flow system and is shown in Figure 2-5. Groundwater flow maps during other sampling events are in Appendix B.

In the spring, saturated groundwater flow under the cover in the tailings and in the sand aquifer beneath the tailings displayed a strong horizontal hydraulic gradient (>0.003, or 3 m head difference over 1 km of horizontal distance) from high hydraulic heads at the south to low heads at the north and northeast (Figure 2-4). Vertical gradients (average 0.23) were upward at each nested piezometer, indicating the potential for downward groundwater flow. In addition, a perched water table that followed the slope of the clay (Figure 2-3) was observed at all five test pits from May to June 2022. A gradual increase in water level at the KK4-2.85 piezometer was observed from May to June 2022 (Figure 2-6).

These observed groundwater flow patterns suggest that in the spring, snowmelt infiltration was impeded by the clay and created saturated conditions in the upper sand. The strong horizontal gradient in the perched groundwater flow system promoted lateral drainage of water that followed the slope of the clay layer. Meanwhile, slow vertical infiltration into the clay and underlying units occurred, and the infiltrated water eventually recharged the actual water table under the cover, which was demonstrated by the gradual increase of water level in the tailings at KK4. Location KK4 is situated at the high point of ground elevation of NIT and overlies bedrock outcrops with no connection to the quaternary sand aquifer. Gradual infiltration from the cover was the only source of groundwater replenishment at KK4.

In late summer and fall, saturated groundwater flow was generally not observed in KK4 tailings. Instead, groundwater flow at NIT was towards the east with a horizontal hydraulic gradient of approximately 0.0006 (Figure 2-5). The water level at the KK4-2.85 piezometer gradually decreased from July to September 2022 (Figure 2-6). The perched water table above the clay was not present in the summer. In the fall, a perched water table may occur briefly due to frequent precipitation events; however, it was not captured by the groundwater monitoring events. Seasonal water-table fluctuations were up to 1.7 m for KK3 and KK5, 0.8 m for KK1, 0.7 m for KK4, and 0.5 m for KK2.

These observed flow patterns suggest that after the cessation of spring snowmelt infiltration, the perched water table at NIT dissipated due to both lateral drainage and downward infiltration. Under the cover, groundwater dispersed away from the south end of NIT (KK4) without substantial replenishment, causing the water table to decrease until the tailings above the bedrock outcrop became unsaturated throughout. The absence of high hydraulic head levels from the south caused a shift in the flow system. High hydraulic heads to the west (KK2 and KK3) compared to the east (KK1 and KK5) resulted in an eastward groundwater flow. Although large precipitation events likely caused perched water-table conditions to occur temporarily above the clay, vertical infiltration into the clay and underlying unit was not significant; there was no measurable increase in the water level at the KK4-2.85 piezometer.

Continuous water-level data at KK3 displayed large temporal fluctuations in water level corresponding to snowmelt, precipitation, and drought, whereas the water level at KK2 was

stable in May and decreased steadily since June (Figure 2-6). Large water-level fluctuations at the southern half of NIT (KK3 and KK5) with higher ground elevation were caused by the accumulation and release of hydraulic heads at the south end of NIT with bedrock outcrops. Water-level monitoring outside the impoundment indicates that KK3 groundwater was hydraulically connected to the wetlands and sand aquifer outside the impoundment, which further contributed to large fluctuations in water level at KK3 in response to meteorological events. During late summer, fall, and winter, eastward groundwater flow from outside the impoundment to NIT likely displaced the tailings-derived plume water outward.

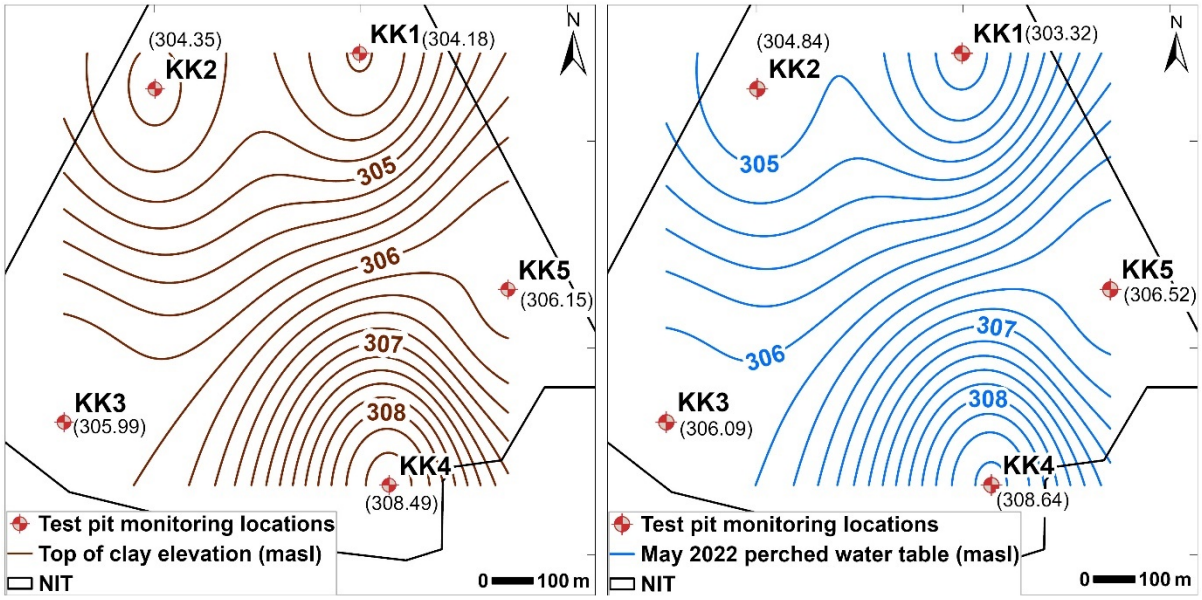

Figure 2-3. Top of clay elevation contours at NIT compared to representative spring (May 2022) perched water-table elevation contours above the clay layer. A contour interval of 0.2 m was used in both maps.

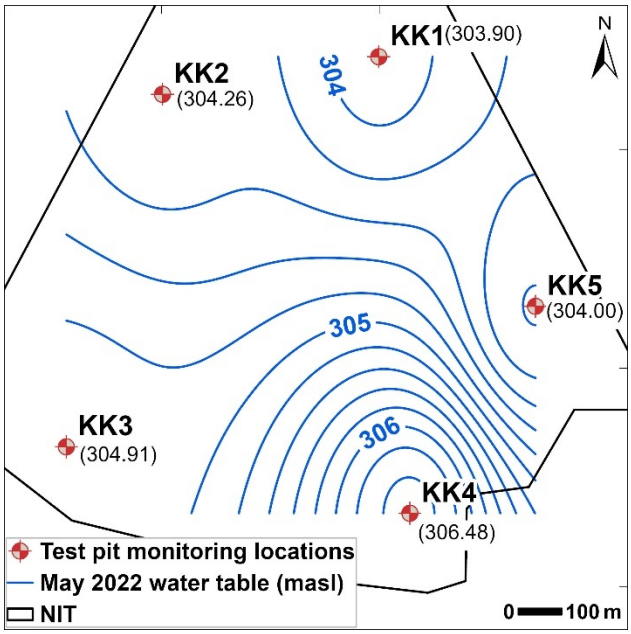

Figure 2-4. Representative spring and early summer (May 2022) water-table elevation contours in the tailings and sand aquifer at NIT. A contour interval of 0.2 m was used.

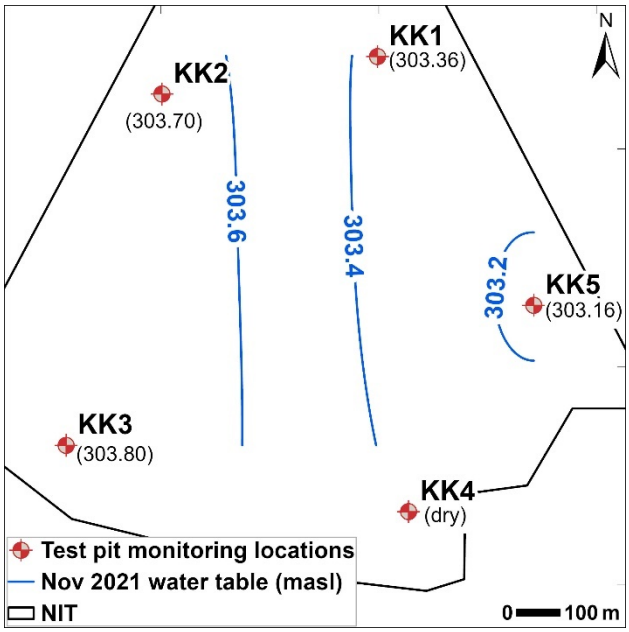

Figure 2-5. Representative late summer, fall, and winter (November 2021) water-table elevation contours in the tailings and sand aquifer at NIT. A contour interval of 0.2 m was used.

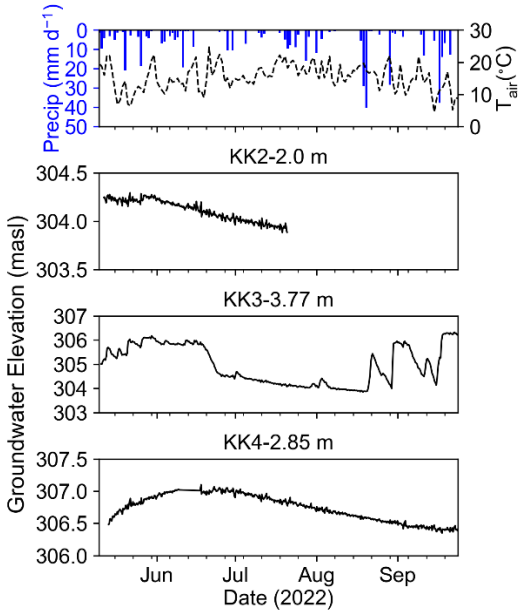

Figure 2-6. *In situ* continuously measured water-level data at three piezometers from May 10th to September 25th, 2022. The instrumentation at KK2-2.0 m malfunctioned so only partial data were available.

2.5.1.2 Physical properties

The mean and standard deviation values of ρ_p, ρ_b, ϕ (accounted for core compression), S, and d_{10} from particle-size analysis for upper sand, clay, and tailings are summarized in Table 2-1. The mean particle size for tailings is fine sand (Figure 2-7). Heterogeneity in material properties is present among samples collected from the same cover layer (Table 2-1). All saturation values at and above the clay and GCL layer are below one, which confirms that the perched water table was not present in the cover system during coring in October 2017.

Results from *in situ* K test conducted at KK5-4 piezometer and falling head permeameter tests are summarized in Table 2-2. Results from field tests and laboratory analysis are comparable and in the range of K values typically reported for silt and silty sand (Freeze and Cherry 1979).

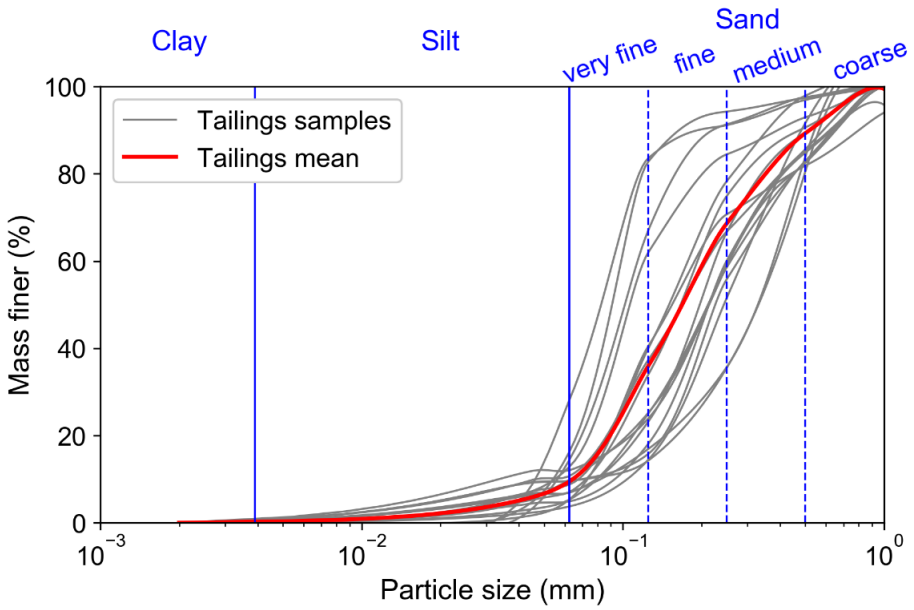

Figure 2-7. Particle-size distribution curve for tailings from 19 samples.

Table 2-1. Summary of material properties for two cover layers and tailings, including particle density (ρ_p), dry bulk density (ρ_b), porosity (ϕ), saturation (S), and effective particle diameters d_{10}. Insufficient samples were available from the other layers for physical characterization.

Material	ρ_p (g m^{-3})	ρ_b (g m^{-3})	ϕ (-)	S (-)	d_{10} (mm)
Upper sand	2.67 ± 0.09	1.50 ± 0.69	0.44 ± 0.20	0.28-0.83	0.170 ± 0.03
Clay	2.76 ± 0.30	1.32 ± 0.72	0.52 ± 0.28	0.70-0.76	-
Oxidized tailings	2.51 ± 0.13	0.95± 0.03	0.62 ± 0.02	0.47-0.84	0.083 ± 0.015
Unoxidized tailings	3.02 ± 0.26	1.50 ± 0.26	0.50 ± 0.07	0.52-0.99	0.065 ± 0.013

Table 2-2. *In situ* rising-head hydraulic conductivity (K) test results analyzed with the Hvorslev (1951) method (the mean result of two tests) and results from laboratory falling head permeameter tests (average of three tests).

Location	Depth (m)	Material	Method	K (m s^{-1})
KK5	4.0	unoxidized tailings	rising-head K tests	6 x 10^{-7}
KK3	1.45-1.65	oxidized tailings	permeameter	4 x 10^{-7}
KK3	2.0-2.4	unoxidized tailings	permeameter	4 x 10^{-7}

KK4	2.2-2.4	unoxidized tailings	permeameter	6×10^{-7}
KK5	2.2-2.5	unoxidized tailings	permeameter	1×10^{-6}

2.5.1.3 Source of water - stable water isotopes

Stable water isotopes are useful trackers of the source of water and processes in the hydrological cycle. Plots of the water isotopic composition of different layers (Figure 2-8) show no noticeable deviation from the LEL, which indicates that the pore water and groundwater in NIT covers and tailings originated from local precipitation. The LEL nearly overlaps with the LMWL, indicating minimal evaporative enrichment of water isotopes between the meteoric water and water in the subsurface.

For upper sand, water isotopes in the summer and fall (July 2018, September 2018, August 2021, and November 2021) cluster around the right end of the LEL, indicating that they are more enriched in the heavier isotopes (^{18}O and ^{2}H). In contrast, spring water samples (May 2018 and June 2022) cluster at the left end of the LEL, indicating depletion in the heavier isotopes. Compared to snow, rainwater is more enriched in the heavier isotopes due to Rayleigh distillation (Dansgaard 1964). Because pore water in the summer and fall in the shallowest layer originated from rainwater whereas pore water in the spring was largely derived from snowmelt, the isotopic characteristics of pore waters align with those of their precipitation source. This alignment suggests that the residence time for water in the upper sand layer is relatively short.

In contrast, water isotopes from the clay, lower sand, waste rock, and tailings are not as enriched in the heavier isotopes. Instead, they tend to cluster in the middle and lower left regions of the graph regardless of the sampling time. Some water isotopes from the tailings are located at the far-left end of the plot, depicting the strong influence of the more isotopically depleted winter precipitation. These trends indicate that winter precipitation was a significant source of pore water and groundwater in the lower layers of the cover and tailings throughout the year. In addition, snowmelt had a longer residence time in the tailings than rainwater.

Water isotope results suggest that during the summer and fall, water in the upper sand layer was quickly replenished with rainwater. Infiltration into the underlying layers was

limited by the clay, and the water in the upper sand dispersed, possibly through lateral drainage and evapotranspiration. Capillary pressure increase from occasional rainfall events was insufficient to exceed the water-entry values of the underlying sand, so deep rainwater infiltration was rare. In contrast, excessive spring snowmelt penetrated deep into the cover and tailings and constituted a large portion of the local groundwater recharge.

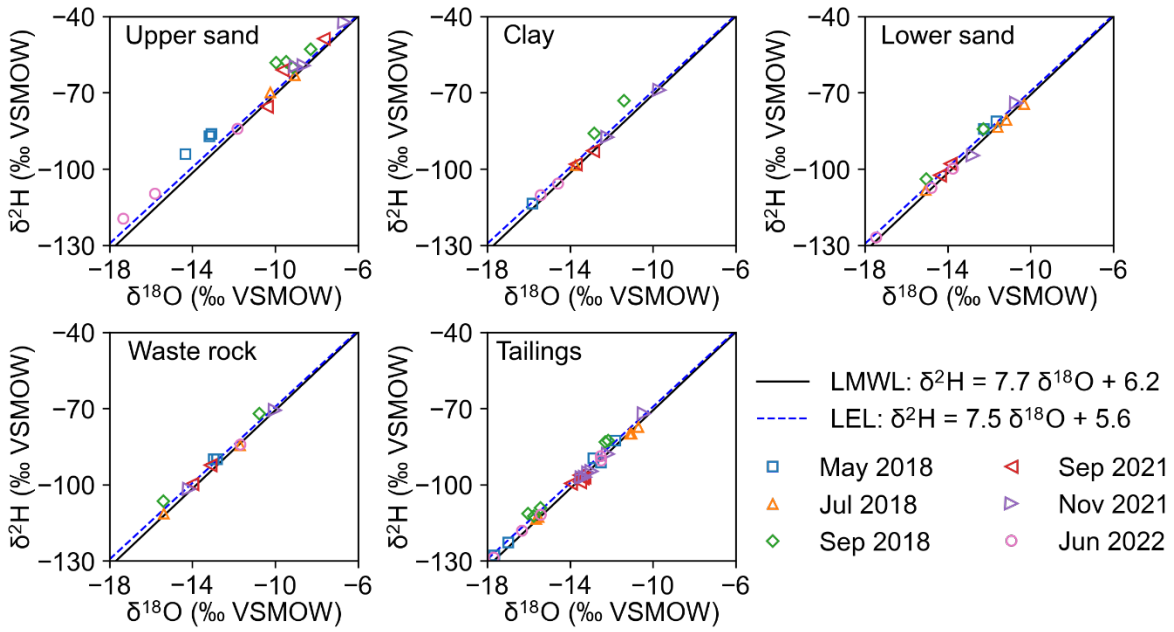

Figure 2-8. Plots of water isotope composition ($\delta^{18}O$ and $\delta^{2}H$) of pore-water and groundwater samples for each cover layer and tailings. Different symbols indicate six sampling events. The solid line indicates the LMWL at Bonner Lake and the dashed line represents the LEL calculated from all collected water samples.

2.5.1.4 Cover hydrology - *in situ* instrumentation

A comparison between precipitation records and daily mean θ_w shows that before winter conditions started in November 2018, θ_w in the shallowest upper sand layer changed abruptly in response to precipitation and evapotranspiration (Figure 2-9). Frequent precipitation during the fall caused near-saturated conditions in the upper sand in September and October 2018, as well as September 2022 (Figure 2-9, Figure 2-10). Pore-water freezing would cause a decline in dielectric permittivity recorded by the soil moisture

sensors. Between November 2018 and March 2019, θ_w at shallowest depths declined markedly, likely due to the progressive freezing of pore water in the shallow subsurface, even though measured temperatures remained slightly above 0 °C. Pore-water freezing may cause erratic changes in the dielectric permittivity measured by the sensors. Around mid-March, an increase in θ_w at the shallow depths occurred at all locations, which coincided with the onset of snowmelt. A combination of pore-water thawing and snowmelt infiltration likely occurred. Another abrupt increase in θ_w occurred at the end of the snowmelt period following a large influx of snowmelt. In spring 2022, similar abrupt changes in θ_w at shallower depth occurred at KK3 and KK4 in response to snowmelt infiltration and precipitation. The deeper portion of the upper sand remained saturated due to the presence of the perched water table. In summer 2022, θ_w in the upper sand declined rapidly to as low as the residual saturation in response to dry conditions in July and early August.

Stable θ_w values were maintained in the clay throughout the fall, winter, and spring (Figure 2-9). Except for a slight decline in θ_w in February 2019, likely due to pore-water freezing, and a slight increase in θ_w in mid-March due to pore-water thawing and/or snowmelt infiltration, little changes in θ_w occurred. Temperatures in the clay layer were slightly higher than those in the upper sand layer in the winter months, suggesting that the top sand provided a certain degree of insulation against freezing. Desiccation of the clay occurred twice in the summer of 2022 at KK3 and KK4, which corresponded to dry conditions and low θ_w values close to the residual saturation in the upper sand (Figure 2-10). In both cases of desiccation, θ_w values recovered to or near the saturated values following precipitation events. At KK5, there was no evidence of clay desiccation.

The θ_w measurements in lower sand, waste rock, and tailings displayed moderate temporal changes, which were much less pronounced than those in the upper sand. Stable θ_w values in the waste rock at KK1 were due to the shallow water table (average 1.6 meters below ground surface or mbgs) and the soil moisture sensor located near the tension-saturated zone. Since temperatures did not drop below 0°C for the deeper sensors, freezing of the pore water did not occur. Slight increases in θ_w occurred in the KK5 waste rock and tailings, and the KK4 tailings at the end of the snowmelt period immediately following the θ_w increase at the shallowest depth (Figure 2-9). These observations indicate that water was released from the base of clay and GCL as a pressure response to the infiltration from the

surface, i.e., peristaltic displacement. A gradual decline in θ_w in the tailings occurred at KK3 and KK4 in summer 2022, which was attributed primarily to changes in the water-table positions.

Tensiometer records show increases in Ψ (or a decline in h) in response to evaporation under dry conditions and declines in Ψ (or an increase in h) in response to precipitation in the upper sand and clay (Figure 2-11, Appendix C). During the dry periods, Ψ increased rapidly in the upper sand until a rapid recovery occurred following precipitation events. At KK3, Ψ in the clay shows similar variability as the deeper portion of the upper sand; in contrast, at KK4, Ψ in the clay was stable except for a small increase (i.e., decrease in h) towards the end of a dry period in mid-August. The Ψ and h values in lower sand and waste rock remained stable and minimally impacted by precipitation and evaporation at the surface. Apart from the dry periods, downward hydraulic gradients persisted in the vadose zone, indicating downward movement of water. During the dry periods, upward evapotranspiration flux may temporarily cause upward transport within the shallowest few cm.

Soil water retention curves describe the hydraulic behaviour of unsaturated materials through the relationship between θ_w and Ψ. Overall good agreement was obtained between the field data and fitted curves (Figure 2-12). For the upper sand and the lower sand, the two fitted parameters α and n both fall within the range of values for sand; similarly, the fitted parameters for the clay were within the range of values in the literature (Schaap et al. 2001). For the upper sand, data from different depths show variability, indicating heterogeneity and potential hysteresis. Hysteresis is further indicated by the scattering of data points at low Ψ. Tensiometers in the clay did not record a wide range of values. For the lower sand, recorded θ_w values at low matric suction are lower than those predicted by the van Genuchten (1980) equation; this observation indicates that the response in the lower sand layer may also be hysteretic. However, hysteresis was not adequately captured by soil water retention curves at this layer.

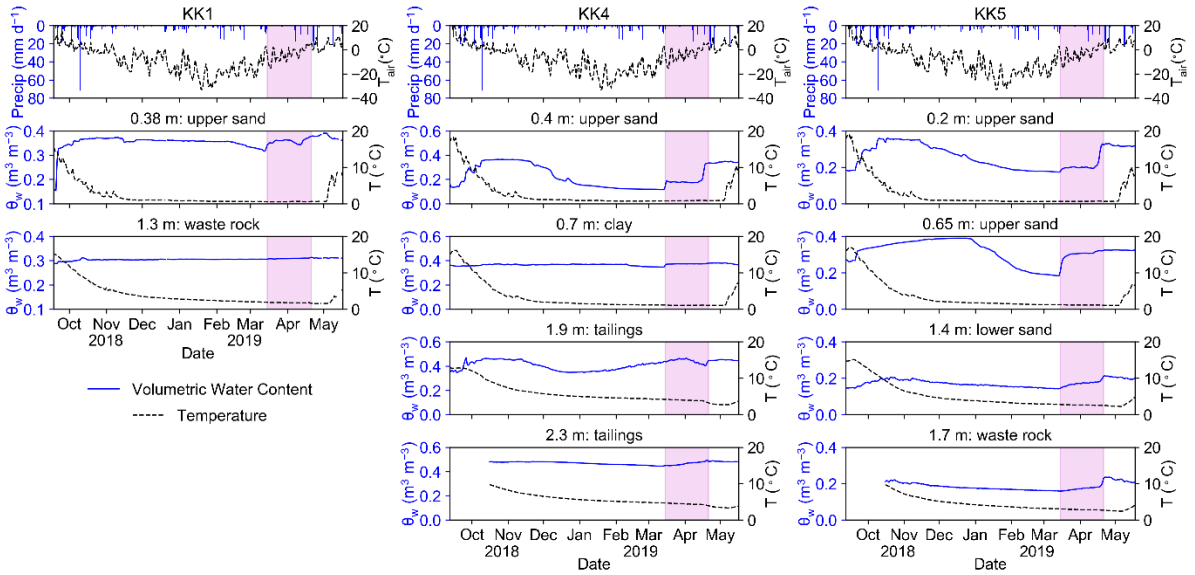

Figure 2-9. First row: temporal variations of precipitation (blue bars) and air temperature (black dashed lines) recorded at a nearby weather station from September 12th, 2018 to May 18th, 2019; second to fifth rows: daily mean time series of volumetric water content (θ_w, blue solid lines), and temperature (black dashed lines) recorded by soil moisture sensors at three test pit locations. The vertical pink area indicates the snowmelt period.

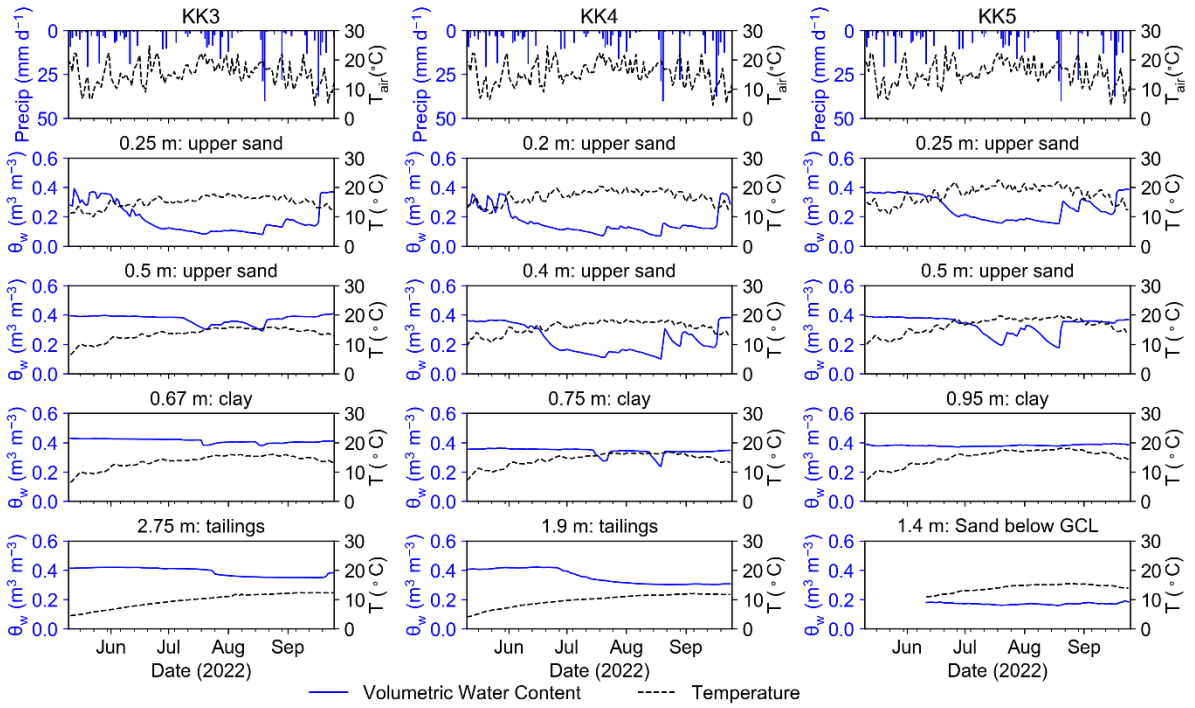

Figure 2-10. First row: temporal variations of precipitation and air temperature recorded at a nearby weather station from May 10th to September 25th; second to fifth rows: daily mean time series of volumetric water content (θ_w, blue solid lines), and temperature (black dashed lines) recorded by soil moisture sensors at three test pit locations.

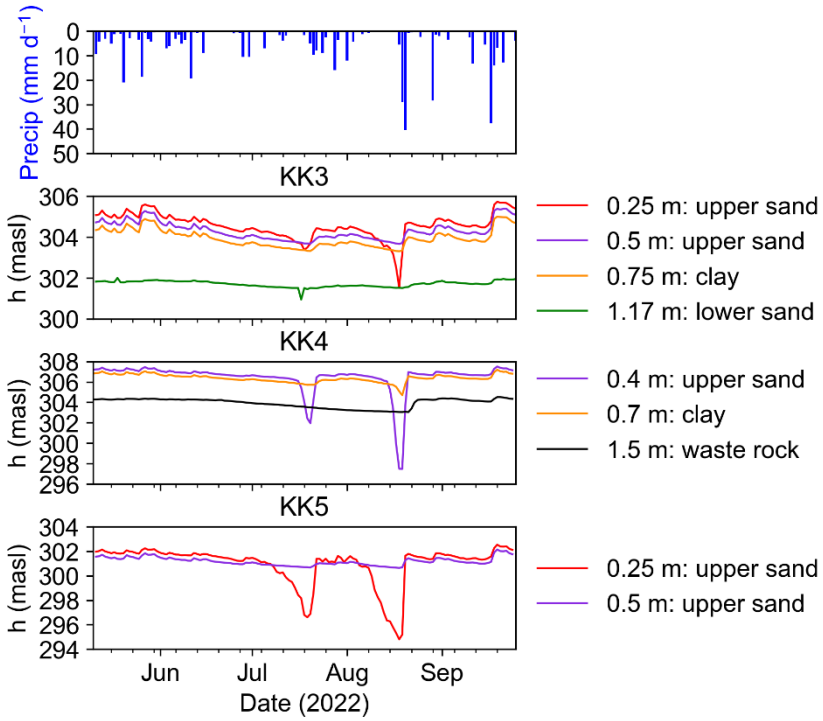

Figure 2-11. Time series of daily mean hydraulic head (h) in meters above sea level (masl) calculated from matric suction recorded by tensiometers at three test pit locations in 2022.

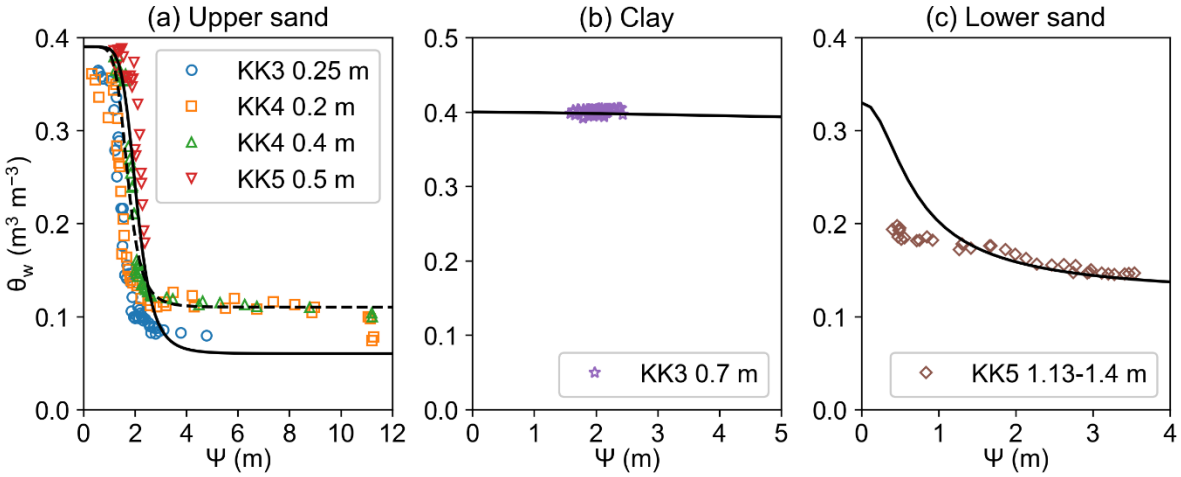

Figure 2-12. Soil water retention curves (black solid lines) fitted to *in situ* instrumentation data using eq. 2-2 for (a) the upper sand: $\alpha = 0.5\ m^{-1}$, n=7, $\theta_r = 0.03$, and $\theta_s = 0.39$. (b) the clay: $\alpha = 0.04\ m^{-1}$, n=1.3, $\theta_r = 0.15$, and $\theta_s = 0.4$ (c) the lower sand: $\alpha = 2\ m^{-1}$, n=2.2, $\theta_r = 0.12$, and $\theta_s = 0.33$. Note: for (a), the dashed line represents an alternative best fit to the data ($\alpha = 0.6\ m^{-1}$, n=7, $\theta_r = 0.11$, and $\theta_s = 0.39$); however, these parameters resulted in non-convergence in subsequent Hydrus 1-D simulations so were not adopted.

2.5.2 Numerical modelling of variably saturated flow

Calculated evapotranspiration values with modification that limits evapotranspiration under a snow cover indicate that evapotranspiration accounts for approximately 70% of precipitation year-round, although large seasonal variations exist.

Figure 2-13 compares the measured and Hydrus 1-D simulated θ_w with the hydraulic parameters listed in Table 2-3. Overall good agreement between measured and modelled θ_w across KK4 and KK5 suggests that the calibrated hydraulic parameters were representative of the cover layers and tailings at NIT. Hydraulic parameters derived from fitting *in situ* instrumentation data for the upper sand, clay, and lower sand (Figure 2-12) were used in the simulation. The inclusion of hysteresis (see §2.4.4) improved the θ_w fit, especially for the shallowest upper sand layer; this trend indicates that hysteretic behaviour in drying and wetting likely occurred.

Simulated θ_w in the shallowest upper sand deviated from measured θ_w during the winter (Figure 2-13). Freezing of the pore water might have occurred in the shallow layers during the winter, despite *in situ* temperatures remaining slightly above 0°C, suggesting that the

effect of pore-water freezing on θ_w was not well captured by the simulation. The θ_w dynamics during the spring snowmelt period were captured relatively well by the simulation. During the summer, simulated θ_w values in the upper sand were lower than measured values, especially at lower depths. Water-table fluctuations were not incorporated into the model due to a lack of continuous groundwater level data during the simulation period. The gradual decrease of θ_w in the tailings was probably induced by the declining water table and therefore was also not captured by the simulation. Furthermore, ignoring spatial heterogeneity and prescribing the same set of hydraulic properties across all locations in the simulations likely contributed to the discrepancies between the simulated and measured θ_w. As revealed by physical property characterization, heterogeneity in porosity, particle-size distribution, and corresponding hydraulic properties existed in all materials. In addition, discrepancies may result from instrumentation limitations and issues. For example, loss of sensor contact with soil may occur during dry periods and result in lower-than-expected θ_w values.

Simulated boundary fluxes (Figure 2-15) show that the discharge at the bottom of the 1-D profiles was negligible throughout most of the year. In 2019, a high discharge occurred following snowmelt infiltration in late April 2019, when water was displaced through the clay and GCL into the lower layers, which characterizes a breakthrough in the capillary barrier effect. Similarly, a high discharge at the lower boundary occurred throughout May and June 2022. A time lag was observed between upper boundary recharge and lower boundary discharge, indicating that the low-permeability layers suppressed the response to infiltration. Lower boundary discharge following precipitation events in October 2018 was limited and had a noticeable time lag from recharge. No noticeable discharge occurred after the cessation of snowmelt infiltration in summer 2022, despite multiple rainfall events. Minimal discharge throughout the summer, fall and winter indicates that the composite cover may effectively impede infiltration from extreme rainfall events.

Several limitations exist for the model simulations. The 1-D assumption of the system would be problematic if significant horizontal throughflow above the clay occurred. Throughflow is difficult to estimate and as previously discussed (2.5.1.1 and 2.5.1.3), displacement of water from the upper sand layer into the clay occurred despite throughflow. Substantial throughflow likely only occurred in the spring and briefly in the fall if excessive

precipitation occurred, the 1-D assumption was suitable for the rest of the year. In addition, seasonal water-table fluctuations were neglected, but an overall good agreement between simulation results and field measurements indicates that the assumption of a constant water table is reasonable.

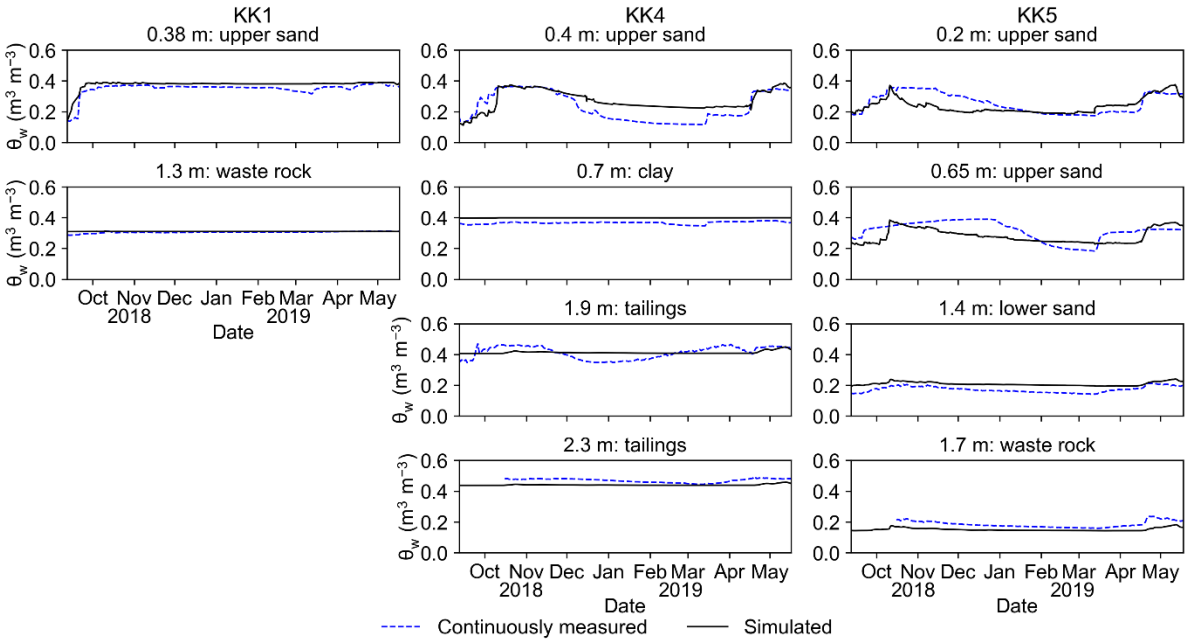

Figure 2-13. Hydrus 1-D simulated volumetric water content (θ_w) compared to *in situ* continuously measured θ_w from September 12th, 2018 to May 18th, 2019.

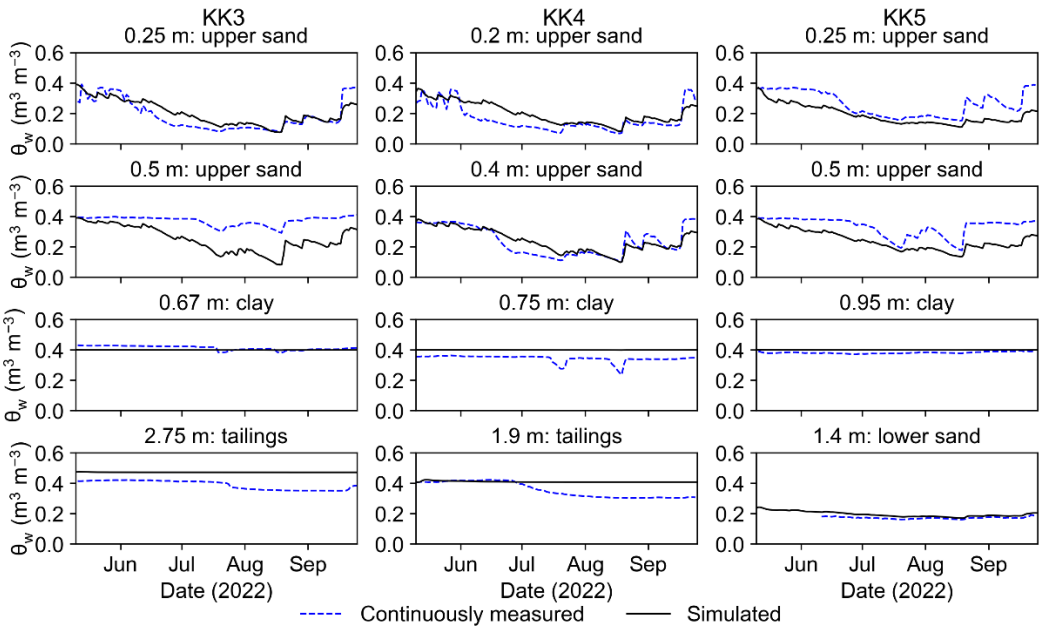

Figure 2-14. Hydrus 1-D simulated volumetric water content (θ_w) compared to *in situ* continuously measured θ_w from May 10th to September 25th, 2022.

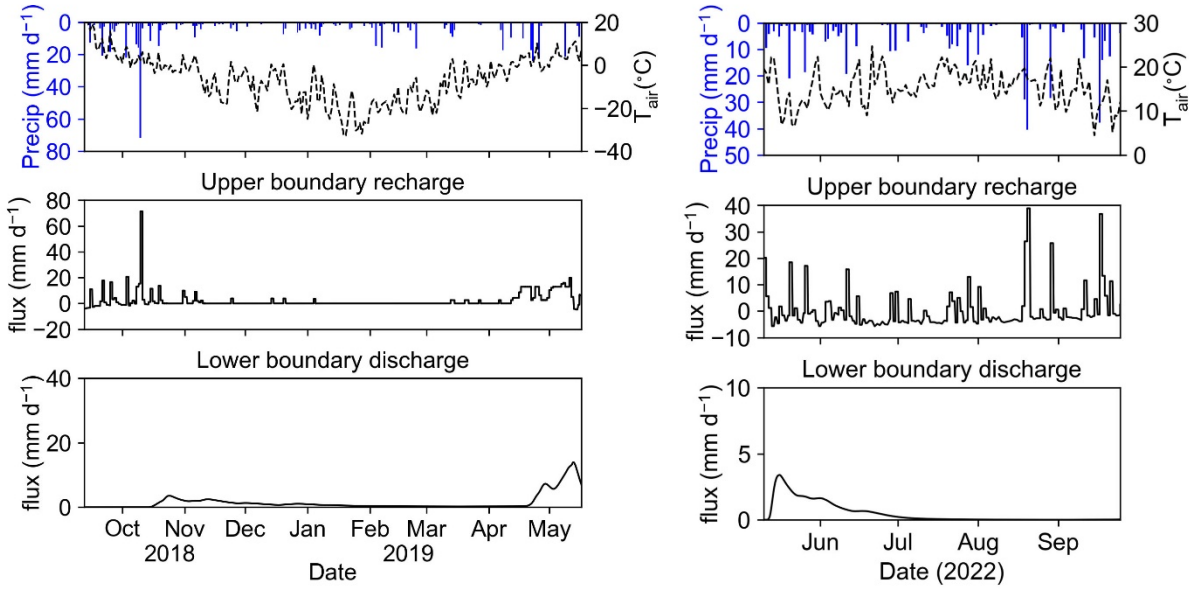

Figure 2-15. Hydrus 1-D simulated fluxes at KK4 from September 12th, 2018 to May 18th. 2019, and from May 10th to September 25th, 2022.

Table 2-3. Hydraulic parameters used in Hydrus 1-D simulations. Tortuosity (L) of 0.5 was used for all layers.

Material	θ_r (m^3 m^{-3})	θ_s (m^3 m^{-3})	α (m^{-1})	n (-)	K_{sat} (m s^{-1})
Upper sand	0.06	0.39	0.50	7.0	1.00×10^{-4}*
Clay	0.15	0.40	0.04	1.3	1.88×10^{-7}*
GCL*	0.068	0.60	0.001	2.0	5.80×10^{-11}
Lower sand	0.12	0.33	2.0	2.2	1.00×10^{-4}*
Waste rock	0.13	0.39	3.0	3.6	5.00×10^{-5}
Tailings	0.05	0.48	0.7	1.6	1.00×10^{-6}

*K_{sat} values for the clay and sand were adopted from Wardrop Engineering Inc. (2005).

**Hydraulic parameters for GCL were adopted from Benson et al. (2007).

θ_r: residual volumetric water content

θ_s: saturated volumetric water content (=ϕ)

α, n: van Genuchten (1980) parameters for water retention curves

K_{sat}: saturated hydraulic conductivity

2.5.3 Oxygen transport

Oxygen transport provides the driving force for sulfide oxidation. Characterizing gas transport in the subsurface informs cover performance in preventing O_2 ingress. At KK3, a general trend of decreasing O_2 concentrations and increasing CO_2 concentrations across the GCL was observed during all sampling events; pore-gas O_2 concentrations were as low as 5 vol.% before reaching the waste rock (Figure 2-16). These measurements suggest that the composite cover impeded atmospheric O_2 ingress. Calculated D_e values in the fall and winter were up to three orders of magnitude higher than those in the spring. Spring snowmelt infiltration resulted in a return to saturated conditions at the base of the upper sand and the lowest D_e values occurred immediately above the clay.

At KK4, a pronounced decrease in O_2 concentrations across the clay and GCL was only observed in May 2022, during which O_2 was nearly depleted and CO_2 concentrations were almost 10 vol.% (Figure 2-16). During the summer and early fall, O_2 concentrations were only moderately below atmospheric (10-15 vol.%) in the tailings. The highest pore-gas O_2 concentrations in the tailings, which were nearly atmospheric (20.9 vol.%), were observed in

November 2021; these measurements indicate seasonal variations in the effectiveness of the cover at KK4 that allow ingress of atmospheric O_2. The D_e of the clay was at water-saturated values in the spring but was two orders of magnitude greater in the fall and winter. The D_e values in other layers were also much lower in the spring than in the fall/winter. The thin hardpan around 1.65 mbgs in the tailings was not an effective barrier for O_2 transport, since D_e at that depth was high due to high porosity and low saturation.

At KK5, O_2 concentrations in the lower sand layer were moderately below atmospheric (8-15 vol.%) before reaching the waste rock during all sampling events (Figure 2-16). CO_2 concentrations were up to 5 vol.%. Like KK3 and KK4, D_e values at and above the clay layer were at water saturation in the spring. However, in the lower sand, D_e values were similar in the spring and the fall/winter.

Figure 2-17 and Figure S-C1 in Appendix C show the D_e time series calculated from Hydrus 1-D simulated θ_w and measurements by *in situ* moisture probes. Effective O_2 diffusion coefficient remained relatively stable in lower sand, waste rock, and tailings compared to those in the shallowest upper sand layer, which varied up to four orders of magnitude concomitantly. Desiccation in the clay during the summer caused an increase in D_e (Appendix C), which enabled increased O_2 diffusion. Differences in the simulated and measured D_e were analogous to those discussed in 2.5.1.4.

In cold regions where the ground is covered in ice and snow during the winter, gas diffusion through mine-waste covers only occurs for approximately 200 days of the year (Mbonimpa et al. 2003). Meteorological records from weather stations (Environment and Climate Change Canada 2022) suggest that despite interannual variations, the ground is likely snow and ice covered between November 15 and May 1 annually. Thus, annual O_2 flux was assumed to occur for a period of 198 days (May 1 to November 15). Using the moisture-content values derived from the Hydrus 1-D simulations, equivalent D_e across the cover (eq. 2-10) during the following time periods was taken as the annual mean D_e: 2018-05-01 to 2018-05-18, 2018-09-12 to 2018-11-15, and 2022-05-19 to 2022-09-11. Subsequently, a maximum O_2 flux across the cover was calculated using eq. 2-11. Hypothetical O_2 fluxes in uncovered tailings were calculated assuming a value for K_r (eq. 2-13) estimated using XRD data and physical properties summarized in Table 2-1. It was

further assumed that O_2 becomes depleted at a depth (z_0) of 0.5 m at KK4 and at a depth of 0.2 m at KK5, based on pore-gas O_2 concentration measurements and the results of mineralogical studies, to facilitate the estimate of O_2 flux in uncovered tailings using eq. 2-17.

The calculation results in Table 2-4 demonstrate a vast difference in the annual O_2 flux between the covered and uncovered tailings for both KK4 and KK5. Oxygen fluxes in uncovered tailings are almost four orders of magnitude greater than those under a composite cover. Despite slight differences in the thickness of each layer, O_2 fluxes under the composite cover at the two locations are similar. These simplified calculations demonstrate that the composite cover may decrease the rate of sulfide oxidation by orders of magnitude. However, many simplifications were made in these calculations. The cover was assumed to be ideal without flaws or imperfections. Diffusion was assumed to be the only gas transport process in uncovered tailings. Advection could account for up to 23% of gas transport if gas consumption by sulfide oxidation occurred in the absence of carbonate dissolution and CO_2 generation, resulting in significant gas-pressure gradients (Binning et al. 2007); similar conditions are unlikely at Kam Kotia. Due to the limited duration of *in situ* measurements, D_e from different times that sum to one year was used to represent the mean annual D_e.

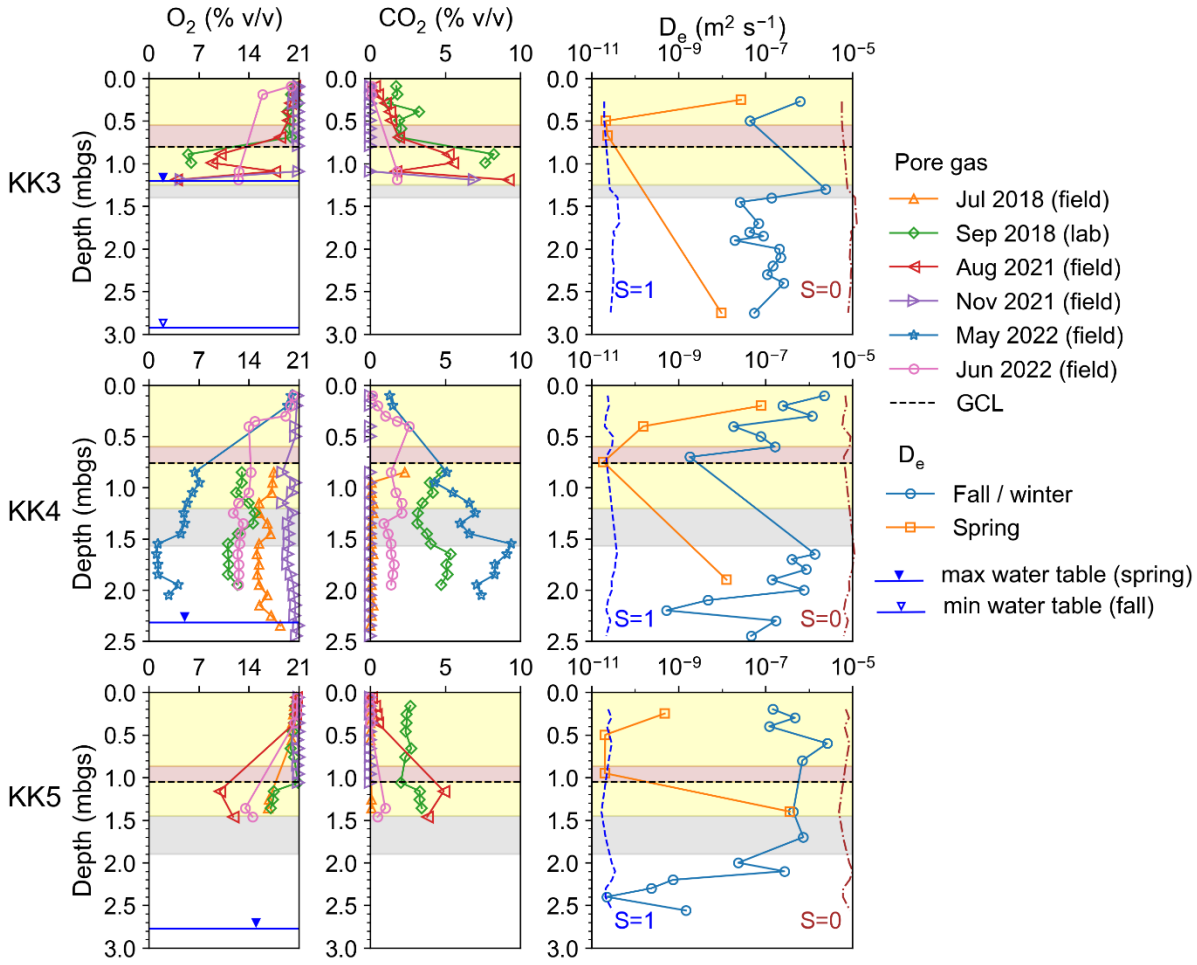

Figure 2-16. O_2 and CO_2 concentration profiles at KK3, KK4, and KK5 measured *in situ* or analyzed in the laboratory; profile of D_e from physical properties and *in situ* soil moisture sensors (eq. 2-9). Water-saturated and air-saturated D_e values were shown as blue dashed lines and brown dot-dashed lines, respectively.

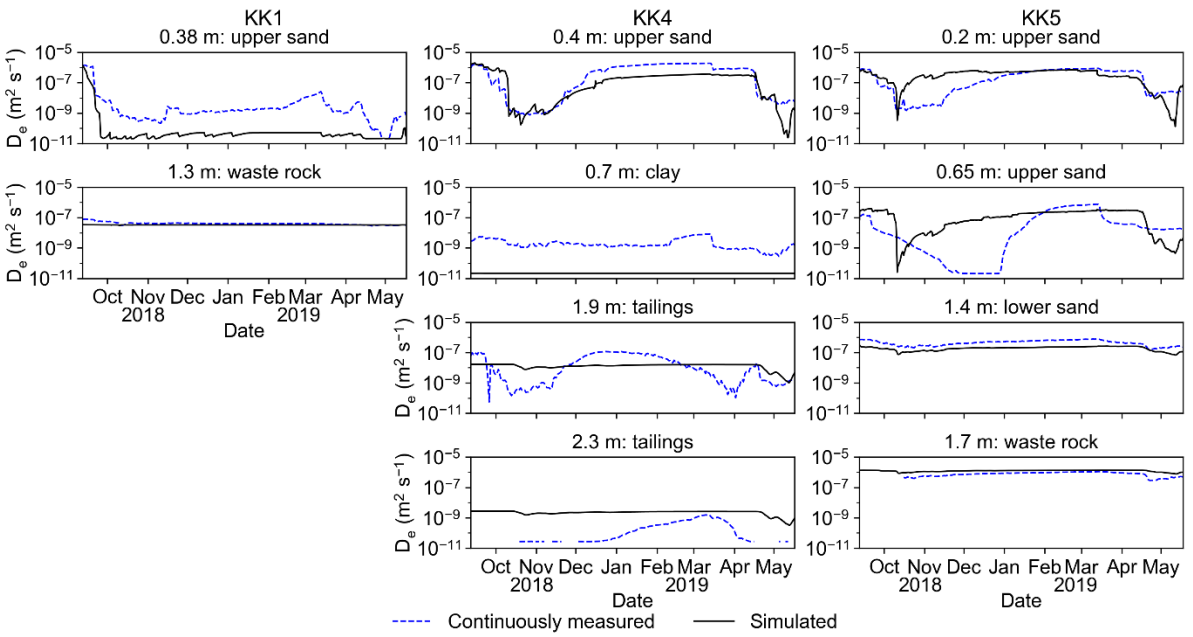

Figure 2-17. Time series of effective O_2 diffusion coefficient (D_e) between September 12th, 2018 and May 18th. 2019, calculated from *in situ* continuously measured soil moisture content (θ_w) and Hydrus 1-D simulated θ_w.

Table 2-4. Calculated annual O_2 flux with and without the composite cover at two test pit locations assuming O_2 flux occurs from May 1 to November 15 annually.

Location	With composite cover			Uncovered tailings			
	$\dot{D}_e$ (m^2 s^{-1})	z_c (m)	O_2 flux (g m^2 yr^{-1})	$\dot{D}_e$ (m^2 s^{-1})	K_r (s^{-1})	z_0 (m)	O_2 flux (g m^2 yr^{-1})
KK4	1.7×10^{-10}	1.57	0.5	3.3×10^{-8}	4.6×10^{-6}	0.5	2000
KK5	1.7×10^{-10}	1.90	0.5	4.3×10^{-8}	1.5×10^{-5}	0.2	4000

2.5.4 Cover effectiveness – infiltration and gas transport

The capillary barrier effect of the cover functioned well throughout most of the year (summer, fall, and winter), which is indicated by the low water saturation in lower sand and waste rock, more depleted water isotopes below the upper sand, and the low simulated discharge. Nevertheless, breakthroughs in the capillary barrier effect occurred following the

spring snowmelt, which resulted in downward displacement of water through the cover as indicated by higher moisture contents (Figure 2-9), water levels (Figure 2-6), and simulated discharge (Figure 2-15). The upper sand layer provided some protection for the clay and GCL by partially insulating the clay from freeze-thaw and evapotranspiration-induced desiccation. The clay layer performed relatively well as a moisture-retaining layer. Apart from two dry periods in summer 2022, the clay remained nearly saturated throughout multiple seasons. Although the GCL was not exhumed and examined, it was assumed to be at or near saturation because it underlies the clay.

The high degree of saturation in the clay and GCL throughout the year combined with the sufficient thickness of the clay effectively inhibited Fickian diffusion of O_2 at all monitoring locations. Oxygen flux calculations suggest that the cover significantly lowered the diffusive flux of O_2 into the underlying tailings.

Rapid O_2 diffusion was not observed at KK3 or KK5. The near-atmospheric O_2 concentrations under the clay and GCL at KK4 in November 2021 (Figure 2-16) indicate the decline in the moisture content of the sand layers and partial desiccation of the clay layer enabled diffusion of atmospheric O_2 gas through the cover and increased the potential for advective O_2 transport and possibly non-Darcian flow. Conduits may have been created by freeze-thaw induced fractures in the clay and/or defects in the GCL, such as accidental punctures formed during cover placement or instrumentation installation, and material deterioration caused by internal erosion and cation exchange. However, these imperfections were not captured by *in situ* instruments and are likely local features of limited extent. The depleted O_2 content in May 2022 at KK4 suggests that high degrees of water saturation in the spring inhibited O_2 transport through imperfections in the cover. Low D_e values in the spring also indicate low gas diffusion. Combined with the lack of gas transport under a snow cover, O_2-rich conditions in the KK4 tailings likely only occurred during the late summer and early fall.

2.6 Conclusions

Multi-year hydrogeological characterization, pore-gas monitoring, gas flux calculation, and 1-D variably saturated flow modelling revealed a strong seasonal pattern in water flow and gas transport at the composite cover and tailings at NIT. The clay layer in the composite

cover remained near saturation throughout most of the year, except for temporary desiccation during dry periods in the summer. The cover was effective in preventing infiltration during most of the year (summer, fall, and winter) when the capillary barrier effect functioned well. Fickian diffusion of O_2 was effectively limited by the combination of clay and GCL. However, local cover imperfections due to fractures in the clay and/or punctures in the GCL may have created conduits for O_2 transport into the tailings. In the spring, snowmelt infiltration created a perched water table above the clay, which promoted lateral drainage, breakthroughs in the capillary barrier effect, and downward displacement of the pore water through the clay. Snowmelt also altered the groundwater flow pattern due to higher hydraulic head values in the NIT and in adjoining streams and wetlands. Infiltration of snowmelt increased water saturation in the cover, which inhibited O_2 transport via both diffusion at intact cover locations and advection and/or non-Darcian flow at cover imperfections. This seasonal pattern suggests that despite potential local imperfections, the composite cover substantially reduced water infiltration and gas transport a decade after implementation.

This study filled the research gap in the long-term field performance of composite covers for mine waste remediation, especially a lack of knowledge on the effectiveness of covers on pre-oxidized legacy tailings. The results of this study can provide insight into cover design, mine closure, and remediation planning.

Chapter 3
Tailings geochemistry and mineralogy under a composite cover at Kam Kotia mine, ON

3.1 Summary

Remediation by a composite cover was implemented on legacy tailings in northern Ontario, Canada to reduce the production of acid mine drainage (AMD). The effect of the cover on rates of sulfide oxidation and trace element mobility was investigated a decade after cover placement. Multi-year measurements of pore-gas concentrations, pore-water and groundwater sampling and analysis, mineralogical studies of the tailings, selective chemical extractions, and synchrotron-based X-ray absorption experiments were conducted. Prior to cover placement, decades of subaerial oxidation of the sulfide-rich tailings (up to 74 wt% pyrite) depleted sulfide minerals to a depth of 0.1-0.25 m. Depleted pore-gas O2 concentrations, circumneutral pH, improvement in water quality, and sulfate reduction occurring in peat layers underlying the tailings were observed at one detailed sampling location, suggesting that the cover decreased AMD generation and transport. In contrast, near-atmospheric pore-gas O_2 concentrations, low pH, and elevated aqueous concentrations of Fe, SO_4, Zn, Cu, As, and Pb were present at another location, suggesting continued sulfide oxidation. Crystalline and amorphous Fe(III) (oxy)hydroxides, secondary covellite, and Fe(III) hydroxysulfate phases sequestered trace elements. Limited sequestration of Zn and Mn in secondary minerals and mobilization of As was observed, leading to the persistence of these elements in the pore water. Arsenate was more abundant than As(III) in secondary phases, but elevated concentrations of As(III) persisted even in the oxidized zone. Due to ongoing sulfide oxidation, element remobilization, and the limited capacity for sulfate reduction, diminished water quality, with elevated aqueous concentrations of SO_4, Zn, As, and Mn may persist.

3.2 Introduction

The mining industry generates large amounts of waste, mainly in the form of waste rock and mill tailings. Sulfide minerals commonly found in mine waste include pyrite [FeS_2], pyrrhotite [$Fe_{1-x}S$], chalcopyrite [CuFeS], sphalerite [ZnS], arsenopyrite [FeAsS], and galena

[PbS]. These sulfides are susceptible to oxidation in the presence of O_2 and water to produce acid mine drainage (AMD), which is a principal environmental concern facing the mining industry. Pyrite is one of the most common sulfide minerals. Although the mechanism of pyrite oxidation is complex and involves multiple intermediate steps and oxidation products, it can be generally represented as (Blowes et al. 2014):

$$FeS_2 + \frac{15}{4}O_2 + \frac{7}{2}H_2O \rightarrow Fe(OH)_3 + 2H_2SO_4 \qquad \text{eq. 3-1}$$

In addition to SO_4 and Fe, AMD can mobilize elements such as Cu, Zn, As, Ni, Co, and Pb via the oxidation of different sulfide minerals that are present in the mine waste. Other trace elements such as Cd and Hg, which occur as trace components in sulfide minerals, can also be leached into the environment.

AMD can be especially pronounced at historical or legacy mine sites which were left unrehabilitated for decades. This is partly because under acidic conditions in oxidized tailings, ferric iron becomes more soluble and can more readily oxidize sulfides through reactions mediated by acidophilic bacteria (Blowes et al. 2014). Costs associated with AMD remediation at abandoned and orphaned mines in North America are estimated to be tens of billions of dollars (INAP 2012).

Acidity produced by AMD can lead to the dissolution of gangue and secondary minerals in the mine waste and the surrounding soil and aquifer materials. These minerals, including calcite, dolomite, ankerite, siderite, Al hydroxides, Fe oxyhydroxides, and Al silicates, provide acid neutralization and pH buffering capacity (Blowes et al. 2014). However, the dissolution of these minerals has the potential to release greenhouse gases and introduces additional elements into the mine drainage, such as Al, Mn, Ca, Na, and Mg.

Another common process associated with AMD is secondary-mineral precipitation. The most common secondary phases include gypsum [$CaSO_4 \cdot 2H_2O$], Fe(III) oxyhydroxides including ferrihydrite [$Fe_{10}O_{14}(OH)_2$], goethite [α-FeO(OH)], lepidocrocite [γ-FeO(OH)], jarosite [$KFe_3(SO_4)_2(OH)_6$], natrojarosite [$NaFe_3(SO_4)_2(OH)_6$], secondary Al hydroxide [$Al(OH)_3$], primary or secondary siderite [$FeCO_3$], marcasite [FeS_2], and covellite [CuS] (Blowes et al. 2014). Some secondary phases, such as Fe(III) (oxy)hydroxides and Al

hydroxides, have large surface areas that facilitate the sorption of trace elements. Trace elements in AMD can also be sequestered through co-precipitation with secondary minerals.

Several mitigating and remedial techniques can reduce the availability of O_2 and water to curtail AMD generation. Among them, multi-layer composite covers attract growing attention as they are considered more effective than mono-layer covers (Aubertin et al. 2016). In a multi-layer cover system, a layer of low-permeability and highly saturated material with sufficient thickness acts as a barrier to the ingress of both O_2 and water. Clay, silt, and geomembranes are the most common low-permeability materials (MEND 2004, Aubertin et al. 2016). The low-permeability material is placed between coarse-grained material such as sand and gravel to achieve a capillary barrier effect, which further enhances the moisture retention of the low-permeability material (see Chapter 2).

In addition to geotechnical concerns of cover defects (detailed in Chapter 2), a geochemical concern of cover placement on legacy tailings is the remobilization of trace metal(loid)s previously sequestered by secondary minerals, which could be achieved through several mechanisms. Firstly, a change in water balance and water-table position caused by the cover may alter the precipitation and dissolution of water-soluble mineral phases and influence the mobility of weakly adsorbed elements (Holmström et al. 2001). Secondly, a change in the pore-water and groundwater pH can affect the sorption and desorption of trace metal(loid)s. Under higher pH conditions, resulting from lessened AMD production, oxyanion-forming elements such as As and Se tend to desorb (Smedley and Kinniburgh 2002), increasing their mobility in the aqueous phase. Thirdly, the gradual transformation of amorphous Fe(III) (oxy)hydroxide into more crystalline forms such as goethite and hematite can release trace metal(loid)s because higher crystallinity corresponds to less sorption capacity (Moncur et al. 2009). Last but not least, under reducing redox conditions, reductive dissolution of Fe(III) (oxy)hydroxides may occur and release trace elements. Biotic and abiotic reduction of Fe(III) (oxy)hydroxides was demonstrated in field studies (***e.g.***, Lovley et al. (1989), McCreadie et al. (2000)). Reductive dissolution of Fe(III) oxides through oxidation of organic carbon by microbes can be represented as:

$$2Fe_2O_3 + CH_2O + 7H^+ \rightarrow 4Fe^{2+} + HCO_3^- + 4H_2O \qquad \text{eq. 3-2}$$

Previous studies (Ribet et al. 1995, Gunsinger et al. 2006) proposed reductive dissolution of Fe(III) (oxy)hydroxide as an important mechanism for trace metal(loid)s release if oxidized tailings were to be remediated with a cover; however, field studies have not verified mobilization of sequestered elements in remediated tailings. It is uncertain whether sufficiently anaerobic or reducing conditions could be achieved with a composite cover in the absence of additional organic carbon.

Anaerobic conditions and availability of organic carbon can promote biotic sulfate mediated by dissimilatory sulfate reducing bacteria (DSRB):

$$SO_4{}^{2-} + 2CH_2O \rightarrow H_2S + 2HCO_3{}^{-} \quad \text{eq. 3-3}$$

Both eq. 3-2 and eq. 3-3 produce alkalinity that enhances acid neutralization. Subsequent precipitation of metal sulfides can attenuate aqueous concentration of metal(loid)s, such as Fe, Zn, Cu, and As:

$$Fe^{2+} + H_2S \rightarrow FeS + 2H^{+} \quad \text{eq. 3-4}$$

The objective of this study was to characterize the geochemistry and mineralogy of a legacy tailings impoundment in northern Ontario, Canada that was remediated with a composite cover, with a particular focus on sulfide oxidation processes beneath the cover and trace element sequestration and mobility.

3.3 Site description

The study site is the abandoned Kam Kotia mine (48°36'N, 81°37'W) near Timmins in northern Ontario, Canada (Figure 3-1a). The site is characterized by a continental climate with a mean annual temperature of 1.8 °C and annual precipitation of 835 mm (Environment and Climate Change Canada 2021). The bedrock is Archean metavolcanic rocks of the Tisdale Group, mainly komatiites and basalts (Pyke 1982). The principal sulfides in the ore body were pyrite, sphalerite, and chalcopyrite, while plagioclase, chlorite, quartz, micas, and siderite were the main gangue minerals (Winterhalder 1992, SENES Consultants Ltd. et al. 2000). Sulfides were massive as well as present as quartz-sulphide stockworks (Calder Engineering Ltd. 2013). Prior to mining activities, the surficial geology was glaciofluvial and

glaciolacustrine sand, silt, clay, and an overlying peat layer up to 0.6 m in thickness, with small areas of bedrock outcrops (SENES Consultants Ltd. et al. 2000).

The mine started operation in 1942 with open pit mining. It changed ownership three times and underground mining occurred in the 1960s and 1970s. The Kam Kotia mine mainly produced copper and zinc, as well as secondary gold and silver. The North Impounded Tailings (NIT) area located in the northwest of the site was one of the principal tailings deposition areas (Figure 3-1b). It was constructed in 1967 and tailings deposition occurred between 1968 and 1972 (Geologic Testing Consultants 1984). Production at Kam Kotia ceased in 1972 and the mine was subsequently abandoned with the responsibility of rehabilitation returned to the government. Sulfide oxidation continued over decades in the exposed and unrehabilitated tailings at NIT and other tailings deposition areas, resulting in the production of AMD with drainage pH<3 (SENES Consultants Ltd. et al. 2000). Most of the NIT tailings overlie peat or an unconfined quaternary sand aquifer, whereas at the south end the tailings overlie bedrock outcrops. Acid mine drainage in the NIT tailings migrated downward and resulted in the development of a plume in the quaternary sand aquifer (SENES Consultants Ltd. et al. 2000).

In 2001, the Ontario Ministry of Ministry of Northern Development, Mines, Natural Resources and Forestry (NDMNRF) initiated the rehabilitation of Kam Kotia. In 2008, a five-layer composite cover was constructed on NIT to reduce AMD generation (Hamblin 2008). From the top to the bottom, the cover consists of upper sand, clay, geosynthetic clay liner (GCL), lower sand, and waste rock (Figure 3-2).

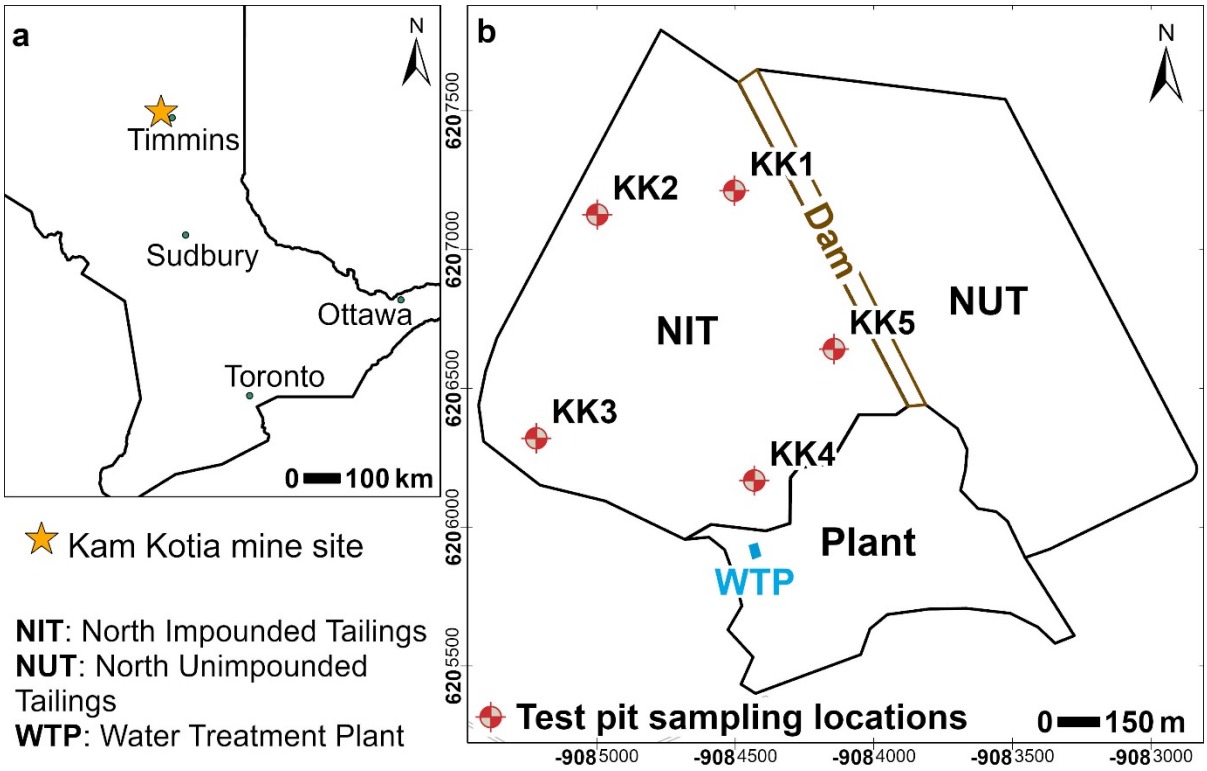

Figure 3-1. (a) Location of Kam Kotia mine within Ontario, Canada. (b) Conceptual diagram of the mine site including NIT and five test pits excavated in 2017 at NIT.

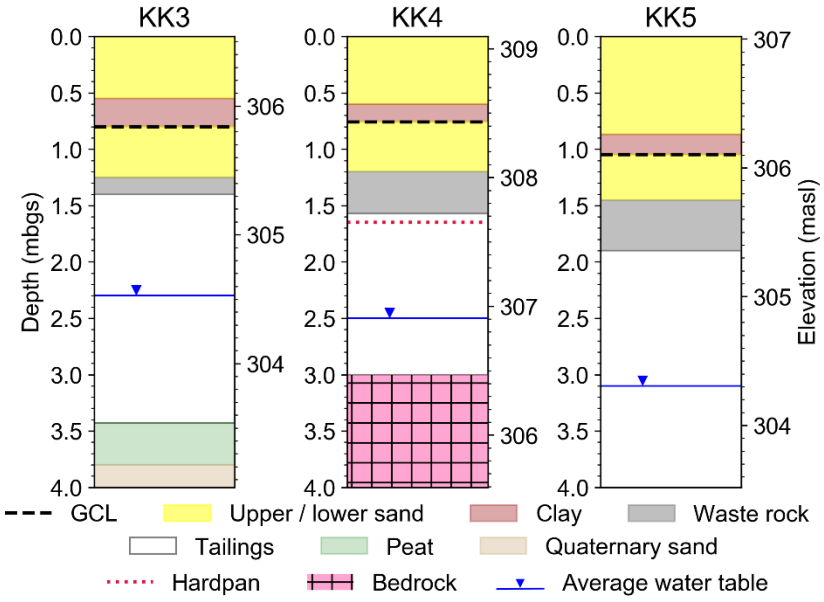

Figure 3-2. Cross-sectional lithology of three test pits at NIT with the five-layer composite cover in both depth (meters below ground surface or mbgs) and elevation (meters above seas level or masl)

3.4 Methods

3.4.1 Field sampling and geochemical analyses

(Starr and Ingleton 1992)Additional sampling was conducted at for pore water, groundwater, and pore gas in 2021 and 2022. Results from three previous sampling events in 2018 were also incorporated into the data analysis. Pore-gas O_2 and CO_2 concentrations from multi-depth gas-sampling ports were measured by a field O_2/CO_2 analyzer (Quantek Instruments 902P). To obtain gas concentrations from shallow depths in the upper sand layer, hollow-stem steel rods were inserted into the ground at fixed depths and attached under suction to a field O_2/CO_2 analyzer for pore-gas measurements.

The pH and Eh were measured on unfiltered samples in the field with electrodes (Thermo Orion Ross Ultra pH Electrodes and Orion Redox/ORP Electrodes) and meters (Thermo Orion Star A221 Portable Meters). Alkalinity was measured in the field using a Digital Titrator (Hach model 1690001) with 0.16 N or 1.6 N sulfuric acid cartridge and bromocresol green-methyl red indicator powder on filtered (0.45 µm) water samples.

Samples for dissolved cation analysis were field filtered (0.45 µm) and preserved with HNO_3 to pH<2; samples for dissolved anions were field filtered; samples for dissolved organic carbon (DOC) were field filtered and preserved with H_2SO_4; samples for stable carbon isotope and sulfur isotope were field filtered. Major cations were analyzed by inductively coupled plasma-optical emission spectrometry (ICP-OES, Thermo iCAP 6000) following the United States Environmental Protection Agency (U.S. EPA) method 200.7 (U.S. EPA 1994a). Trace cations were analyzed by inductively coupled plasma-mass spectrometry (ICP-MS, Thermo X Series 2) following EPA 200.8 (U.S. EPA 1994b). Major anions were analyzed by ion chromatography (IC, Dionex DX-600) following EPA 300.0 (U.S. EPA 1993). DOC was analyzed with a 1030W TOC Analyzer (Aurora).

For selected aqueous samples at KK3, $\delta^{13}C$ (DIC) analysis was conducted at the Environment Isotope Laboratory (EIL), University of Waterloo, using an Isotope Ratio Mass

Spectrometer (IRMS; MicroGas-IsoPrime). Peat samples were collected from cores and analyzed for $\delta^{13}C$ by a continuous flow isotope ratio mass spectrometer (GVI IsoPrime) at the EIL. Both aqueous and solid-phase $\delta^{13}C$ results were reported relative to Vienna Pee Dee Belemnite (‰VPDB) with a precision of 0.2‰. Sulfate isotope ($\delta^{34}S$-SO_4) on aqueous samples was conducted at EIL using a continuous flow isotope ratio mass spectrometer (CFIRMS; Micromass Isochrom). $\delta^{34}S$ results were reported relative to Vienna Canyon Diablo troilite (VCDT) reference standard values with a precision of 0.3‰.

Mineral saturation indices (SI) were calculated using PHREEQC 3.6.2 (Parkhurst and Appelo 2013) with the WATEQ4F database (Ball and Nordstrom 1991) to gain insights into the tendency of primary and secondary-mineral dissolution and precipitation.

3.4.2 Chemical extractions

Five-step non-sequential selective chemical extractions were performed on tailings samples from cores collected in October 2017. Tailings samples of approximately 1 g for each extraction step were collected at specified depths of the cores in an anaerobic chamber. Gravimetric water content at each sampling depth was also determined. The steps of the extractions were consistent with those outlined in Gunsinger et al. (2006) and summarized in Table 3-1.

The first extraction used anoxic deionized (DI) water purged with Ar to target water-soluble phases and weakly adsorbed elements. The second extraction targeted phases that mobilize under alkaline conditions, such as insoluble sulfates and adsorbed oxyanions. The third extraction utilized a weak reducing agent, ascorbate, consisting of 0.12 M Na-ascorbate, 0.6 M Na-bicarbonate, and 0.17 M Na-citrate, to target amorphous oxyhydroxides. The fourth extraction used a strong reducing agent 2M hydroxylamine hydrochloride [$NH_2OH{\cdot}HCl$] with 25 vol% acetic acid, abbreviated as HHCl, to target all reducible oxyhydroxides. The fifth extraction targeted phases that mobilize under acidic conditions. The first three extractions were performed in an anaerobic chamber, whereas the fourth was heated in a fume hood.

All solid masses were corrected for gravimetric water content. All final concentrations were corrected for pore-water chemistry using the results from October 2017 field sampling; when pore-water concentrations from an extraction depth were not available, linear

interpolation between depths was performed. Cation samples for the second and third extractions were preserved with HNO_3 and the results were corrected for the volume of acid added.

Table 3-1. 5-step chemical extractions (Gunsinger et al. 2006).

Reagent	Solid: Reagent Ratio	Digestion (hr)	Target	Reference
DI water purged with Ar	1:50	24	Water-soluble	(Ribet et al. 1995)
0.3 M NaOH	1:30	16	Insoluble sulfates	Yin and Catalan (2003)
0.12 M Na-ascorbate, 0.6 M Na-bicarbonate, 0.17 M Na-citrate	1:20	24 in the dark	Amorphous oxyhydroxides	Amirbahman et al. (1998)
2 M hydroxylamine hydrochloride (HHCl) in 25% acetic acid	1:30	24 at 95°C	Amorphous and crystalline oxyhydroxides, adsorbed (all reducible oxyhydroxides)	Ribet et al. (1995)
0.5 M HCl	1:10	24	Poorly crystalline, adsorbed, carbonate (acid-soluble)	Heron et al. (1994)

3.4.3 Mineralogical analyses

Additional whole rock X-ray fluorescence (XRF) analysis was conducted for selected tailings samples, which were pulverized and compressed into XRF pellets, then analyzed using PANalytical MiniPal 4. KK4 tailings samples of approximately 5 g were subsampled from the cores at specific depths in an anaerobic chamber and freeze-dried (Labconco FreeZone 1-L Benchtop Freeze Dry System). Dried samples were sent to Spectrum Petrographic (Vancouver, Washington, USA) to prepare polished grain-mounted slides embedded in epoxy on Suprasil 2A Quartz glass in the absence of O_2 or water. Previous XRD and C/S results (§1.3) were also included in the data analysis.

Thin sections were examined with an optical microscope (Nikon Eclipse LV100POL) under plain-polarized reflected and transmitted light. Selected locations of interest were imaged with backscattered electrons and analyzed for elemental composition using scanning electron microscopy / energy dispersive X-ray (SEM/EDX, Hitachi TM3000). Based on the oxidation status of sulfide minerals identified through optical microscopy and SEM/EDX, the sulfide alteration index (SAI) for each depth was interpreted based on the guidelines proposed by Blowes and Jambor (1990) and modified by Moncur et al. (2005, 2009).

Boulder-size waste rock was collected during excavation in October 2017. Selected samples were analyzed for whole rock elemental composition by XRF (PANalytical MiniPal 4). Standard polished thin sections of four crushed waste-rock samples, two sulfide-rich and two low-sulfide, were prepared by Vancouver Petrographic (Langley, BC).

3.4.4 Synchrotron-based X-ray microprobe analyses

X-ray absorption spectroscopy (XAS) measurements were performed at the Sector 20 beamline at the Advanced Photon Source (APS) of the Argonne National Laboratory via remote access in April 2022. The samples were KK4 thin sections (polished grain-mounted slides on quartz glass and embedded in epoxy) at depths of 1.65 m and 2 m. Data were collected using a microprobe for micro X-ray fluorescence (μXRF) mapping with a spot size of 1.3 μm x 2 μm at areas of interest on these thin sections. Micro X-ray absorption near edge structure (μXANES) spectra were subsequently collected at selected spots using the fluorescence signal. μXANES for As K-edge were collected between 11667 and 12110 eV with a step size of 10 eV from 11667 to 11847 eV and a step size of 0.5 eV from 11847 to12110 eV near the As K-edge (11867 eV). Two-to-three spectra were collected for each spot.

μXANES measurements of KK4 thin sections at depths of 1.65 m and 2.45 m were performed at the SXRMB beamline at the Canadian Light Source (CLS) in Saskatoon, Canada on August 27, 2022. A spot size of 10 μm x 10 μm was used. μXANES spectra for Fe K-edge were collected between 7082 and 7262 eV with a step size of 1 eV from 7082 to 7106 eV, a step size of 0.35 eV from 7106 to 7137 eV near the Fe K-edge (7112 eV), and a step size of 0.75 eV from 7137 to 7262 eV. μXANES spectra for S K-edge were collected

between 2442 and 2560 eV with a step size of 1 eV from 2442 to 2466 eV, a step size of 0.15 eV from 2466 to 2497 eV near the S K-edge (2472 eV), and a step size of 0.75 eV from 2497 to 2560 eV. Two spectra were collected for each spot.

μXRF data were processed and visualized using PyMca (Solé et al. 2007). The data were calibrated for K-edge peaks for known elements and normalized against the incident energy (I_0). Normalized intensity was mapped for key elements of interest such as As, Fe, Cu, and Zn.

The sequential μXANES spectra were merged into one spectrum, corrected for dead time and glitches, and normalized with Larch (Newville 2013). The spectra were calibrated using reference spectra for As, Fe, and S K-edge, which were acquired at the same beamline as the samples, acquired during previous synchrotron experiments by other members of our research group, or downloaded from the European Synchrotron Radiation Facility (ESRF) (ESRF ID21 2022). Linear combination fitting (LCF) was implemented in Larch to estimate the fraction of each As, Fe, or S species in the sample spectra. The best-fit spectra were chosen based on the likely components and minimal X^2 values.

3.5 Results and discussion

3.5.1 Pore gas

Pore-gas results were presented in section 2.5.3 and summarized here. Oxygen transport provides the driving force for sulfide oxidation in the tailings, which leads to subsequent geochemical and mineralogical changes. At KK3, O_2 concentrations decreased and CO_2 concentrations increased with depth across the GCL during all sampling events (Figure 3-3). Pore-gas O_2 concentrations were low (minimum 5 vol.%) above the waste rock, which suggests that the cover restricted atmospheric O_2 ingress. Carbonate mineral dissolution and organic carbon oxidation likely produced CO_2 and consumed O_2 in the subsurface. The limited O_2 availability at the KK3 waste rock and tailings could effectively lower the sulfide oxidation rate.

At KK4, a significant decrease in O_2 concentrations with depth was only recorded in May 2022, when O_2 concentrations were near 0 vol.% and CO_2 concentrations reached 10 vol.% in the waste rock and the tailings (Figure 3-3). During most sampling events in the summer

and early fall, O_2 concentrations in the tailings were intermediate (10-15 vol.%). Near-atmospheric (20.9 vol.%) O_2 concentrations in the tailings were observed in November 2021 with minimal change with depth. The intermediate to high O_2 concentrations recorded at multiple sampling events suggest that local defects in the cover, which may be due to imperfections during construction, inadequate sealing following instrument installation, or deterioration of materials over time, likely existed, which allowed atmospheric O_2 ingress into the tailings.

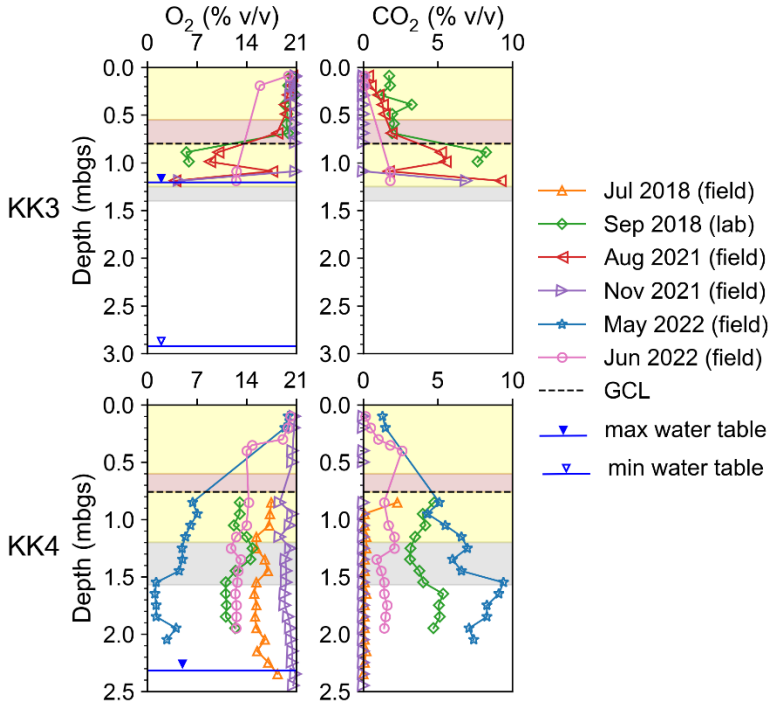

Figure 3-3. O_2 and CO_2 concentration profiles at KK3 and KK4. Data were from Chapter 2 (Figure 2-16). Background colours represent different layers: yellow for sand, brown for clay, black dashed line for GCL, grey for waste rock, white for tailings, green for peat, and tan for quaternary sand.

3.5.2 Mineralogy and solid-phase geochemistry

XRD analysis of the unoxidized tailings of KK3 and KK4 indicates the presence of pyrite, quartz, calcite, plagioclase (albite and anorthite), amphibole, muscovite, and chlorite (Figure 3-4). In addition, accessory amounts of K-feldspar, siderite, and dolomite are sparsely

present. For unoxidized tailings, pyrite accounts for up to 44 wt% at KK4, up to 59 wt% at KK4, and up to 74 wt% at KK5.

Assuming sphalerite, chalcopyrite, and arsenopyrite accounted for all solid-phase Zn, Cu, and As, XRF results at the deepest tailings of KK3, KK4 and KK5 indicate that sphalerite accounted for around 0.3 wt%, chalcopyrite accounted for approximately 1 wt%, and arsenopyrite accounted for approximately 0.5 wt%. SEM/EDX results suggest that Zn, Cu, and As were also present as trace components in pyrite and pyrrhotite (Appendix D). In contrast, calcite accounted for up to 2.6 wt% at KK3 and less than 1 wt% at KK4 and KK5. The overwhelming abundance of sulfide minerals compared to carbonate minerals indicates that the tailings are acid-generating.

In addition, XRF results show that in the unoxidized tailings, Co, Pb, Ni, Cr, and Cd accounted for approximately 740 ppm, 450 ppm, 120 ppm, 90 ppm, and 2 ppm, respectively. Discrete sulfide phases such as galena or pentlandite were not identified by optical microscopy or SEM/EDX; these elements were likely present as impurities and trace components in the principal sulfides. SEM/EDX analysis identified Pb, Ni, and Co in unoxidized pyrite and pyrrhotite (Appendix D).

At KK3, extensive oxidation of the shallowest 0.25 m of the tailings occurred the tailings were exposed to the atmosphere over more than four decades before cover placement. This oxidized zone was characterized by an ocherous colour, depletion of pyrite, and enrichment of secondary minerals such as Fe_2O_3 (hematite and maghematite) and gypsum (Figure 3-4). Below the oxidized zone, pyrite content gradually increased until it reached around 40 wt% at 0.5 m below the top of the tailings. Pyrite content decreased at the bottom of the tailings bordering the underlying peat. A mixture of natural sediments in the tailings likely resulted in a lower sulfide content.

At KK4, the oxidized zone was approximately 0.1 m deep and it was characterized by a thin hardpan around 1.6-1.65 meters below ground surface (mbgs), or 0.03-0.08 m below the top of the tailings, which was mainly comprised of Fe_2O_3 and gypsum (Figure 3-4). Optical microscopic study and SEM/EDX analysis showed almost no occurrence of sulfides at 1.65 mbgs (Figure 3-5a). The only remnant pyrite grains were those encapsulated in ilmenite and thus not susceptible to oxidation. Abundant Fe(III) oxyhydroxides of various

crystallinity, including Fe_2O_3, goethite, and ferrihydrite, were observed. Clusters of sub-micron jarosite grains were present at the centre of Fe(III) oxyhydroxides (Figure 3-5b). EDX analysis indicated the association of Si, Al, Pb, As, Co, Cu, and other trace elements in Fe oxyhydroxides and jarosite (Appendix D).

At 1.8 mbgs of KK4 (0.23 m below the top of the tailings), pyrite content abruptly rose to 59% (Figure 3-4). Photomicrographs and SEM/EDX revealed abundant pyrite and chalcopyrite grains, which appeared to have undergone congruent dissolution along the fractures and rims (Figure 3-5c). These grains were separated into smaller pieces without alteration rims. Low pore-water pH likely facilitated rapid and congruent microbially mediated oxidative dissolution of sulfides (Pakostova et al. 2020). No sphalerite was found at this depth. Sphalerite was more susceptible to oxidative dissolution than pyrite and chalcopyrite (Moncur et al. 2009, Bao et al. 2022).

At 2.0 mbgs (0.43 m below the top of the tailings), pyrite content was around 30%. Unaltered sphalerite grains were observed, along with abundant secondary covellite, such as those surrounding the sphalerite grain (e.g., Figure 3-5d). Copper derived from chalcopyrite weathering can precipitate as covellite under reducing conditions (Boorman and Watson 1975, Blowes et al. 2014). Abundant covellite suggests that at a depth of 2.0 m, there was a transition between oxidized and reduced zones. Some pyrite grains showed signs of early-stage oxidation with thin alteration rims, while some pyrite grains showed thicker rims of secondary-mineral precipitates (e.g., Figure 3-5e). Unaltered arsenopyrite was also present as inclusions in a large pyrite grain (Appendix D).

At 2.2 mbgs (0.63 m below the top of the tailings), minimal oxidation of pyrite and chalcopyrite was observed. Complete pyrrhotite was not found, instead, marcasite and Fe oxyhydroxide pseudomorphs after pyrrhotite were present (Figure 3-5f).

At 2.45 mbgs (0.88 m below the top of the tailings), pyrrhotite was more abundant than above and displayed varying degrees of oxidation. Some pyrrhotite grains were intensely altered (Figure 3-5g), some showed alteration along the basal parting, rim, or fractures, whereas others contained unaltered cores (Figure 3-5h). Individual arsenopyrite grains were present but contained alteration rims (Figure 3-5i). SAI values along the KK4 depth profile were assigned and summarized in Figure 3-6.

Extensive heterogeneity was present in the waste-rock mineralogy, with S content ranging from 0.2 to 26 wt%, C content ranging from 0.5% to 5%, Fe between 0.001 and 20 wt%, Cu between 250 and 10,000 ppm, and Zn ranging from 250 to 1000 ppm. The potential for acid generation and element release in the waste rock varied spatially.

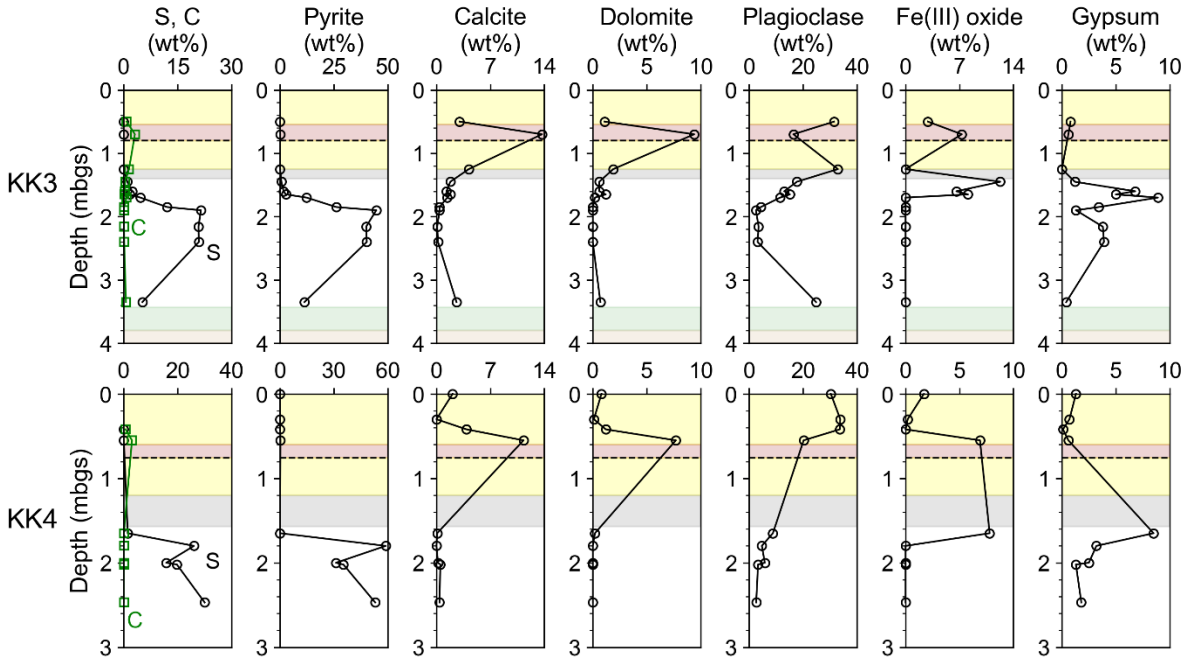

Figure 3-4. Depth profiles of C/S concentrations and major crystalline phases at KK3 and KK4. Background colours represent different layers: yellow for sand, brown for clay, black dashed line for GCL, grey for waste rock, white for tailings, green for peat, and tan for quaternary sand.

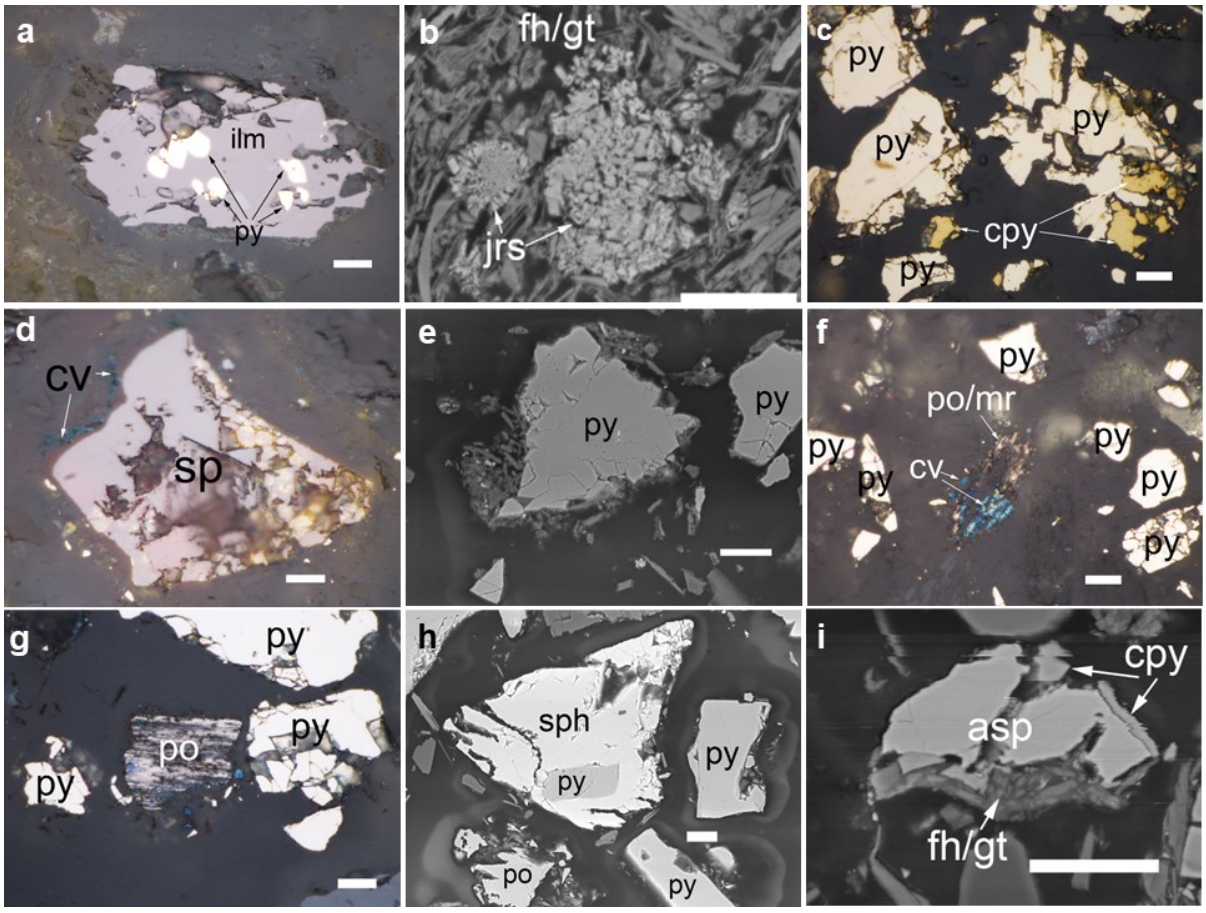

Figure 3-5. Photomicrographs under plain reflected light (a, c, d, f, g) and scanning electron microprobe (SEM) backscattered electron (BSE) images (b, e, h, i) of polished grain-mounted thin sections of KK4 tailings between depths of 1.65 and 2.45 meters below ground surface (mbgs). Each white scale bar represents 10 μm. Py=pyrite, ilm= ilmenite, jrs=jarosite, fh=ferrihydrite, gt=goethite, cpy=chalcopyrite, cv=covellite, sph=sphalerite, po=pyrrhotite, mr=marcasite, asp=arsenopyrite. (a) At 1.65 mbgs, remnant pyrite inclusions in ilmenite; no individual sulfide grains were present at this depth. (b) At 1.65 mbgs, a jarosite cluster surrounded by Fe oxyhydroxides. (c) at 1.8 mbgs, pyrite and chalcopyrite grains displaying congruent dissolution along fractures and rims. (d) At 2.0 mbgs, an unaltered sphalerite grain surrounded by covellite. (e) At 2.0 mbgs, left: pyrite displaying oxidation with a rim of Fe oxyhydroxides and hydroxysulfates; right: pyrite without alteration. (f) At 2.2 mbgs, a marcasite and Fe oxyhydroxide pseudomorph after pyrrhotite with covellite precipitated on top. (g) At 2.45 mbgs, a pyrrhotite grain with intensive alteration to marcasite and Fe oxyhydroxides, surrounded by unaltered pyrite grains. (h) At 2.45 mbgs, an unaltered sphalerite grain with pyrite inclusion; a pyrrhotite grain showing alteration to Fe oxyhydroxides along the rim and fractures, but with an unaltered core. (i) At 2.45 mbgs, arsenopyrite with a rim of Fe oxyhydroxides at the bottom and minor intergrown chalcopyrite.

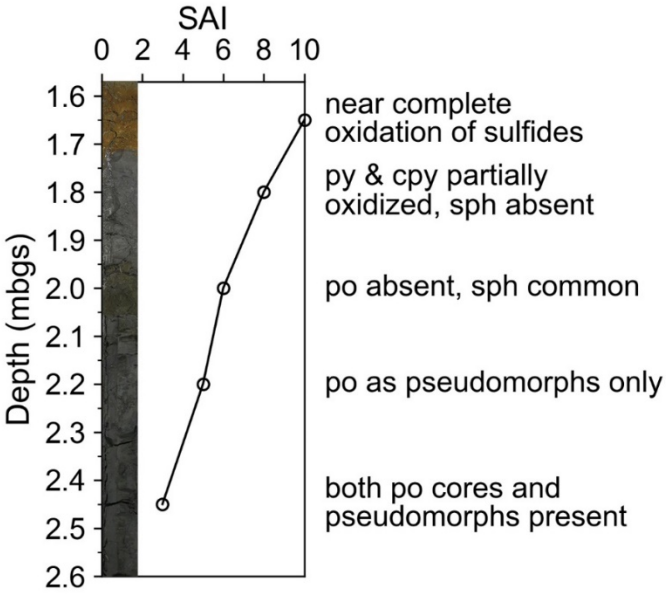

Figure 3-6. The photo represents the cross-sectional view of cores collected at KK4 tailings and the graph represents corresponding mineral changes quantified by sulfide alteration index (SAI) after Blowes and Jambor (1990), Moncur et al. (2005, 2009).

3.5.3 Aqueous geochemistry

At KK3, seasonal water-table fluctuation was up to 1.7 m (Figure 3-7). Groundwater at KK4 was also hydraulically replenished by uncontaminated water outside the impoundment (see Chapter 2). In the cover layers, pH was neutral and major and trace ion concentrations were low and similar to shallow infiltrated rainwater. The pore water was saturated with respect to calcite and dolomite, indicating the occurrence of carbonate mineral dissolution.

Pore-water pH in the tailings remained circumneutral throughout the monitoring period and the pore water was near-saturated with respect to calcite, dolomite, and siderite, indicating that the pore water was well buffered by carbonate dissolution. Fresh groundwater from outside the impoundment may have replenished the alkalinity at KK3. All metal(loid) concentrations in the tailings, including Al, Fe, Cu, Zn, Co, and Mn, were lower than other sampling locations in the impoundment, with the exception of As. In 2018, the pore-water As concentrations peaked (up to 4 mg L^{-1}) at around 2 mbgs within the zones of seasonal water-table fluctuations. However, As concentrations declined sharply in 2021 and 2022. No

notable difference in Eh is observed between the cover and the tailings. Eh values were much higher in 2018 (300-500 mV) than in 2021/2022 (<200 mV); one likely cause is inconsistencies in calibration and field measurement procedures; alternatively, the results suggest that the cover likely contributed to the shift to lower redox conditions over time. Additionally, measured Eh values indicate that strongly reducing conditions were not present during the sampling events.

The pore water was near- or super-saturated with respect to ferrihydrite and gibbsite; these two phases likely contributed to the attenuation of metal(loid)s in the tailings via co-precipitation and sorption. Sulfate (SO_4) concentrations were high, and the pore water and groundwater approached saturation with respect to gypsum (Figure 3-7). Compared to other weathered tailings sites (e.g., Moncur et al. 2005, Gunsinger et al. 2006), SI values for ferrihydrite were much higher in 2018 at KK3; these values are likely an artifact of high Eh measurements and low aqueous Fe concentrations. Ferrihydrite SI values in 2021 and 2022 are in the range of literature values.

Compared to the tailings above, the peat was characterized by lower δ^{13}C-DIC values, higher alkalinity, low concentrations of SO_4 and trace metal(loid)s, and moderately higher δ^{34}S-SO_4 isotope ratios (Figure 3-7). In May 2018, high DOC was present; lower concentrations were observed in subsequent sampling. The mean solid-phase δ^{13}C for the four peat samples was -25‰ VPDB.

Groundwater in the quaternary sand aquifer was characterized by circumneutral pH and elevated concentrations of Fe, SO_4, Ca, and Mn throughout 2018. Groundwater approached saturation with respect to calcite, dolomite, and siderite with depth. The geochemical data in the quaternary sand aquifer is consistent with a well-developed groundwater plume impacted by AMD. In 2021 and 2022, SO_4 and metal(loid) concentrations declined from previous years, especially at 3.9 mbgs. One possible reason for the decline is that the AMD plume was gradually flushed out by the uncontaminated eastward flow of groundwater, containing lower concentrations of dissolved metals, during most of the year (see 2.5.1.1). High δ^{34}S-SO_4 isotope ratios were present in November 2021 and June 2022.

Kinetic fractionation of S isotopes (^{32}S and ^{34}S) during bacterially mediated sulfate reduction (eq. 3-3) in the presence of organic carbon results in higher δ^{34}S in the remaining

sulfate (Seal 2006). Oxidation of ^{13}C-depleted organic carbon in the peat likely produced the low $\delta^{13}C$-DIC isotope ratios and high alkalinity. A combination of low $\delta^{13}C$-DIC and high $\delta^{34}S$-SO_4 isotope ratios indicates the occurrence of sulfate reduction in the peat and the underlying sand aquifer. Because sulfate and metal concentrations in the peat were low across all sampling events, significant sulfate reduction and metal-sulfide precipitation (eq. 3-4) occurred in the peat in the past, suggesting that the extent of sulfate reduction reactions has declined, resulting in less $\delta^{34}S$-SO_4 isotope fractionation. In addition, slower rates of sulfate reduction result in larger fractionation (Goldhaber and Kaplan 1975). These trends are consistent with the lateral migration of water impacted by sulfate reduction from the adjacent surface water flow system. Low DOC values during most of the sampling events suggest organic carbon may have been depleted and DOC concentrations may not be sufficient to sustain continued sulfate reduction.

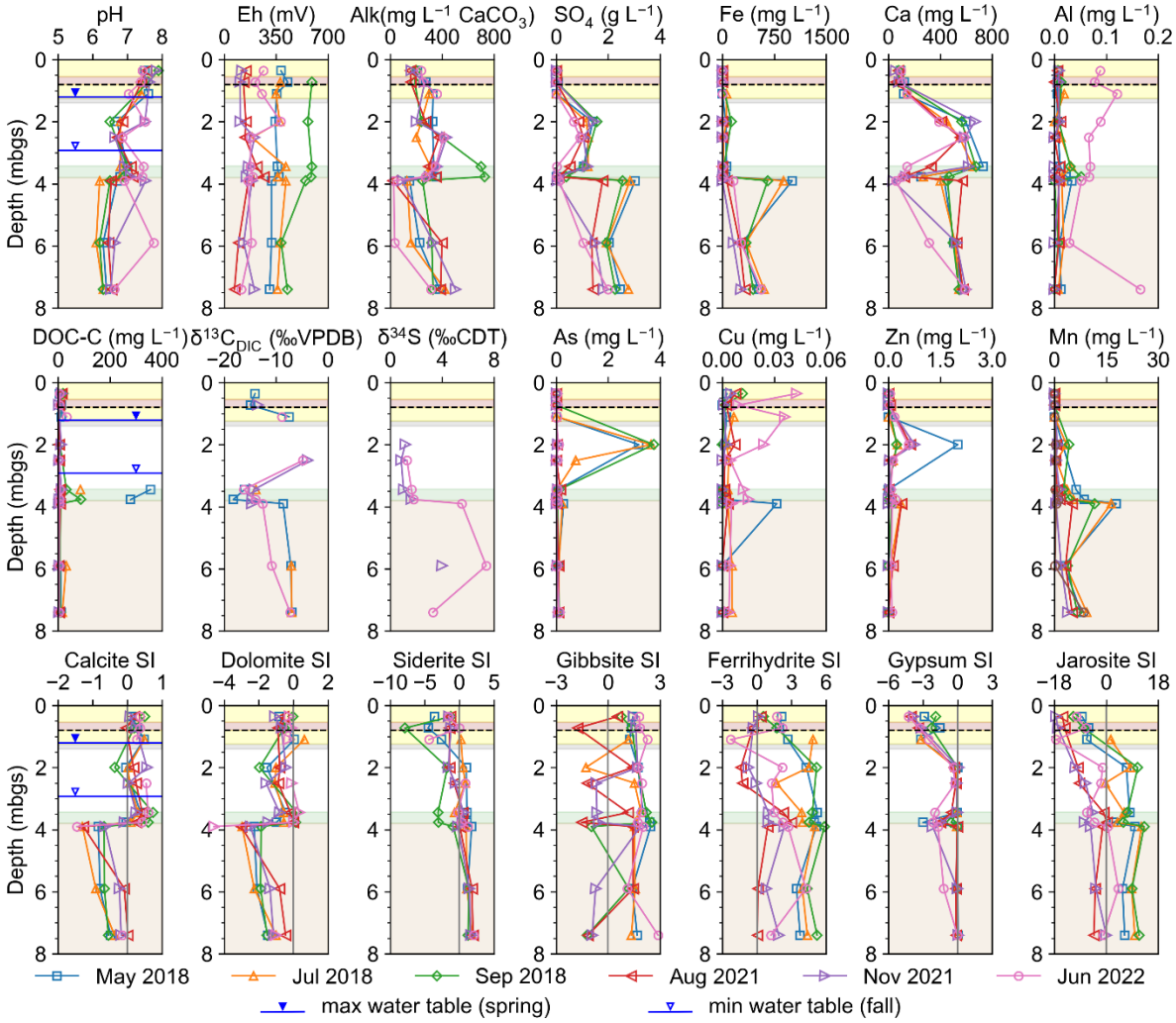

Figure 3-7. Vertical profiles of aqueous geochemical results and calculated saturation indices (SI) at KK3 from six pore water and groundwater sampling events. Background colours represent different layers: yellow for sand, brown for clay, black dashed line for GCL, grey for waste rock, white for tailings, green for peat, and tan for quaternary sand.

At KK4, tailings directly overlie bedrock outcrop. The water table was below 3 mbgs during summer and fall and rose to around 2.3 mbgs in the spring. Pore-water pH remained neutral in all cover layers. Pore water in the waste rock contained elevated concentrations of SO_4, Ca, and Zn but remained saturated with respect to calcite and dolomite (Figure 3-8). This combination indicates that oxidation of sulfide minerals, particularly sphalerite, released SO_4 and dissolved metals, and that the pore water pH was neutralized by the dissolution of

carbonate minerals which maintained circumneutral pH. The concentration of Fe was low and the pore water was near equilibrium with respect to ferrihydrite, which attenuated Fe under neutral pH. The pore water in the waste-rock layer was near equilibrium with respect to gypsum, suggesting that gypsum precipitation limited dissolved SO_4 concentrations. There are no apparent solid-phase controls on Zn concentrations.

In the tailings at KK4, low pore-water pH (as low as 2.2) was present along with low or depleted alkalinity and elevated aqueous concentrations of SO_4, Ca, Fe, Al, and trace metal(loid)s As, Cu, Zn, Co, and Pb during most sampling events (Figure 3-8). Compared to the 2018 sampling events, pore-water pH declined in 2021 and 2022, which indicates ongoing sulfide oxidation and corresponding production of acidity. Compared to previous sampling events, the lowest pH occurred deeper in the tailings in June 2022, indicating a downward migration of the oxidation front. Eh values were much higher at KK4 than at KK3. SO_4 concentrations were ubiquitously high in the tailings. Although the pore water was saturated with gypsum, aqueous SO_4 remained generally >2 g L^{-1}.

Tailings pore water was undersaturated with respect to calcite and dolomite; pore water was saturated with respect to siderite in 2018 but became undersaturated in 2021 and 2022. The SI results indicate that carbonate dissolution was favoured under low pH conditions. Elevated concentrations of Al (up to 125 mg/L) were present in the pore water. Similar to other studies (e.g., Moncur et al. 2005), gibbsite or other Al hydroxide phases were not identified by mineralogical analyses, but their presence and importance in controlling aqueous Al concentration are inferred. Gibbsite was not present in the host rock; it is an assumed secondary phase resulting from the dissolution of aluminosilicate minerals such as anorthite, albite, and muscovite. Subsequent precipitation of gibbsite and other Al hydroxide phases occurs when the pore-water pH is higher (>5) (May et al. 1979). Apart from July 2018, tailings pore water was largely undersaturated with respect to gibbsite, suggesting that the acid-neutralization capacity of gibbsite became depleted. The pore water was near-saturated with respect to ferrihydrite in 2018 and became undersaturated with respect to ferrihydrite in 2021 and 2022. Under low pH conditions in 2021 and 2022, the dissolution of Fe (oxy)hydroxides likely contributed to acid neutralization in the tailings.

Elevated Fe concentrations (up to 1.7 g/L) were present in the tailings pore water. Peak aqueous concentrations of Fe, Cu, Pb, Co, and Ni occurred at or below the depth of the lowest pore-water pH. The trace metals were likely liberated through a combination of sulfide oxidation, desorption from Fe (oxy)hydroxides, and acidic dissolution of (oxy)hydroxides. High Zn and Mn concentrations were ubiquitous in the tailings and did not show consistent depth patterns. Peak As concentrations occurred just below the depth of the lowest pH. Pore-water As concentrations were up to 50 mg/L, the highest of all locations at the site. In contrast to other trace metal(loid)s, As concentrations decreased between 2018 and 2021/2022; this is likely due to enhanced adsorption of As oxyanions to Fe(III) oxyhydroxides or Al hydroxides under lower pH. The majority of adsorbed As under lower pH is likely As(V). Arsenate [$As(V)O_4^{3}$] has a higher affinity for sorption than arsenite [$As(III)O_3^{3-}$], especially under low pH (Dzombak and Morel 1991, Smedley and Kinniburgh 2002).

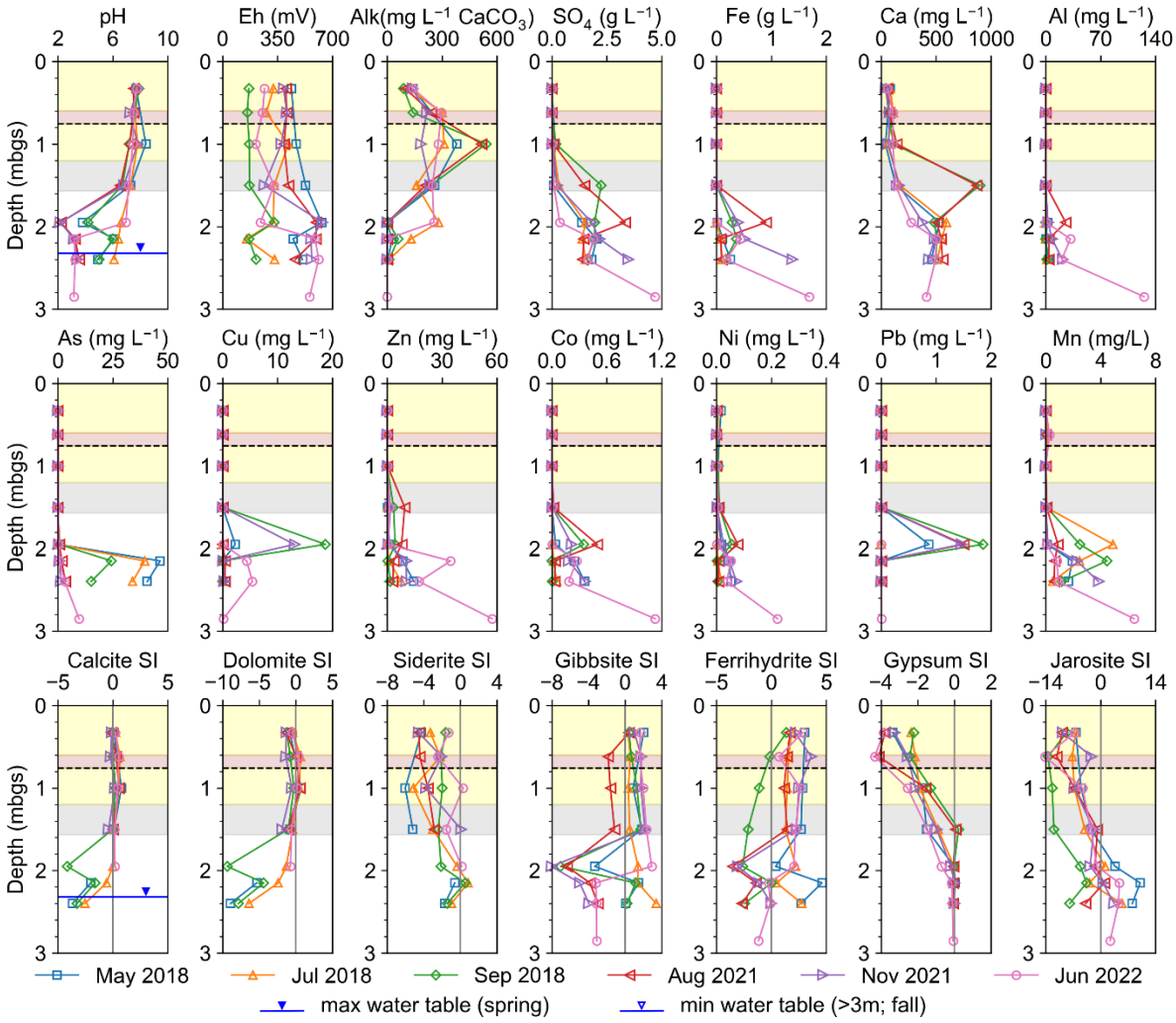

Figure 3-8. Vertical profiles of aqueous geochemical results and calculated mineral saturation indices (SI) at KK4 from six pore-water and groundwater sampling events. SI for carbonate minerals in the tailings could not be calculated for August and November 2021 due to depleted alkalinity. Background colours represent different layers: yellow for sand, brown for clay, black dashed line for GCL, grey for waste rock, and white for tailings.

3.5.4 Selective chemical extractions

Targeted extractions can assist in identifying mechanisms controlling trace metal(loid) concentrations and mobility under changing geochemical conditions and determining secondary phases associated with trace element sequestration. Results and interpretations

are comparable for all elements across different locations, so only data for KK4 are presented here and those for KK3 and KK5 are included in Appendix E.

Extractable Fe concentration is highest in the total reducible fraction (Figure 3-9), which mainly consists of crystalline oxyhydroxides. Except at the hardpan (1.65 mbgs), amorphous Fe oxyhydroxides are not abundant. The Fe concentrations in the total reducible and acid-soluble fractions peak at the hardpan and remain elevated deeper in the tailings (Figure 3-9). The low concentration of extractable Fe at 1.8 m depth is possibly due to low pore-water pH that did not favour Fe (oxy)hydroxide precipitation; this is consistent with the observation of congruent dissolution of sulfides at this depth (section 3.5.2). Speciation of Fe shows that ferrous iron (Fe(II)) is more abundant than Fe(III), even at the hardpan, and becomes increasingly dominant with depth. Ferrous iron in the acid-soluble fraction is mainly attributed to siderite. Although a small amount of pyrite may have partially dissolved in 0.5 M HCl (Rickard and Morse 2005), it is likely insignificant compared to carbonate (Lindsay et al. 2011), especially given the short extraction time. The increasing trend of Fe(II) with depth suggests the increasing presence of siderite with depth. Siderite was present in the original host rock (SENES Consultants Ltd. et al. 2000); as well, siderite can precipitate as secondary minerals following calcite and dolomite dissolution (Al et al. 2000).

Water-soluble and insoluble sulfates are comparable (Figure 3-9). Water-soluble Ca and sulfate share a similar decreasing trend with depth, which indicates the presence of gypsum, which is moderately soluble. K concentrations in the alkaline-soluble fraction peak at the hardpan, which indicates the presence of jarosite (Bigham and Nordstrom 2000).

Extractable Al is present in all fractions except the water-soluble extract. Both acid-soluble and alkaline-soluble Al concentrations increase with depth, but only acid-soluble Al is abundant at the hardpan (Figure 3-9). Al associated with acid-soluble and alkaline-soluble fractions is mainly attributed to gibbsite because gibbsite dissolution is favoured under acidic as well as strongly alkaline conditions (May et al. 1979). Acid-soluble Al at the hardpan is attributed to Al hydroxysulfate phases such as basaluminite and alunite, which tend to dissolve under low pH (Bigham and Nordstrom 2000). A considerable amount of Al is also associated with amorphous and crystalline Fe(III) oxyhydroxides.

Extractable As is significant in all fractions; as well, extractable and aqueous As peak at approximately the same depth (Figure 3-9); these data suggest that previously sequestered As can be easily liberated into the pore water under a variety of conditions, including alkaline, acidic, reducing, and high moisture content. Alkaline-extractable As is attributed to desorption from Fe oxyhydroxides and Al hydroxides, because arsenate and arsenite oxyanions tend to desorb under higher pH (Smedley and Kinniburgh 2002). Arsenite also desorbs under lower pH, which causes As release in the 0.5M HCl extraction. Partial dissolution of arsenopyrite is unlikely to be a significant source of acid-extractible As because As is slowly released from arsenopyrite oxidation (Blowes et al. 2014). Arsenic in ascorbate and HHCl extractions was liberated by the reductive dissolution of oxyhydroxides, which is a previously described mechanism of As release (Smedley and Kinniburgh 2002).

Extractable Cu associated with crystalline oxyhydroxides is the most abundant of all fractions, which is in low concentration at the hardpan but peaks at 2.45 mbgs (Figure 3-9). Acid-soluble Cu peaks at 2 mbgs, which corresponds to the observation of abundant covellite under reflected light optical microscopy (Figure 3-9). Covellite, a secondary sulfide formed under reduced conditions, is prone to acidic dissolution (Boorman and Watson 1975, Blowes et al. 2014), contributing to the acid-soluble Cu fraction. As well, the desorption of Cu from Fe oxyhydroxides and Al hydroxides contributes to Cu release under acidic conditions.

Extractable Zn concentration is only elevated at 2.45 mbgs associated with crystalline oxyhydroxides (Figure 3-9). Minimal Zn is present in amorphous oxyhydroxides. These results are consistent with the findings of Lindsay et al. (2011). Almost no Zn was released by desorption under acidic conditions, suggesting that Zn likely remains in solution or is co-precipitated with crystalline oxyhydroxides. Reductive dissolution of crystalline oxyhydroxides can release the incorporated Zn in significant amounts.

Extractable Pb and Mn associated with crystalline oxyhydroxides are the most abundant (Appendix E). Acid-soluble Pb and total reducible Pb both peak at the hardpan, suggesting that Pb sorbed to and co-precipitated with crystalline Fe oxyhydroxides and can be re-mobilized through desorption and reductive dissolution of Fe oxyhydroxides. Alkaline-extractable Pb at 1.8 mbgs is attributed to anglesite [$PbSO_4$], which is soluble under alkaline

and acidic conditions (Dove and Czank 1995) and a common weathering product of galena (Blowes et al. 2014). A small amount of Mn is in the water-soluble fraction. Cobalt does not show measurable sequestration in secondary phases.

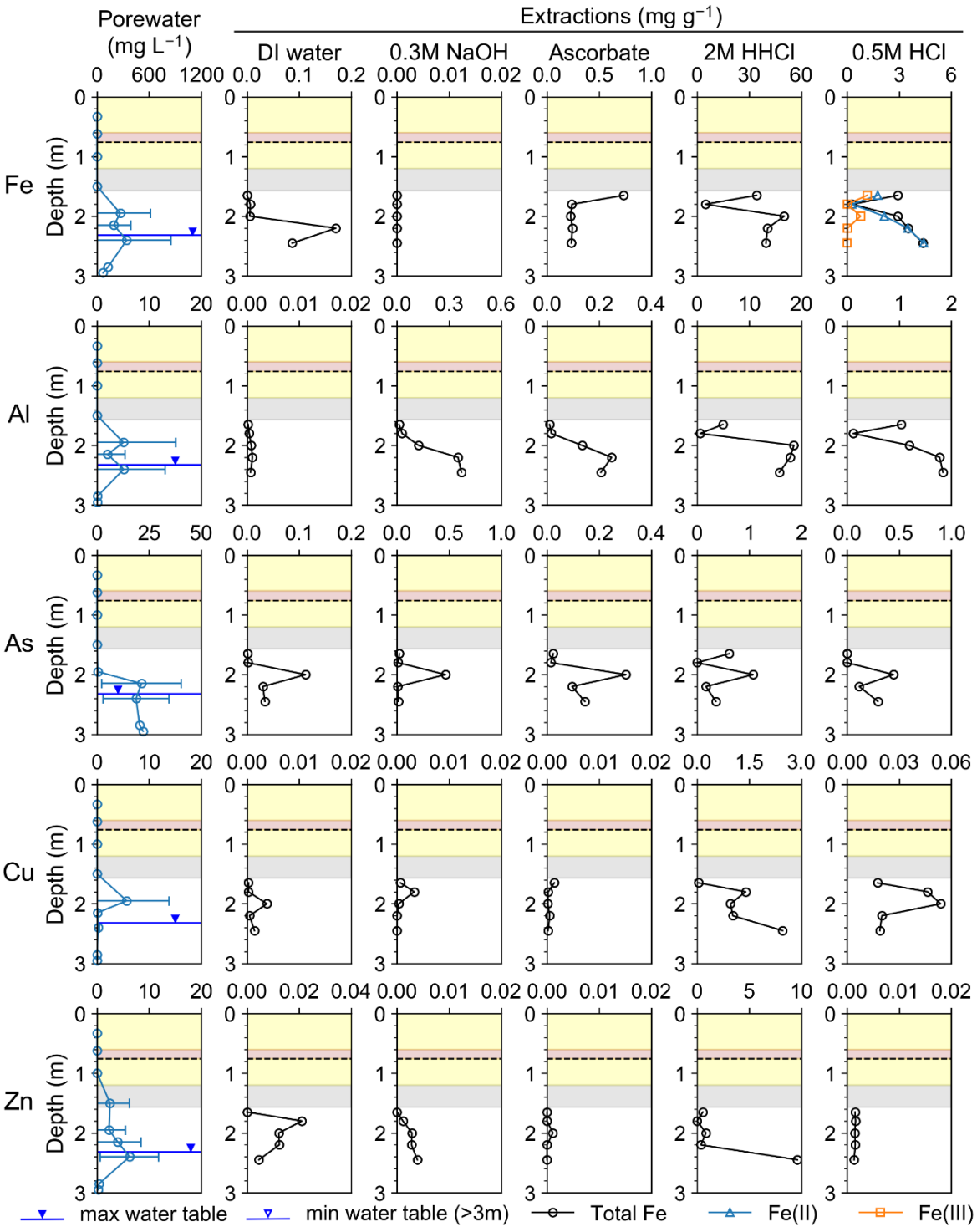

Figure 3-9. Selectively extracted Fe, Al, As, Cu, and Zn concentrations compared to aqueous concentrations at KK4.

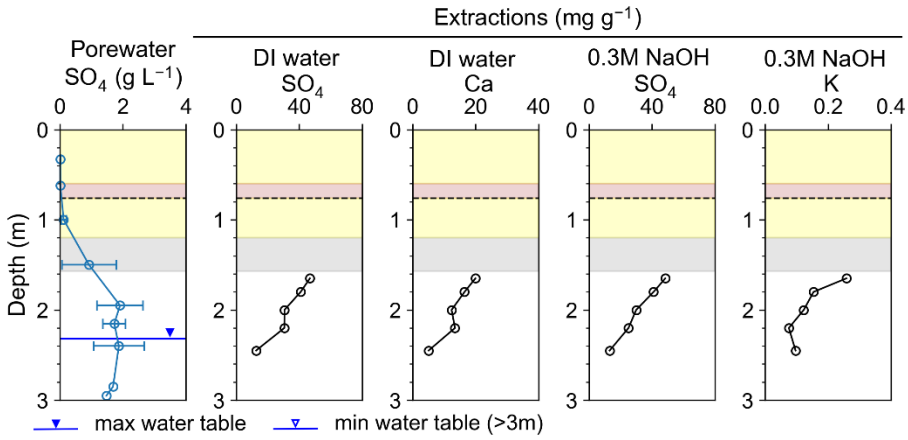

Figure 3-10. Selectively extracted SO_4, Ca, and K concentrations compared to aqueous SO_4 concentrations at KK4.

3.5.5 Synchrotron-based X-ray microprobe analyses

Synchrotron-based XAS techniques provide high-resolution information on the association and distribution of elements in tailings, as well as their oxidation state and bonding environment. μXRF maps at the 1.65 mbgs jarosite crystal aggregates demonstrate that As and Fe do not share the same spatial distribution pattern; solid-phase As concentrates at the periphery of jarosite (Appendix F). High concentrations of As partially coincide with the location of a Fe-rich oxidation rim surrounding a pyrite grain in the sample collected at 2.0 mbgs.

Linear combination fitting of the As standards included in the XANES spectra shows good fits to K-edge spectra for all samples (Figure 3-11) with χ^2 values between 8 x 10^{-4} and 3 x10^{-3}. The dominant phases present at 1.65 mbgs include scorodite [$FeAsO_4 \cdot 2H_2O$], arsenate (As(V)) bound to jarosite and arsenite (As(III)) bound to ferrihydrite (Figure 3-11a). The LCF fit for the 2.0 mbgs sample featuring an alteration rim surrounding a pyrite grain (Figure 3-11b) indicates less extensive oxidation than at the 1.65 mbgs sample, with dominant phases that include As(V)-bound to ferrihydrite, As(III) bound to ferrihydrite and lower abundances of scorodite and As(V) bound to jarosite. The double peaks in the spectrum of this sample were not well captured by LCF, suggesting the presence of an

unidentified As(III)-bearing phase. The majority of the As retained at depths of 1.65 m and 2.0 m is As(V), which occurred either as scorodite or as sorbed species to ferrihydrite or jarosite (Figure 3-11a &b). Scorodite precipitation is more favourable under very low pH (<2) and high aqueous As concentrations, whereas adsorption of As(V) is more favourable under higher pH (Bigham and Nordstrom 2000). Scorodite was not identified by optical microscopy or SEM/EDX; the local presence of scorodite on a micro scale is likely under the low pH and high pore-water As conditions within the tailings. Arsenite was more abundant within the alteration rim on pyrite than at the jarosite grain. Nevertheless, even at the oxidized hardpan (1.65 mbgs), about 15% of As was present as As(III), which demonstrates the persistence of As(III).

Linear combination fitting results of the As sulfide at 2.0 mbgs (Figure 3-11c) indicate that the main components include unoxidized arsenopyrite (around 70%), As(III) as orpiment [As_2S_3], As(III) sorbed to ferrihydrite, and trace amounts of As(V). Orpiment is found in the ore body, and it is also derived from the oxidation of arsenopyrite (Nordstrom and Archer 2003). The μXANES data suggest that the arsenopyrite grain has undergone minor oxidation.

All LCF fits, using the standards included in the data analysis, show good agreement with the Fe K-edge experimental data (Appendix F) with χ^2 values between 2×10^{-5} and 3×10^{-4}. For S K-edge, χ^2 values for LCF are between 1×10^{-3} and 4×10^{-2} (Appendix F). A profile of Fe and S μXANES LCF results through the alteration rim of a partially oxidized pyrrhotite grain at 2.45 mbgs indicate that from the interior of the grain (point a) to the grain boundary (point d), pyrrhotite was progressively altered to intermediate oxidation products, in the sequence: marcasite, ferrihydrite, and elemental S (Figure 3-12). Incorporation of traces of thiosulfate (1%) improved the LCF fit for S, however, thiosulfate was excluded from the reported fit results due to its low presence. Marcasite and elemental S are common intermediate or secondary species of pyrrhotite oxidation when the leaching rate is not rapid (Blowes et al. 2014). Thiosulfate is unstable under acidic conditions (Blowes et al. 2014). The abundance of marcasite and elemental S suggests that at 2.45 m, the sulfide oxidation rate was slow and mildly acidic pH was present.

Iron and S μXANES LCF results at a Fe(III) oxyhydroxide grain at the hardpan indicate the presence of a variety of Fe(III) oxyhydroxides and hydroxysulfates, including goethite, ferrihydrite, melanterite, lepidocrocite, jarosite, and Fe_2O_3 (Appendix F). Fe_2O_3 was scarce compared to less crystalline phases like goethite, lepidocrocite, and ferrihydrite.

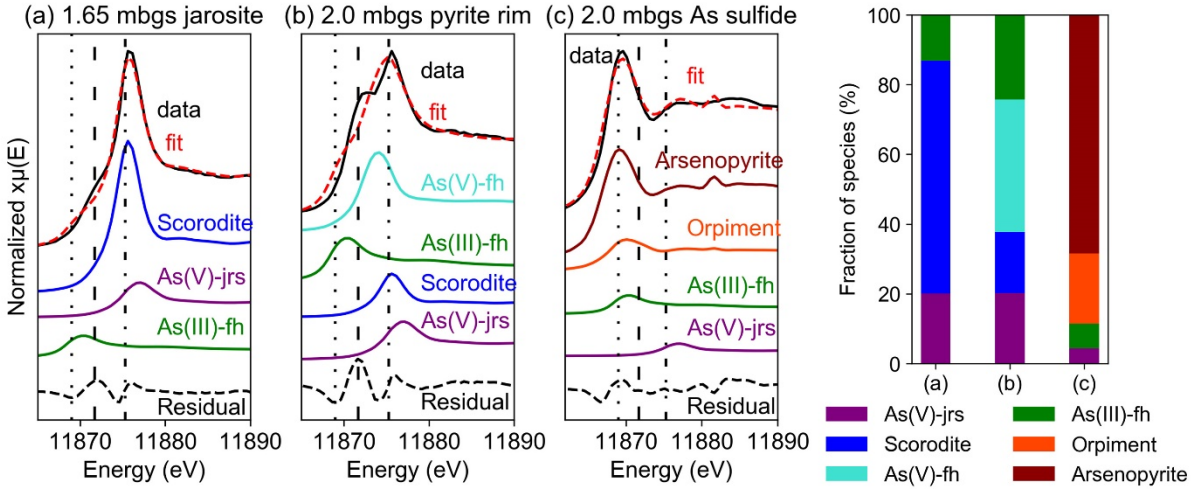

Figure 3-11. Arsenic μXANES linear combination fitting at three different grains at KK4: 1.65 mbgs (oxidized zone, hardpan) and 2.0 mbgs (transition zone between oxidized and reduced environment). Fh=ferrihydrite and jrs=jarosite. The vertical dotted line represents the white line for As sulfide (11869 eV), the dashed line represents the white line for As_2O_3 (11871.7 eV) and the dash-dotted line represents the white line for As_2O_5 (11875.3 eV) (Smith et al. 2005).

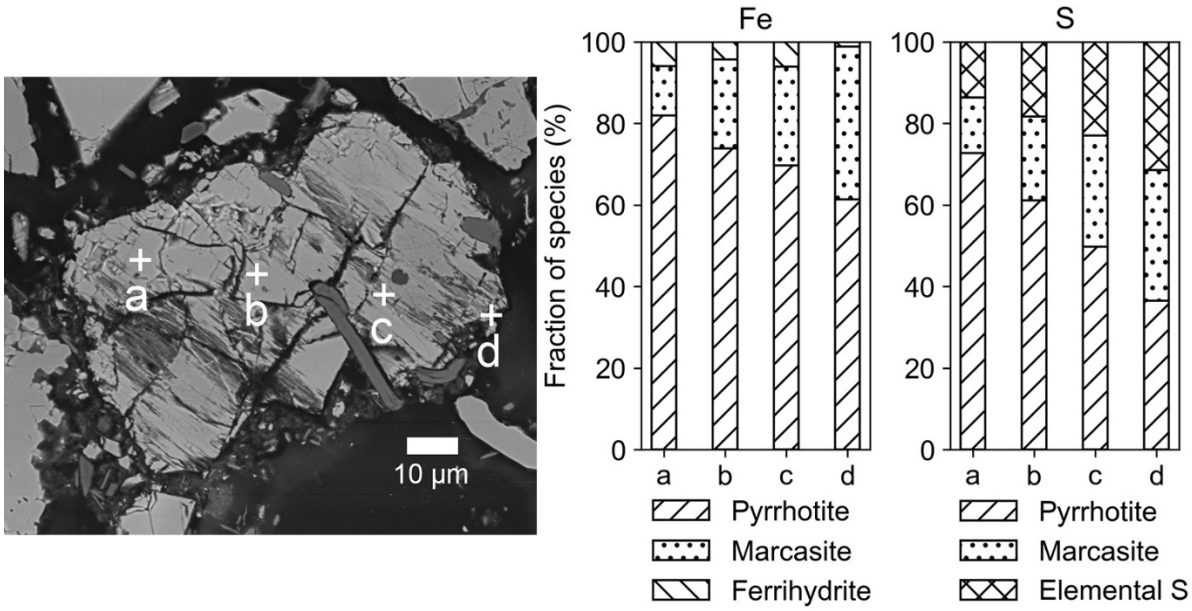

Figure 3-12. Iron and S µXANES linear combination fitting results at four spots across a pyrrhotite grain at 2.45 mbgs of KK4.

3.5.6 Sulfide oxidation under a composite cover

The presence of shallow (0.1-0.25 m) oxidized zones suggests that decades of subaerial sulfide oxidation did not deplete sulfide minerals extensively, likely due to the unusually high sulfide content and elevated water table at NIT. Nevertheless, sulfide oxidation resulted in an extensive zone of low pH pore water containing high elemental concentrations, which impacted groundwater in the underlying aquifer and persisted a decade after remediation by a composite cover. Mineralogical studies through optical microscopy and SEM/EDX suggest that the susceptibility of various sulfides to oxidation in the tailings is as follows: pyrrhotite > arsenopyrite > sphalerite > pyrite > chalcopyrite. This trend generally aligns with mineralogical studies from other tailings sites (Blowes et al. 2014).

Low O_2 concentrations at KK3 suggest that the composite cover limited O_2 transport into the tailings. Between 2018 and 2021/2022, aqueous elemental concentrations decreased and pH increased at KK3. The combination of pore-gas and aqueous geochemistry suggests that the cover reduced the rate of sulfide oxidation at KK3, thus lowering the acidity and metal(loid) leaching over time. Naturally occurring peat under the tailings also

promoted sulfate reduction in the peat and underlying quaternary sand aquifer, which further attenuated SO_4 and trace elements.

In contrast, moderate to high O_2 concentrations at KK4, observed during multiple sampling events suggest that potential defects in the cover may have developed during cover placement, during the installation of the instrumentation, and/or via material deterioration over time. These inferred imperfections in the cover correspond with lower pH pore water and higher concentrations of dissolved Fe and heavy metals at KK4 compared to KK3. Between 2018 and 2021/2022, elemental concentrations increased and pH decreased at KK4. The availability of O_2 at KK4 resulted in continued sulfide oxidation, acidity production, and metal(loid) leaching. The thin hardpan 0.08 m below the top of the tailings did not act as an effective O_2 transport barrier since it was friable and porous despite the abundance of a variety Fe(III) oxyhydroxides, Fe(II) and Fe(III) hydroxysulfates, and other secondary phases. The zone of active oxidation was around 0.23 m below the top of tailings at KK4, where abundant pyrite and chalcopyrite and low pH conditions, along with a lack of alteration rims or secondary Fe(III) oxyhydroxides, result in rapid sulfide oxidation and metal leaching rates. Around 0.43 m below the top of the tailings was a transition zone between the oxidative and the reductive zones of the tailings characterized by abundant covellite. Deeper in the tailings (0.88 m below the top of the tailings), the leaching rate was low and abundant pyrrhotite grains were abundant and secondary and intermediate oxidation products were observed.

The pre-oxidized waste rock in the cover may have locally undergone continued sulfide oxidation, which resulted in high Zn and SO_4 concentrations at the KK4 waste rock. Carbonate, especially calcite, dissolution maintained circumneutral pore-water pH. Continued sulfide oxidation and local depletion of carbonate minerals may eventually result in low pore-water pH. Due to the highly heterogeneous mineralogy, low pore-water pH could have occurred locally in the waste rock. Downward migration of acidic pore water enriched in Fe^{3+} into the tailings could promote microbially mediated sulfide oxidation by Fe^{3+} (Pakostova et al. 2020).

3.5.7 Trace element mobility

The relative mass abundance of trace elements in the unoxidized tailings of NIT follows the general trend Cu>Zn>As>Mn>Co>Pb>Ni>Cr>Cd. In the aqueous state, the mass abundance is generally as follows: Zn>As>Cu>Mn>Pb>Co with spatial variations between locations. Aqueous Ni, Cr and Cd concentrations are in μg L^{-1} and several orders of magnitude lower than the other elements.

Sphalerite oxidation was the primary source of dissolved Zn. Zinc was mobile and conservative in the pore water, which was evident from its ubiquitous presence in the pore water and groundwater. Its mobility, especially its presence at greater depths, is partially attributed to the higher reactivity of sphalerite. Co-precipitation with crystalline (oxy)hydroxides was the dominant solid-phase control on Zn. Sequestered Zn was relatively stable under various geochemical conditions, except under strongly reducing conditions.

Copper mainly originated from chalcopyrite oxidation. Sorption and co-precipitation with crystalline Fe (oxy)hydroxides were the dominant processes controlling pore water Cu concentrations in the oxidized zone. At and below the interface between the oxidized zone and the reduced zone, covellite precipitation also controlled pore-water Cu concentrations. Attenuated Cu in Fe (oxy)hydroxides can re-mobilize under acidic and strongly reducing conditions.

Arsenic was derived from the oxidation of arsenopyrite and As-bearing pyrite. Arsenic was mainly sequestered through sorption and co-precipitation with Fe oxyhydroxides and hydroxysulfates. Sequestered As can be re-mobilized under a variety of chemical conditions. Most As sequestered in the oxidized zone and alteration rims below the oxidized zone occurred as As(V). Scorodite may also be a minor sink for As(V) in the oxidized zone. However, a small amount of As(III) persisted in the oxidized zone. Because As(III) is more toxic and mobile than As(V), its persistence and ease of release can be of concern in the long-term evolution of the tailings.

Manganese likely originated from carbonate and/or aluminosilicate dissolution. Like Zn, it was relatively conservative and was present in elevated concentrations in the groundwater plume in the sand aquifer. A limited amount of Mn was sequestered in crystalline oxyhydroxides. Cobalt and Pb were present as trace components in the principal sulfides.

Lead was attenuated by sorption/co-precipitation with crystalline (oxy)hydroxides, especially at the oxidized zone. In contrast, SEM/EDX analysis reveals low to little presence of Co in pyrrhotite or sphalerite deep in the tailings (Appendix D), which partially explains its relatively low abundance in the aqueous state relative to Pb.

Results from selective chemical extractions, SEM/EDX, and synchrotron suggest that crystalline Fe(III) oxyhydroxides, including goethite, lepidocrocite, and Fe_2O_3, acted as important sources and sinks for trace metal(loid)s, in both the oxidized zone and deeper in the tailings. Where the cover functions to limit sulfide oxidation rates, higher pore-water pH promotes the desorption of As. When defects in the cover enable localized sulfide oxidation in the tailings, it results in acidic conditions and dissolution of Fe(III) (oxy)hydroxides, re-mobilizing trace metal(loid)s. If strongly reducing conditions are present under the cover, reductive dissolution of crystalline (oxy)hydroxides may occur and release trace elements. Although there was evidence of lower Eh over time at KK3, strongly reducing conditions in the tailings were not observed during any sampling event.

At the base of the tailings, sulfate reduction was observed at KK3 and is inferred to occur through reactions of the pore water SO_4 with naturally occurring peat, which controlled the concentrations of trace elements through the precipitation of metal sulfides at a local scale. On a larger scale, organic carbon availability at the site was sporadic and insufficient to remove significant quantities of trace elements. Elevated metal(loid) concentrations persisted in the pore water and the groundwater plume in the underlying aquifer more than a decade after cover placement. For elements that cannot form low-solubility metal sulfides, such as Mn, sulfate reduction would be ineffective in controlling mobility; these elements may continue to be of concern in the long term.

3.6 Conclusions

Four decades of subaerial oxidation depleted sulfides to a depth of 0.1-0.25 m at NIT of Kam Kotia and resulted in elevated aqueous concentrations of SO_4, Fe, Al, and trace elements Zn, As, Cu, Pb, Mn, and Co in the pore water and groundwater. More than a decade after the placement of a composite cover for remediation, depleted O_2, circumneutral pH, and declining concentrations of metal(loid)s were identified at KK3,

indicating that the cover slowed sulfide oxidation rates at this location. δ^{13}C-DIC and δ^{34}S-SO_4 isotope ratios indicate sulfate reduction facilitated by organic-rich peat under the tailings, which locally attenuated SO_4 and elements.

In contrast, near-atmospheric O_2 concentrations, low pH, and elevated metal(loid) concentrations were present at KK4, indicating potential cover defects that enabled continued sulfide oxidation. Calcite and dolomite were nearly depleted at KK4 whereas siderite dissolution contributed to acid neutralization. Dissolution of Al hydroxides and aluminosilicates released Al into the pore water. Low pore-water pH immediately below the hardpan likely resulted in more rapid sulfide oxidation rates and inhibited the precipitation of Fe(III) (oxy)hydroxides. Fe(III) (oxy)hydroxide dissolution occurred under low pH, which further released the associated trace elements. The rate of sulfide oxidation decreased rapidly with depth and sulfide oxidation was limited beneath approximately 0.6 m from the top of the tailings.

Zinc and Mn were conservative and mobile in the pore water, with minor sequestration in crystalline oxyhydroxides. Copper was attenuated by covellite formation and by sorption and co-precipitation with Fe (oxy)hydroxides below the zone of active oxidation. Arsenic was sequestered by Fe (oxy)hydroxides but can be easily re-mobilized under a variety of geochemical conditions. Arsenate was dominant in the oxidized zone but arsenite also persisted. Lead was sequestered by crystalline (oxy)hydroxides in the oxidized zone, whereas Cobalt had minimal secondary phase sequestration. Crystalline oxyhydroxides played an important role in sequestering trace elements, which can be released through desorption, acidic dissolution, and potentially reductive dissolution. Without sufficient organic carbon and reducing conditions, sulfate reduction was unlikely to occur on a large scale.

Although the composite cover impedes infiltration and gas transport, despite potential local defects (Chapter 2), the pore-water geochemistry in legacy tailings is complex due to the potential for remobilization of previously sequestered elements, continued sulfide oxidation, and an absence of large-scale sulfate reduction. In particular, SO_4, Zn, Mn, and As are likely to remain water quality concerns.

Chapter 4
Reactive transport modelling of tailings hydrogeochemistry under a composite cover

4.1 Summary

Reactive transport simulations corresponding to a detailed sampling location at a covered legacy tailings impoundment in northern Ontario, Canada, were conducted to quantitatively assess the predominant hydrogeochemical reactions. The simulations span the period from the end of tailings deposition (circa 1970) to 2020, 12 years after remediation by a five-layer composite cover. The conceptual model of uncovered tailings weathering and geochemistry of the covered tailings system was implemented in 1-D using the multi-component reactive transport code MIN3P. Transient monthly infiltration, post-cover boundary condition changes, and a dynamic temperature regime were incorporated. The shrinking core model, including parallel $O_{2(aq)}$ and Fe^{3+} oxidation pathways for the waste rock in the cover and the underlying tailings, was incorporated in simulations of oxidation of As-bearing pyrite, chalcopyrite, and sphalerite. Primary host minerals calcite, siderite, albite, anorthite, and muscovite promoted acid-neutralization reactions. Precipitation/dissolution of secondary phases including ferrihydrite, jarosite, gypsum, gibbsite, and amorphous silica and sorption/desorption of cations and arsenite were included in the conceptual model and simulations. The overall agreement between key simulated and field-measured aqueous geochemical parameters suggests that the conceptual model captured the primary hydrogeochemical processes in the tailings and the cover. A lack of reliable data on initial tailings mineralogy and hydrogeochemistry prior to cover placement increased model uncertainties. Simulated reaction rates indicate that where intact, the cover decreased sulfide oxidation rates by both $O_{2(aq)}$ and Fe^{3+} and improved pore-water quality over time. Elevated concentrations of SO_4, Zn and As were likely to persist in the tailings regardless of cover performance, whereas concentrations of Cu and Al were the most sensitive to cover effectiveness.

4.2 Introduction

Quantitative forecasts of the duration and magnitude of acid mine drainage (AMD) from mine wastes, such as tailings and waste rock, can provide critical information for planning remediation strategies and mine closure. Accurate forecasting has been a challenge for stakeholders because it requires advanced numerical techniques and a robust representation of site-specific hydrogeochemistry (Wilson et al. 2018a, 2018b).

Acid mine drainage originates from the oxidation of sulfide minerals, such as pyrite [FeS_2], pyrrhotite [$Fe_{1-x}S$], chalcopyrite [CuFeS], sphalerite [ZnS], and arsenopyrite [FeAsS], in mine waste, following exposure to water and O_2, which can subsequently release acidity, sulfate [SO_4], and toxic elements into the environment. Both $O_{2(aq)}$ and Fe^{3+} can act as oxidants. There are two main microbially mediated oxidation pathways, polysulfide and thiosulfate, which involve intermediate S species that subsequently oxidize to the end product SO_4^{2-} (Rohwerder et al. 2003, Blowes et al. 2014). Sulfide oxidation is biologically mediated by sulfide- and iron-oxidizing bacteria (Johnson and Hallberg 2008, Blowes et al. 2014). Dissolution of gangue minerals including Ca and Mg carbonates and aluminosilicates in the mine waste as well as the surrounding soil and aquifer materials contribute to the neutralization of the acidity generated by sulfide oxidation. Precipitation and dissolution of secondary minerals such as Fe(III) (oxy)hydroxides also influence the pH and elemental concentrations. In addition, secondary minerals can sequester trace elements through co-precipitation and sorption reactions. Other processes such as evaporative enrichment of elements, sulfate reduction, and reductive dissolution of Fe(III) (oxy)hydroxides, may occur under certain conditions. Reactive transport modelling can provide a quantitative framework for the interpretation of the complex suite of hydrogeochemical processes occurring in mine wastes and in forecasting drainage quality.

Covers (mono-layer or composite) are a widely implemented option for mine waste remediation. Covers can be designed to reduce O_2 and water availability for AMD generation. However, the design and evaluation of cover efficiency for AMD remediation are confounded by a series of interacting factors such as climate, hydrogeological processes, mineralogical characteristics, and unidentified geochemical reactions. Reactive transport

modelling can serve as an effective tool to assess the impact of these factors and to evaluate the long-term efficiency of cover systems.

Simulation of contaminant transport can be implemented in several ways. Simplified solute transport models, which consider advection and diffusion-dispersion without regard to chemical reactions, are not suitable for complex mine waste geochemical systems. Equilibrium models assume all reactions achieve equilibrium; however, extensive studies on sulfide oxidation suggest that it is strongly influenced by the diffusion of O_2 to the sulfide grains and through secondary-mineral coatings encapsulating the primary sulfide grains (Blowes et al. 2014). Kinetic-based models, which consider reaction rates, provide improved geochemical simulations of mine drainage systems (Mayer et al. 2002). Moreover, reactive transport codes that consider the solid, aqueous, and gaseous phases enable a more robust representation of the hydrogeochemical system (Steefel et al. 2015).

MIN3P is a multi-component reactive transport code that uses the finite volume method for spatial discretization and the global implicit solution method to solve coupled variably saturated flow and reactive transport equations (Mayer et al. 2002). It includes both kinetic and equilibrium formulations of geochemical reactions involving gas transport, aqueous complexation, redox reactions, and mineral dissolution/precipitation (Mayer et al. 2002).

MIN3P has been applied to quantitatively investigate hydrogeochemical processes in mine tailings and waste rock piles. Mayer et al. (2002) demonstrated the effectiveness of MIN3P in modelling AMD generation and attenuation via a 1-D reactive transport simulation of the Nickel Rim tailings site, which yielded insights into processes controlling the aqueous concentrations of key constituents and mineral dissolution/precipitation. Brookfield et al. (2006) conducted 2-D reactive transport through Copper Cliff tailings impoundment to enhance the understanding of hydrogeochemical processes occurring at the tailings impoundment, such as the importance of water-table fluctuations and the complexity of the iron system. Wilson et al. (2018a) presented a model for sulfide weathering in low S waste rock humidity cells, whereas Wilson et al. (2018b) used a mechanistic scale-up of the humidity cell model to simulate medium-scale field active zone lysimeter experiments.

MIN3P has also been used to predict and evaluate the effectiveness of cover systems in laboratory and field test cells. Molson et al. (2008) simulated four field cells of cover systems

with capillary barrier effects over unoxidized tailings and demonstrated the effectiveness of covers in limiting O_2 front migration and sulfide oxidation. Model sensitivity analysis indicated that covered tailings simulations were not sensitive to effective diffusion coefficients but sensitive to cover water retention parameters. Pabst et al. (2017) used MIN3P to simulate laboratory columns of mono-layer covers placed on pre-oxidized tailings with extension to field applications; the authors found mono-layer covers ineffective in preventing AMD and sensitive to water-table position. Pabst et al. (2018) compared the performance of covers with one, two, and three layers on pre-oxidized tailings and found tri-layer covers with capillary barrier effects to be much more protective than other cover configurations in reducing O_2 flux and AMD production. The authors also found that AMD generation continued for several years in pre-oxidized tailings even with significant reductions in O_2 flux; as well, improvement in effluent quality could take several years to occur.

The abandoned Kam Kotia mine (48.6°N, 81.6°W) is a former copper and zinc mine located in northern Ontario near Timmins (Figure 4-1a). The North Impounded Tailings (NIT) area, one of the principal tailings storage facilities at the site, received tailings deposition between 1968 and 1972. In 1972, the mine was abandoned without rehabilitation and severe AMD contamination occurred for over three decades. In 2008, a composite cover with five layers was placed on the NIT tailings. From the ground surface downward, the cover consists of layers of sand and clay, a geosynthetic clay liner (GCL), a lower sand layer, and a layer of waste rock below the lower sand layer to provide a capillary barrier (Figure 4-1c). The composite cover was expected to reduce AMD production in the NIT tailings by limiting O_2 and water ingress.

One objective of the reactive transport simulations in this study was to quantitatively assess relevant hydrogeochemical processes at NIT with a focus on long-term geochemical processes of sulfide oxidation, acid neutralization, and contaminant mobility. The other objective of the study was to evaluate the effectiveness of the composite cover.

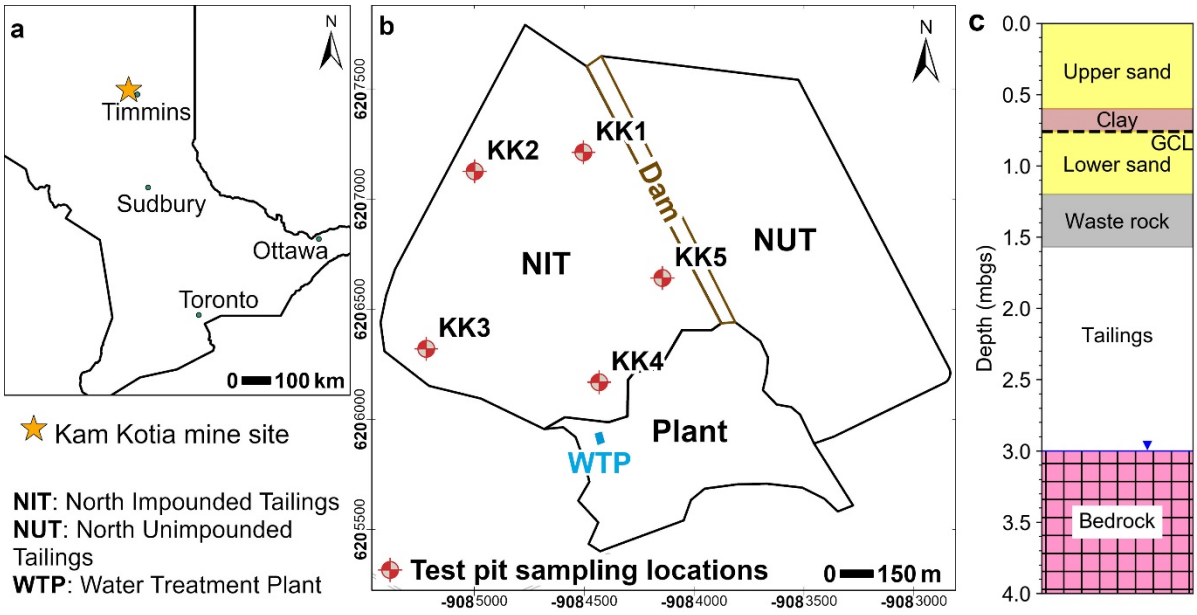

Figure 4-1. (a) Location of Kam Kotia mine within Ontario, Canada. (b) Conceptual diagram of the mine site including NIT and five test pits excavated in 2017 at NIT. (c) Cross-sectional lithology of test pit KK4 at NIT with the five-layer composite cover. The blue inverted triangle represents the average water table depth.

4.3 Methods

4.3.1 Conceptual model

The hydrogeochemical evolution at KK4, one of the test pit locations, was represented in a 1-D vertical system. Tailings and the cover were simulated separately and connected by boundary conditions. Reactive transport simulations of the tailings encompass approximately 50 years, from deposition (circa 1970) to being under a composite cover between 2008 and early 2020 (Figure 4-2). Before remediation, the tailings deposited in the impoundment were exposed to subaerial weathering with rainwater infiltration, which led to extensive AMD generation. After approximately 38 years of weathering, the composite cover was added. A decrease in the infiltration to the tailings was expected to occur after cover placement, which was confirmed by hydrogeological characterization and variably saturated flow simulations (Chapter 2). As well, the composition of the infiltrating water to the tailings was altered from rainwater to the composition observed at the bottom of the waste rock layer by reactions with the cover components. Thus, the placement of the cover was

conceptualized as a change in both the flow and the reactive transport boundary conditions at the inflow boundary (Figure 4-3).

The cover was expected to decrease groundwater mounding at NIT and reduce the hydraulic heads (Wardrop Engineering Inc. 2005). A decline in the water table at the outflow boundary after cover placement was anticipated. Seasonal groundwater fluctuations caused by spring snowmelt were salient features of the local hydrogeology, which were not included in the conceptual model due to the additional complexity.

Mineralogical studies of tailings at depth >0.8 m from the top of the tailings, which were minimally impacted by sulfide oxidation, indicate that the main sulfide minerals in the tailings are pyrite, chalcopyrite, and sphalerite, with small amounts of pyrrhotite and arsenopyrite. Initial mineralogy was assumed to be homogeneous throughout the tailings, such that all primary minerals were evenly distributed. Pyrite, chalcopyrite, and sphalerite were included as the reactive sulfides. Pyrrhotite was not included due to its low abundance and the similarity in oxidation products to pyrite. To simplify the model, arsenopyrite was not simulated separately; instead, it was assumed that As was incorporated into the pyrite structure. The molar ratio between As and Fe calculated from whole rock XRF analysis yielded a modified chemical expression $FeAs_{0.01}S_{1.99}$ for pyrite.

Oxidation of sulfide minerals was conceptualized as transport-controlled by the diffusion of oxidants, including both $O_{2(aq)}$ and Fe^{3+}, and represented by the shrinking core model (Davis and Ritchie 1986, Wunderly et al. 1996). Parallel pathways of oxidation by $O_{2(aq)}$ and Fe^{3+} act separately on the same mineral. For each sulfide, two rate expressions were written according to the reaction stoichiometry in Table 4-1. For example, the rate expression for pyrite oxidation by $O_{2(aq)}$ is (after Mayer et al., 2002):

$$R_{Py-O_{2(aq)}} = -10^3 S_{FeS_2} D_{O_2} \left[\frac{r_p}{(r_p - r_r) r_r}\right]\left[\frac{[O_{2(aq)}]}{v_{O_2}}\right] \qquad \text{eq. 4-1}$$

where $R_{Py\text{-}O2(aq)}$ represents the rate of pyrite oxidation by $O_{2(aq)}$ in mol L^{-1} d^{-1}, S is the scaling factor (m^2_{min} L^{-1}_{bulk}), r_p is the particle radius (m), r_r is the unreacted particle radius (m), vO_2 is the stoichiometric coefficient for $O_{2(aq)}$, and D_{O2} is the effective diffusion coefficient (m^2 s^{-1}) for $O_{2(aq)}$ diffusion through the oxidation rim to the unreacted surface.

Similarly, the rate expression for oxidation of pyrite by Fe^{3+} can be written as

$$R_{Py-Fe^{3+}} = -10^3 S_{FeS_2} D_{Fe^{3+}} \left[\frac{r_p}{(r_p - r_r)r_r}\right]\left[\frac{[Fe^{3+}]}{v_{Fe^{3+}}}\right] \quad \text{eq. 4-2}$$

where $R_{Py\text{-}Fe3+}$ represents the rate of pyrite oxidation in mol L^{-1} d^{-1}, v_{Fe3+} is the stoichiometric coefficient for Fe^{3+}, and D_{Fe3+} is the effective diffusion coefficient (m^2 s^{-1}) for Fe^{3+} diffusion through the oxidation rim to the unreacted surface. Similar shrinking core rate expressions were written for sphalerite and chalcopyrite for oxidation by both $O_{2(aq)}$ and Fe^{3+}. The reactions are summarized in Table 4-1.

Gangue minerals in the tailings identified from XRD analysis include calcite, siderite, albite, anorthite, muscovite, chlorite, K-feldspar, and quartz. Quartz was not included due to a low rate of dissolution. Chlorite and K-feldspar were not included due to their limited acid-neutralization capacity and to simplify the model. Reaction stoichiometries for the dissolution of primary minerals were summarized in Table 4-1. Calcite dissolution was conceptualized as reversible, and the reaction rate was pH-dependent and controlled by the mineral surface area (S). The dissolution rates of albite, anorthite, and muscovite were conceptualized as pH-dependent and irreversible, which were controlled by mineral surface area. The dissolution of dolomite and siderite was reversible and controlled by the reaction rate constant (k_{eff}). The rate expressions are summarized in Table 4-2.

Secondary minerals selected in the model were based on mineralogical analysis and SI calculations. Gypsum, Fe(III) (oxy)hydroxides (represented by ferrihydrite) and Fe(III) hydroxysulfates (jarosite and natrojarosite) are common secondary minerals in mine wastes (Blowes et al. 2014) and identified by optical microscopy and X-ray diffraction. Although discrete Al-bearing secondary phases were not identified during the mineralogy analysis, gibbsite was included based on SI calculations. Amorphous silica, a common reaction product in AMD systems (Blowes et al. 2014), was included as a secondary mineral and prevented the buildup of Si in the aqueous phase. Precipitation of secondary minerals was assumed to be reversible and controlled by the corresponding rate constants. Rate expressions for secondary-mineral precipitation are summarized in Table 4-2.

Primary and secondary aqueous species were selected based on measured aqueous geochemistry. Primary aqueous species include $O_{2(aq)}$, Fe^{2+}, Fe^{3+}, SO_4^{2-}, Cu^{2+}, Zn^{2+}, H_3AsO_3,

Al^{3+}, Mg^{2+}, Ca^{2+}, K^{+}, Na^{+}, CO_3^{2-}, H^{+}, HS^{-}, and H_4SiO_4. Secondary aqueous species (n=76) were included to account for relevant equilibrium aqueous complexation reactions. Equilibrium redox reactions, gas partitioning and sorption reactions are summarized in Table 4-3. SO_4^{2-}/HS^{-} and Fe^{2+}/Fe^{3+} were included as redox couples. O_2 and CO_2 were included as gas phases. Sorption of Cu, Zn, and As(III) as arsenite (H_3AsO_3) onto hydrous ferric oxides (HFO), represented as ≡FeOH, was included using a two-layer surface complexation model (Dzombak and Morel 1991). Literature-derived sorption parameters for HFO were prescribed, including a constant surface area of 600 m^2 $(g\ solid)^{-1}$ and sorption site densities of 0.056 sites nm^{-1} for strong sites and 2.3 sites nm^{-1} for weak sites (Dzombak and Morel 1991). The mass of HFO was fixed at 2 g solid $(LH_2O)^{-1}$ to facilitate competitive sorption between the cation and oxyanion species. Surface complexation constants for Cu and Zn were derived from Dzombak and Morel (1991) whereas those for arsenite were from Dixit and Hering (2003).

Reactive transport simulations for the composite cover span from its installation in 2008 to early 2020. The upper sand, clay and lower sand layers were simulated separately from the waste rock layer. The GCL was excluded, since it was too thin (<1 cm), without well-defined mineralogy, and caused convergence issues for the reactive transport simulations. Similar primary and secondary minerals were included for each layer in the cover simulations but with different input parameters, i.e., initial volume fractions and reaction rate constants or surface areas. Sulfide oxidation reactions in the waste rock were conceptualized in the same manner as those in the tailings. No sulfide minerals were included in the sand and clay layers, which is consistent with the XRD spectra for the cover layers.

A seasonally and spatially variable temperature regime was incorporated into the simulations of the tailings and cover. Temperatures from continuously measured *in situ* instrumentation at various depths provided monthly temporal and spatial temperature dynamics. The seasonal temperature cycle was assumed to be inter-annually consistent. A change in the temperature cycle was prescribed after cover placement since placement of the cover would reduce the magnitude of seasonal temperature fluctuations in the tailings, as revealed by *in situ* instrument measurements at different depths (Chapter 2). Freeze-thaw cycle and associated changes in hydraulic conductivity and reaction rates were not incorporated into the model due to a lack of relevant field and laboratory experimental data.

Temperature changes affect equilibrium and reversible kinetic reactions with defined enthalpy changes, as well as irreversible kinetic reactions with defined activation energies (E_a). For sulfide oxidation reactions simulated with the shrinking core model, activation energies or enthalpies can be defined from humidity cell experiments conducted under different temperatures (Wilson et al. 2018a, 2018b). However, similar laboratory experiments were not conducted, so temperature dynamics were not accounted for.

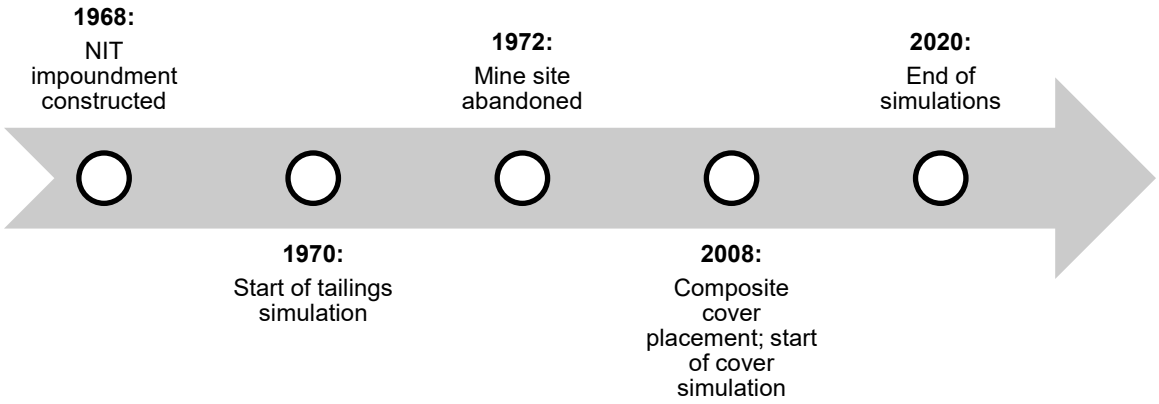

Figure 4-2. Timeline of reactive transport simulations of the North Impounded Tailings (NIT) of the abandoned Kam Kotia mine.

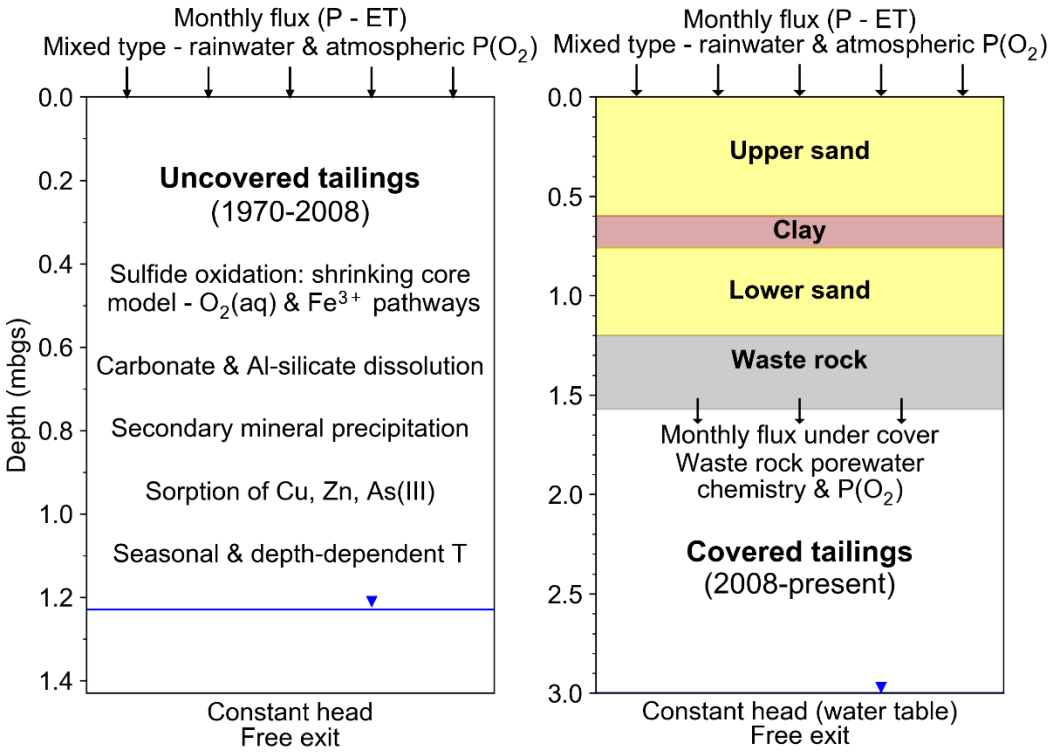

Figure 4-3. Conceptual model of tailings reactive transport processes before cover placement (left) and after cover placement (right).

Table 4-1. Reaction stoichiometry and solubility product (K_{sp}) at 25 °C for mineral dissolution and precipitation.

Mineral	Reactions	log K_{sp}
	Primary minerals	
As-bearing pyrite	$FeAs_{0.01}S_{1.99} + 1.005H_2O + 3.4925O_2 \rightarrow Fe^{2+} + 0.01H_3AsO_3 + 1.99{SO_4}^{2-} + 1.98H^+$	-*
	$FeAs_{0.01}S_{1.99} + 13.97Fe^{3+} + 7.99H_2O \rightarrow 14.97Fe^{2+} + 0.01H_3AsO_3 + 1.99{SO_4}^{2-} + 15.95H^+$	-*
Chalcopyrite	$CuFeS_2 + 4O_{2(aq)} \rightarrow Cu^{2+} + Fe^{2+} + 2{SO_4}^{2-}$	-*
	$CuFeS_2 + 16Fe^{3+} + 8H_2O \rightarrow Cu^{2+} + 17Fe^{2+} + 2{SO_4}^{2-} + 16H^+$	-*
Sphalerite	$ZnS + 2O_{2(aq)} \rightarrow Zn^{2+} + {SO_4}^{2-}$	-*
	$ZnS + 8Fe^{3+} + 4H_2O \rightarrow Zn^{2+} + 8Fe^{2+} + {SO_4}^{2-} + 8H^+$	-*

Calcite	$CaCO_3 \leftrightarrow Ca^{2+} + {CO_3}^{2-}$	-8.475
Dolomite	$MgCa(CO_3)_2 \leftrightarrow Mg^{2+} + Ca^{2+} + 2{CO_3}^{2-}$	-17.09
Siderite	$FeCO_3 \leftrightarrow Fe^{2+} + {CO_3}^{2-}$	-10.89
Muscovite	$KAl_2(AlSi_3O_{10})(OH)_2 + 10H^+ \rightarrow K^+ + 3Al^{3+} + 3H_4SiO_4$	-**
Albite	$NaAlSi_3O_8 + 4H_2O + 4H^+ \rightarrow Na^+ + Al^{3+} + 3H_4SiO_4$	-**
Anorthite	$CaAl_2Si_2O_8 + 8H^+ \rightarrow Ca^{2+} + 2Al^{3+} + 2H_4SiO_4$	-**
	Secondary minerals	
Gibbsite	$Al(OH)_3 + 3H^+ \leftrightarrow Al^{3+} + 3H_2O$	8.11
Ferrihydrite	$Fe(OH)_{3(am)} + 3H^+ \leftrightarrow Fe^{3+} + 3H_2O$	4.89
Jarosite	$KFe_3(SO_4)_2(OH)_6 + 6H^+ \leftrightarrow K^+ + 3Fe^{3+} + 2{SO_4}^{2-} + 6H_2O$	-9.21
Natrojarosite	$NaFe_3(SO_4)_2(OH)_6 + 6H^+ \leftrightarrow Na^+ + 3Fe^{3+} + 2{SO_4}^{2-} + 6H_2O$	-5.28
Gypsum	$CaSO_4 \cdot 2H_2O \leftrightarrow Ca^{2+} + {SO_4}^{2-} + 2H_2O$	-4.6
Amorphous silica	$SiO_{2(am)} + 2H_2O \leftrightarrow H_4SiO_4$	-2.71

Note: *shrinking core model

**irreversible dissolution

Table 4-2. Rate expressions for dissolution/precipitation of minerals. *R* represents the reaction rate, *IAP* represents the ion activity product, K_m represents the solubility product (Table 4-1), k_m^{eff} represents the effective rate constant (mol L^{-1} d^{-1}), and S_m represents the mineral reactive surface area (m^2_{min} L^{-1}_{bulk}).

Mineral	Rate expression
Calcite	$R = -S_{CaCO_3}\left[10^{-0.05}[H^+] + 10^{-6.19} + 10^{-3.3}[H_2CO_3]\right]\left[1 - \frac{IAP}{K_{CaCO_3}}\right]$
Dolomite	$R = -k^{eff}_{MgCa(CO_3)_2}\left[1 - \frac{IAP}{K_{MgCa(CO_3)_2}}\right]$
Siderite	$R = -k^{eff}_{FeCO_3}\left[1 - \frac{IAP}{K_{FeCO_3}}\right]$
Muscovite	$R = -S_{KAl_2(AlSi_3O_{10})(OH)_2}[k_1[H^+]^{0.08} + k_2[H^+]^{-0.1}]$
Albite	$R = -S_{NaAlSi_3O_8}[k_1^{eff}[H^+]^{0.49} + k_2^{eff}[H^+]^{-0.3}]$
Anorthite	$R = -S_{CaAl_2Si_2O_8}[k^{eff}_{CaAl_2Si_2O_8}[H^+]^{1.12}]$

Gibbsite	$R = -k^{eff}_{Al(OH)_3}\left[1 - \frac{IAP}{K_{Al(OH)_3}}\right]$
Ferrihydrite	$R = k^{eff}_{Fe(OH)_3}\left[1 - \frac{IAP}{K_{Fe(OH)_3}}\right]$
Jarosite	$R = k^{eff}_{KFe_3(SO_4)_2(OH)_6}\left[1 - \frac{IAP}{K_{KFe_3(SO_4)_2(OH)_6}}\right]$
Gypsum	$R = k^{eff}_{CaSO_4 \cdot 2H_2O}\left[1 - \frac{IAP}{K_{CaSO_4 \cdot 2H_2O}}\right]$
Amorphous silica	$R = k^{eff}_{SiO_{2(am)}}\left[1 - \frac{IAP}{K_{SiO_{2(am)}}}\right]$

Table 4-3. Equilibrium reactions and corresponding equilibrium constant (K) at 25 °C.

Redox couples	Reaction	log K
Fe^{2+}/Fe^{3+}	$Fe^{2+} + \frac{1}{4}O_{2(aq)} + H^+ \leftrightarrow Fe^{3+} + \frac{1}{2}H_2O$	8.5
SO_4^{2-}/HS^-	$HS^- + 2O_{2(aq)} \leftrightarrow {SO_4}^{2-} + H^+$	138.5
Gas partitioning	**Reaction**	**log K**
$O_{2(g)}/O_{2(aq)}$	$O_{2(g)} \leftrightarrow O_{2(aq)}$	-2.9
$CO_{2(g)}/CO_{2(aq)}$	$CO_{2(g)} \leftrightarrow CO_{2(aq)}$	-18.1
Sorption	**Reaction**	**log K**
≡$FeOZn^+$	$\equiv FeOH + Zn^{2+} \leftrightarrow \equiv FeOZn^+ + H^+$	0.99 (strong)*, -1.99 (weak)*
≡$FeOCu^+$	$\equiv FeOH + Cu^{2+} \leftrightarrow \equiv FeOCu^+ + H^+$	2.89 (strong)*, 0.6 (weak)*
≡FeH_2AsO_3	$\equiv FeOH + H_3AsO_3 \leftrightarrow \equiv FeH_2AsO_3 + H_2O$	5.19 (strong)**, 4.02 (weak)**

*data from Dzombak and Morel (1991)

**data from Dixit and Hering (2003)

4.3.2 Model parameters

4.3.2.1 Tailings simulations

The model domain for tailings simulation was constructed as a vertical 1-D column of 1.42 m depth discretized as 143 control volumes to simulate the tailings at one sampling location, KK4. The total duration of the simulations was 18,300 days, which was consistent with the elapsed time between the end of tailings deposition (circa 1970) and field sampling events after cover placement. A minimum timestep of 1×10^{-13} days and a maximum timestep of 5 days were used to promote model convergence, reduce numerical errors, and optimize model runtime.

For flow boundaries, the upper boundary was prescribed using an infiltration flux (second type). Net monthly infiltration fluxes accounting for precipitation, evapotranspiration, and snow cover were calculated and input into MIN3P. Meteorological data throughout the simulation period (1970-2020), including precipitation, temperature, wind speed, and relative humidity, downloaded from two weather stations approximately 17 km east of the site (Environment and Climate Change Canada 2022), were used to facilitate evapotranspiration calculations using FAO-56 Penman-Monteith (Allen et al. 1998) with modification for winter conditions (Appendix A). To account for spring snowmelt, raw calculated infiltration was modified via Hydrus 1-D (Šimůnek et al. 2013) simulations with heat transport and snow hydrology for uncovered tailings from 1970 to 2007. For covered tailings from 2008 to 2020, influxes were prescribed as the simulated outflow from a cover-only Hydrus 1-D simulation with the same atmospheric inflow boundary conditions. Figure 4-4 shows the transient fluxes at the inflow boundary as well as temperature at the top of the tailings prescribed in the model.

A constant head (first type) boundary condition was applied at the lower boundary. Groundwater monitoring before cover placement was sporadic. In addition, temporal changes in groundwater level before and after cover placement were unavailable. Due to the lack of data, the water-table position in the uncovered tailings was calibrated by the model; a water table situated at 0.2 m below ground surface (mbgs) was adopted due to good agreement between the simulated pore-water chemistry and field measurements. The water-table position after cover placement was adopted from Hydrus 1-D simulations (i.e., at

the bottom of the tailings). As well, hydraulic parameters and material properties for each cover layer and the tailings were assumed to be homogeneous and adopted from previously calibrated Hydrus 1-D simulations (Table 4-4).

For most primary minerals, XRD mineral weight percent (wt%) of tailings at depth were adopted, except for sphalerite and chalcopyrite, which were below the detection limit of XRD. Sphalerite and chalcopyrite wt% were calculated from XRF total Zn and Cu of tailings at depth, assuming that these sulfide phases accounted for all solid-phase Zn and Cu. Mineral wt% was then converted to initial volume fraction (φ_i) ($m^3_{mineral}$ m^{-3}_{bulk}, or dimensionless) using mineral density (ρ_{min}) from MIN3P or WATEQ4F mineral database and sample bulk density (ρ_b) measurements:

$$\varphi_i = \frac{wt\%}{100\rho_{min}}\rho_b \qquad \text{eq. 4-3}$$

For all secondary minerals, an initial φ_i of $1x10^{-10}$ was prescribed. For sulfide minerals simulated using the shrinking core model, r_r (unreacted particle radius) was the average particle radius (5.63×10^{-5} m) derived from particle-size analysis by sieve. r_p (5.6×10^{-5} m) was slightly smaller than r_r as required by the shrinking core model.

For reactive transport boundaries, the upper boundary was prescribed as a specified flux of infiltrating water and free diffusion of gaseous and dissolved phases (mixed type boundary). The chemical composition of rainwater was adapted from Mayer et al. (2002) and Molson et al. (2008) and summarized in Table 4-7. A free exit boundary condition was applied at the lower boundary. To account for the placement of the composite cover, a change in the reactive transport inflow boundary condition was prescribed at timestep 14,000 days (corresponding to 2008), with the inflow switching from rainwater to the average pore-water composition in the waste rock layer (Table 4-7). Oxygen partial pressure (P_{O2}) was assigned as 0.01%, which approximated a successful composite cover that acted as a barrier to O_2 transport. Initial concentrations of aqueous species were adopted from Mayer et al. (2002) and Molson et al. (2008) and summarized in Table 4-7.

Simulations of aqueous geochemistry were compared to post-cover aqueous geochemistry data from field sampling events from 2017 to 2021 for calibration. Simulated pH and aqueous concentrations of Fe and SO_4 were also compared to published (Fortin et

al. 1996) studies on Kam Kotia tailings as a pre-cover order-of-magnitude calibration reference.

For each primary sulfide mineral, effective diffusion coefficients and scaling factors for $O_{2(aq)}$ and Fe^{3+} oxidation (four parameters) were calibrated. Since more effective diffusion coefficients than scaling factors were reported in the literature, initial calibration was conducted to obtain order-of-magnitude estimates of the effective diffusion coefficients comparable to literature values (Mayer et al. 2002, Wilson et al. 2018a, 2018b) with fixed scaling factors of arbitrary values. Scaling factors were subsequently calibrated to fine-tune the simulations with fixed effective diffusion coefficients. For non-sulfide minerals, effective rate constants for reversible mineral dissolution/precipitation reactions, and reactive surface areas for irreversible mineral dissolution were calibrated. Parameters were adjusted until reasonable agreement between the simulated and measured aqueous geochemistry for all relevant parameters was obtained.

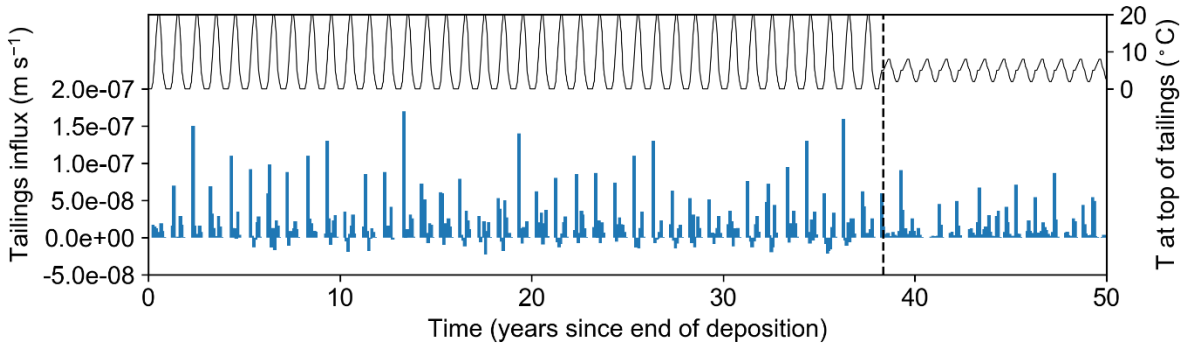

Figure 4-4. Monthly infiltration and temperature from 1970 (year 0) to early 2020 (year 50) prescribed at the upper boundary of the tailings simulations. The vertical dashed line indicates the time of cover placement.

Table 4-4. Hydraulic parameters used in MIN3P simulations.

Material	θ_r ($m^3\ m^{-3}$)	θ_s ($m^3\ m^{-3}$)	α (m^{-1})	n (-)	K_{sat} ($m\ s^{-1}$)	AEV (m)
Upper sand	0.06	0.39	0.5	7.0	1.00×10^{-4}	0
Clay	0.15	0.40	0.04	1.3	1.88×10^{-7}	5
Lower sand	0.12	0.33	2.0	2.2	1.00×10^{-4}	0
Waste rock	0.13	0.39	3.0	3.6	5.00×10^{-5}	0

Tailings	0.05	0.48	0.7	1.6	1.00×10^{-6}	0

θ_r: residual volumetric water content

θ_s: saturated volumetric water content (=ϕ)

α, n: van Genuchten (1980) parameters for water retention curves

K_{sat}: saturated hydraulic conductivity

AEV: air entry pressure

Table 4-5: Initial volume fraction (φ_i) and calibrated input parameters for tailings (diffusion coefficient (D) for sulfide minerals, reaction rate constant (k_{eff}), surface area or scaling factor (S), and activation energy (E_a)).

Mineral	φ_i ($m^3_{min}\ m^{-3}_{bulk}$)	D ($m^2\ s^{-1}$) / k_{eff} (mol $L^{-1}\ d^{-1}$)	S ($m^2_{min}\ L^{-1}_{bulk}$)	E_a (kJ mol^{-1})
As-bearing pyrite	1.1×10^{-1}	$O_{2(aq)}$: 1.0×10^{-13} Fe^{3+}: 2.0×10^{-18}	0.01	- -
Chalcopyrite	8.0×10^{-3}	$O_{2(aq)}$: 1.0×10^{-14} Fe^{3+}: 2.0×10^{-18}	0.02	- -
Sphalerite	1.0×10^{-3}	$O_{2(aq)}$: 1.0×10^{-14} Fe^{3+}: 2.0×10^{-18}	2.5×10^{-3}	- -
Calcite	6.5×10^{-3}	-	2.0×10^{-5}	2
Dolomite	5.0×10^{-5}	1.0×10^{-9}	-	-
Siderite	3.5×10^{-3}	2.0×10^{-10}	-	-
Muscovite	1.0×10^{-4}	-	0.1	5.3
Albite	5.0×10^{-5}	-	0.1	13.9
Anorthite	2.5×10^{-3}	-	0.1	19.3
Gibbsite	-	1×10^{-6}	-	-
Ferrihydrite	-	1×10^{-9}	-	-
Jarosite	-	1×10^{-11}	-	-
Natrojarosite	-	1×10^{-11}	-	-
Gypsum	-	1×10^{-6}	-	-
SiO_2 (am)	-	1×10^{-6}	-	-

4.3.2.2 Cover simulations

Cover layers were simulated separately from tailings to promote model convergence. The duration of cover simulations was 4,383 days to match the period between cover placement in 2008 and early 2020. Spatial discretization was 1 cm, which was consistent with the discretization used in the tailings simulation.

Hydraulic parameters for each of the four cover layers derived from Hydrus 1-D simulations were applied (Table 4-4). Sulfide-free layers of upper sand, clay, and lower sand were included in one simulation and the sulfide-containing waste rock layer was simulated in the other. The two simulations were linked by flow and reactive transport boundary conditions. Monthly fluxes from the outflow boundary of the sand-clay-sand simulation were used to provide monthly inflow boundary conditions for the waste rock simulation. The average aqueous concentrations at the outflow boundary of the sand-clay-sand simulations were assumed as the influx concentrations in the waste rock simulation; because sulfide oxidation was not prescribed in the sand-clay-sand layer, temporal changes in aqueous geochemistry at the outflow were not significant.

For sand and clay, minerals identified in XRD analysis were included in the simulations. The upper sand and the lower sand were assumed to have the same mineralogical composition since they were of the same origin. For the waste rock, whole rock XRF elemental wt% results were converted to mineral wt% assuming that chalcopyrite accounts for all Cu, sphalerite accounts for all Zn, and all remaining S were attributed to pyrite. These calculations were adjusted using SEM/EDX quantitative elemental composition on waste rock thin sections. The same diffusion coefficients for the shrinking core model for the tailings were used for the waste rock since they originated from the same ore body. Scaling factors were adjusted to fit the simulated results to the measured pore-water chemistry. Input parameters for cover mineralogy were summarized in Table 4-6.

Similar to the tailings simulations, the inflow boundary was set as transient monthly specified fluxes from precipitation records and calculated evapotranspiration between 2008 and 2020. The outflow boundary was set as specified hydraulic heads. The upper reactive transport boundary was set as mixed type with rainwater composition, and the lower boundary as free exit boundary.

Table 4-6. Initial volume fraction and calibrated input parameters for cover layers (diffusion coefficient for sulfide minerals, reaction rate constant, and surface area).

Mineral	Sand φ (m^3 mineral m^{-3} bulk)	Clay φ (m^3 mineral m^{-3} bulk)	k_{eff}/S (sand and clay)	Waste rock φ (m^3 mineral m^{-3} bulk)	k_{eff}/S (waste rock)
As-bearing Pyrite	-	-	-	1.5×10^{-2}	0.06
Chalcopyrite	-	-	-	3.0×10^{-3}	1
Sphalerite	-	-	-	2.0×10^{-2}	0.8
Calcite	1.1×10^{-2}	2.0×10^{-2}	4×10^{-4}	5.0×10^{-4}	1×10^{-7}
Dolomite	1.0×10^{-3}	7.0×10^{-4}	1×10^{-9}	1.0×10^{-6}	1×10^{-10}
Siderite	-	-	1×10^{-9}	1.0×10^{-7}	1×10^{-10}
Muscovite	1.2×10^{-3}	5.5×10^{-2}	1.0	1.0×10^{-2}	2.0
Albite	7.5×10^{-2}	3.6×10^{-2}	1.0	2.5×10^{-2}	5.0
Anorthite	1.1×10^{-1}	5.4×10^{-2}	0.5	4.0×10^{-2}	1.0
Gibbsite	-	-	1×10^{-10}	-	1×10^{-8}
Ferrihydrite	2.9×10^{-3}	2.2×10^{-2}	1×10^{-10}	2.0×10^{-2}	1×10^{-9}
Gypsum	3.0×10^{-3}	3.0×10^{-3}	1×10^{-8}	-	1×10^{-8}
SiO_2 (am)	-	-	1×10^{-6}	-	1×10^{-6}

Table 4-7. Initial and inflow boundary water chemistry.

Aqueous species	Initial concentration - tailings (mol L^{-1})	Initial concentration - cover (mol L^{-1})	Inflow concentration (rainwater) (mol L^{-1})	Inflow concentration after cover placement (mol L^{-1})
$O_{2(aq)}$	pe=-2.5	Eh=5	$P(O_2)=0.21$	$P(O_2)=0.0001$
CO_3^{2-}	2.5×10^{-3}	2.5×10^{-3}	-	5×10^{-3}
$CO_{2(aq)}$	-	-	$P(O_2)= 4.12 \times 10^{-4}$ atm	-
pH	7.0	7.0	5.0	6.9
Ca^{2+}	1.7×10^{-2}	1.7×10^{-2}	3.0×10^{-3}	1.3×10^{-2}
Na^{+}	1.0×10^{-10}	1.0×10^{-10}	1.0×10^{-8}	9.0×10^{-4}

K^+	1.0×10^{-7}	1.0×10^{-7}	1.0×10^{-6}	2.0×10^{-4}
Mg^{2+}	1.0×10^{-8}	1.0×10^{-8}	1.0×10^{-8}	1.2×10^{-3}
Al^{3+}	2.6×10^{-8}	2.6×10^{-8}	1.28×10^{-8}	3.0×10^{-7}
SO_4^{2-}	2.0×10^{-2}	2.0×10^{-4}	1.0×10^{-5}	1.2×10^{-2}
Fe^{2+}	1.0×10^{-4}	1.0×10^{-4}	1.29×10^{-11}	5.6×10^{-6}
Fe^{3+}	1.0×10^{-12}	1.0×10^{-12}	5.36×10^{-5}	1.6×10^{-6}
Cu^{2+}	1.0×10^{-10}	1.0×10^{-10}	1.0×10^{-10}	1.6×10^{-6}
Zn^{2+}	1.0×10^{-10}	1.0×10^{-10}	1.0×10^{-10}	4.0×10^{-5}
H_3AsO_3	1.0×10^{-10}	1.0×10^{-10}	1.0×10^{-10}	1.0×10^{-10}
HS^-	3.0×10^{-12}	3.0×10^{-12}	2.6×10^{-139}	2.6×10^{-139}
H_4SiO_4	2.0×10^{-3}	2.0×10^{-3}	2.0×10^{-4}	4.0×10^{-4}

4.4 Results and discussion

4.4.1 Model performance

Figure 4-5 compares the simulated profiles for tailings pore-water chemistry before cover placement with available field results presented in Fortin et al. (1996). The simulated pH values roughly aligned with the range described by Fortin et al. (1996). The small-scale variations in field-measured pH were likely due to heterogeneity in tailings material and geochemistry, which were not included in the simulations. Several reactions can affect the pore-water pH, including pyrite oxidation, acid neutralization, and secondary-mineral precipitation. Model simulations underpredicted pore-water SO_4 and Fe. It should be noted that the method of pore-water extraction and chemical analysis in Fortin et al. (1996) may be inconsistent with those in the present study, which were more than 20 years apart. As well, the exact location for field measurements in Fortin et al. (1996) was not specified and might not correspond to the NIT.

Figure 4-6 compares the simulated and measured pore-water chemistry after cover placement. The simulated pH profile at present time matched well with the average field-measured pH from six sampling events. Simulated SO_4 and elemental concentrations were generally within the range measured in the field and followed the depth trend, despite minor discrepancies. The agreement between the measured and the simulated pore-water

chemistry suggests that the conceptual model represented the hydrogeochemistry of the tailings under the composite cover relatively well.

Aluminum concentrations were slightly overpredicted. Aqueous Al was derived from a variety of mineral dissolution processes, including albite, anorthite, and muscovite. SI calculations indicated that gibbsite precipitation was likely, but Al hydroxysulfate phases, including jurbanite, alunite, and basaluminite, were not likely to precipitate.

In addition, model calibration revealed that prescribing the water table at 0.2 m above the bottom of the tailings before cover placement was essential for fitting the aqueous Al concentrations close to the range of the measure values. Alternative simulation results with a constant water table at the bottom of the tailings throughout the duration of the simulation are presented in Appendix G. Although concentrations of SO_4 and elements except for Al still matched well with measure values, pH was underpredicted and Al concentrations were overpredicted by an order of magnitude by the alternative model (Appendix G). A higher water table resulted in greater moisture content throughout the profile, which subsequently limitedO_2 diffusion, leading to lower rates of sulfide oxidation and higher pore-water pH. Gibbsite precipitation was the only mechanism controlling pore-water Al concentrations; gibbsite solubility increases rapidly with decreasing pH (May et al. 1979); the sensitivity of aqueous Al concentrations to pore-water pH and sulfide oxidation rates was also confirmed later in this study (§4.4.5).

Nevertheless, prescribing water-table changes to the model introduced discrepancies between the simulated and the measured pore-water chemistry at the bottom 20 cm of the tailings (Figure 4-6); the pH was overpredicted and elemental concentrations were underpredicted. Seasonal water-table fluctuations were observed in the field investigation (Chapter 2) but not included in the simulations. Seasonal water-table fluctuations were omitted to facilitate model convergence but likely resulted in these discrepancies.

Simulation of the cover geochemistry yielded reasonable agreement with the field measurements (Figure 4-7). The pH and concentrations of SO_4, Zn, Cu, As, Ca, K, Mg, and Si followed general trends similar to the field measurements, despite minor discrepancies between the simulation and the range of field measurements. Because the sand and clay layers were not contaminant sources and elemental concentrations were generally very low,

exact matches between the simulation and field measurements were challenging. High field-measured Na concentrations in the lower sand may be due impacts of the GCL on the pore-water geochemistry.

Notably, Fe concentrations in the waste rock were underpredicted. Iron concentrations were affected by several processes, including pyrite oxidation, dissolution/precipitation of siderite, ferrihydrite, jarosite, and natrojarosite, and the redox reaction between Fe^{2+} and Fe^{3+}. Accurate simulation of dissolved Fe was challenging, especially at low concentrations. Other pore-water geochemical parameters relevant to sulfide oxidation (pH and concentrations of SO_4, Zn, Cu) aligned reasonably well with field measurements, suggesting that sulfide oxidation mechanisms in the waste rock were well-simulated. The agreement between simulated and measured Ca, K, and Mg concentrations also suggests that acid-neutralization mechanisms in the waste rock were represented appropriately by the model.

The shrinking core model was widely applied in simulations of mine waste geochemistry (e.g., Davis and Ritchie 1986, Blowes and Jambor 1990, Mayer et al. 2002, Brookfield et al. 2006, Molson et al. 2008, Pabst et al. 2017, Wilson et al. 2018a, 2018b, Kalonji-Kabambi et al. 2020). The application of the shrinking core model yielded reasonable simulations of pH and aqueous Cu, Zn, As, Fe, and SO_4 concentrations in both the tailings and waste rock pore water that compared well with the post-cover field results. However, it did not result in good agreement with the pre-cover aqueous chemistry in the tailings. These observations indicate that the use of the shrinking core model is more representative when reliable and sufficient monitoring data of the aqueous geochemistry are available for calibration.

No previous study has simulated both waste rock and tailings from the same location. Using the same sets of diffusion coefficients for the three sulfide minerals maintained the consistency of sulfide oxidation mechanisms between the tailings and waste rock, which originated from the same ore body. Different scaling factors imply different effective surface areas available for oxidation in the waste rock and tailings. More extensive oxidation occurred under the low moisture content of the waste rock.

Initial calibration reveals that effective diffusion coefficients for Fe^{3+} should be lower than those for $O_{2(aq)}$ to obtain reasonable simulated results; this trend is consistent with Mayer et al. (2002) but deviates from Wilson et al. (2018a, 2018b). Calculations of effective diffusion

coefficient under different temperatures using activation enthalpy of 35 kJ mol^{-1} from Wilson et al. (2018a, 2018b) indicates that changes in D_e with seasonal temperature variations were within an order of magnitude.

Calibrated scaling factors in this study were much smaller than those reported in a previous study (Mayer et al. 2002). The discrepancy in scaling factors may arise from a variety of causes. Optical microscopy revealed the frequent occurrence of intergrown sulfides or sulfides within a quartz matrix in the tailings (§3.5.2), which likely reduced the surface areas available for oxidation. Snow cover and low winter temperatures slowed O_2 diffusion and the rate of sulfide oxidation. The high moisture content (θ_w) in the spring by snowmelt infiltration also reduced O_2 transport. In addition, freeze-thaw induced changes in water flow and reaction rates were not incorporated in the simulations. All of these processes render sulfide oxidation seasonally slow. Because these processes were not accounted for in the simulation, they were indirectly reflected in the smaller scaling factors.

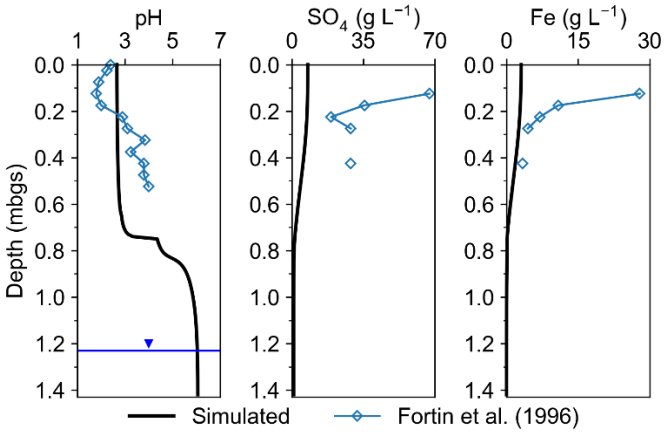

Figure 4-5. Simulated tailings aqueous geochemistry after approximately 24 years compared to field data collected in 1994 from Fortin et al., (1996). The water table (blue inverted triangle) was calibrated to be 0.2 m above the bottom of the tailings before cover placement.

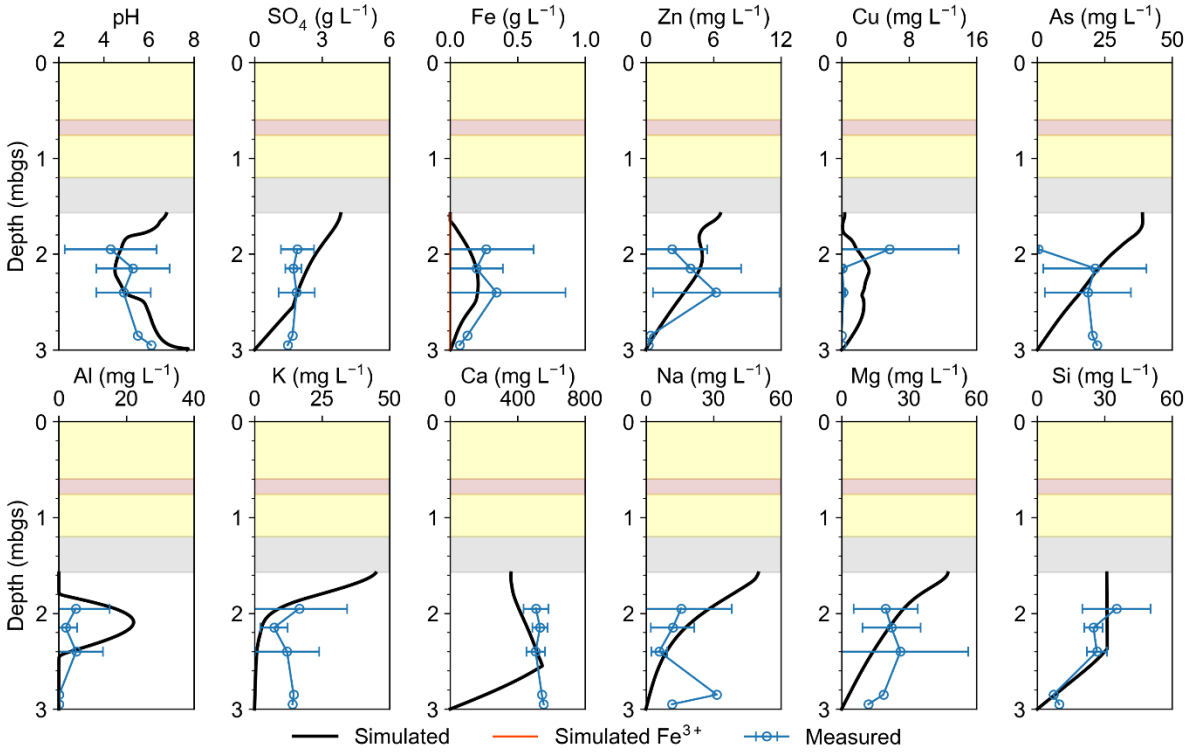

Figure 4-6. Simulated tailings aqueous geochemistry after approximately 50 years (early 2020) under ideal cover conditions (0.01% P_{O2}) compared to field results of six sampling events from 2017 to 2021 at KK4. The water table was prescribed at the bottom of the tailings.

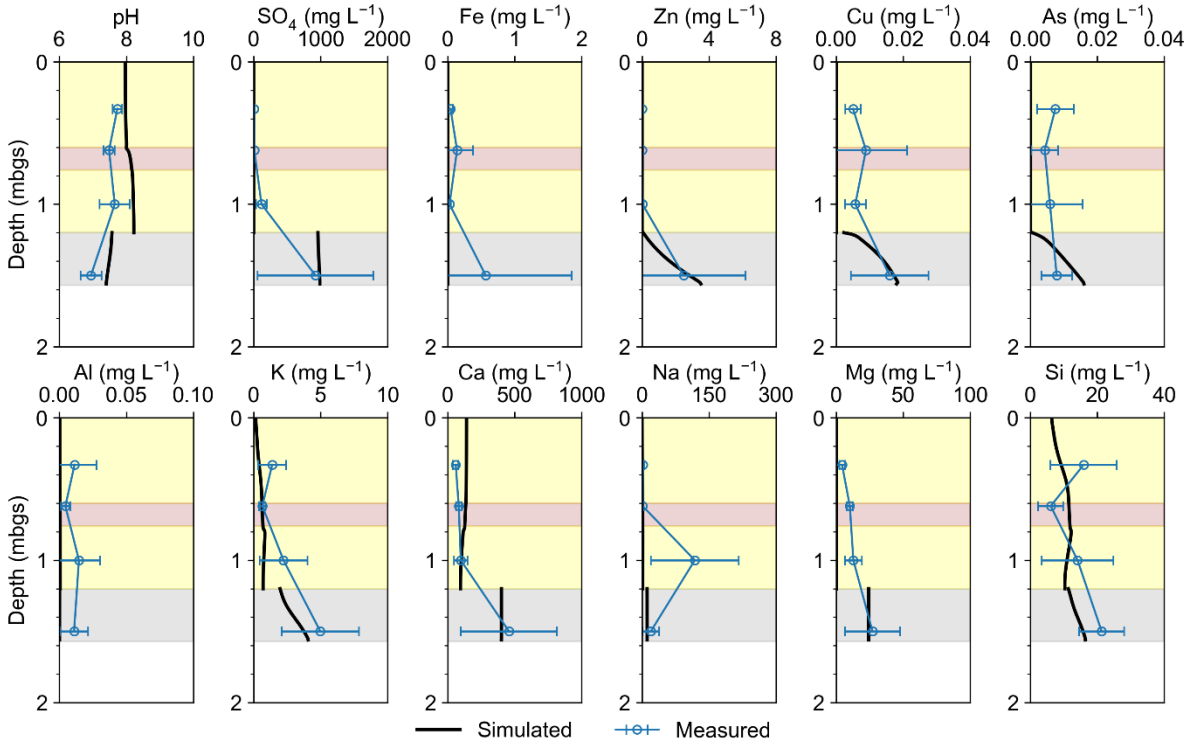

Figure 4-7. Simulated cover aqueous geochemistry after approximately 12 years (early 2020) compared to field results of six sampling events from 2017 to 2021 at KK4.

4.4.2 Sulfide oxidation and cover effectiveness

Simulated changes in tailings geochemical parameters, including pH, aqueous chemical concentrations, mineral volume fractions (φ) of key primary and secondary minerals, and pyrite oxidative dissolution rates over time are shown in Figure 4-8. Small-scale temporal fluctuations in geochemical parameters resulted primarily from the seasonal temperature cycle and secondarily from transient infiltration at the top zone of the tailings.

Before cover placement, the rates of pyrite dissolution via $O_{2(aq)}$ and Fe^{3+} near the surface of the tailings remained high for decades, with the oxidation rate by $O_{2(aq)}$ higher than that by Fe^{3+}. In the middle and at the bottom of the tailings, pyrite oxidation by Fe^{3+} was faster than that by $O_{2(aq)}$ due to lower availability of O_2. Rates of oxidation by both Fe^{3+} and $O_{2(aq)}$ increased gradually over time. Elevated concentrations of SO_4 were present throughout the tailings. Oxidizing and acidic conditions also promoted the oxidation of Fe^{2+} to Fe^{3+}, resulting

in higher concentrations of Fe^{3+} than Fe^{2+} throughout the upper and middle zones of the tailings, which subsequently promoted Fe^{3+} oxidation of sulfides.

After cover placement, the rate of pyrite oxidation by $O_{2(aq)}$ at all depths of the tailings decreased sharply due to a decline in O_2 availability i.e., a change in the boundary condition. The rate of pyrite oxidation rate by Fe^{3+} decreased modestly after cover placement. The abundance of Fe^{3+} in the geochemical system, especially at shallow depths, continued to facilitate pyrite oxidation after decades of subaerial sulfide weathering. Nevertheless, lower O_2 availability under the cover prevented the regeneration of Fe^{3+} by Fe^{2+} oxidation, and Fe^{3+} concentrations declined rapidly. At all depths of the tailings, pore-water pH increased gradually at first, and sharply about 10 years after cover placement (Figure 4-8) corresponding to decreases in acidity generation. Increases in pH also corresponded to decreases in SO_4 concentrations. These results suggest that lower O_2 availability under a composite cover lowered sulfide oxidation rates by both $O_{2(aq)}$ and Fe^{3+} and curbed subsequent AMD generation. Oxidation by Fe^{3+} did not slow down as much as oxidation by $O_{2(aq)}$. These findings are consistent with those of Pabst et al. (2017, 2018).

In addition, less infiltration (Figure 4-4) after cover placement also reduced the downward transport of SO_4. This change is most evident at the bottom of the tailings, where pyrite oxidation rates were orders of magnitude lower than in the shallower tailings, and pore-water SO_4 was largely derived from downward transport.

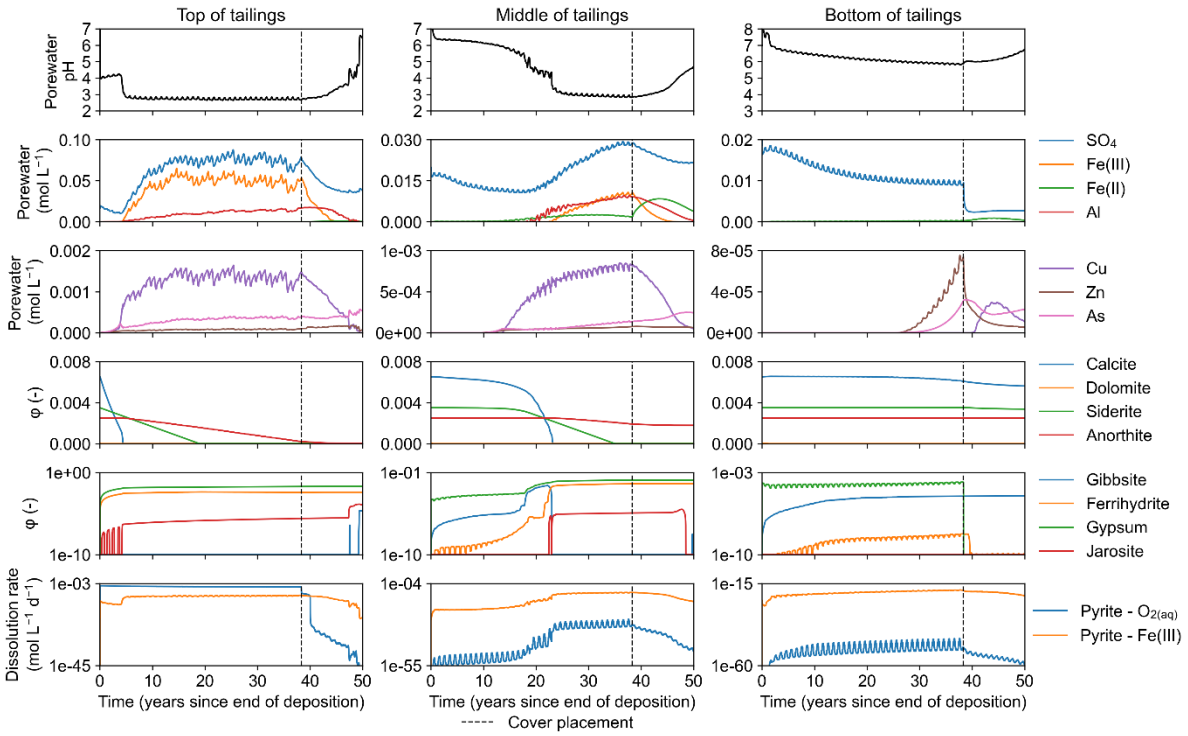

Figure 4-8. Simulated evolution of selected geochemical parameters in the top (inflow), middle, and bottom (outflow) zones of the tailings, including key aqueous geochemical parameters, volume fractions (φ) for primary and secondary minerals, and pyrite oxidative dissolution rates. The vertical dashed line indicates the time of cover placement.

4.4.3 Acid neutralization and secondary-mineral precipitation

Reasonable agreement between the field-measured and the simulated Ca, Mg, Na, and K concentrations indicate that calcite, dolomite, albite, anorthite, and muscovite dissolution as acid-neutralization mechanisms were well-represented. Dolomite, albite, and muscovite were the only source of pore-water Mg, Na, and K, respectively, whereas both calcite and anorthite dissolution leached Ca into the pore water.

Simulated reaction rates and mineral volume fractions indicate that calcite was depleted in five years at the top of the tailings. Calcite depletion corresponded to sharp declines in pore-water pH in the top and the middle zones of the tailings (Figure 4-8). At the bottom of the tailings, calcite was not depleted and maintained circumneutral pore-water pH. During model calibration, the pH-dependent rates of calcite dissolution resulted in better agreement

between measured and simulated pH values than the equilibrium calcite dissolution formulation. Due to the presence of minor masses of dolomite, its dissolution did not have a strong influence on pore-water pH. Siderite dissolution was slower than that of calcite. In the top zone of the tailings, siderite was depleted after 20 years and did not correspond to distinct changes in pore-water pH.

The simulations indicated that precipitation of gibbsite did not occur in the top zone of the tailings before cover placement. In the middle tailings zone, the gibbsite φ initially increased and peaked when calcite was depleted, but it was depleted sharply afterwards (Figure 4-8). Gibbsite precipitation and dissolution corresponded to a small plateau near pH 4 before dropping to <3. In the bottom tailings zone, gibbsite content increased steadily over time. After cover placement, gibbsite precipitation occurred in the top and middle tailings zones, when pH increased. This reaction controlled pore-water Al concentrations.

Anorthite was the most abundant aluminosilicate mineral in the simulation. Sensitivity analysis found that changes in anorthite φ and S had the biggest impact on pore-water pH among the aluminosilicate minerals. In the top zone of the tailings, anorthite was depleted after around 40 years. In the middle zone of the tailings, anorthite φ started decreasing after the depletion of calcite but levelled off after cover placement. No noticeable change in anorthite content occurred at the bottom of the tailings.

The maximum simulated ferrihydrite volume fraction in the vertical profile at the end of the simulation period was 1.1×10^{-2}. Meanwhile, the maximum amount of selectively extracted crystalline oxyhydroxides (§3.5.4) is 5 wt% at KK4 (Figure 3-9), i.e., 1.7×10^{-2} in volume fraction. The simulated and extracted Fe(III) oxyhydroxides correspond well; this indicates that the precipitation mechanism for Fe(III) oxyhydroxides was well-represented.

Simulations showed that large volumes of ferrihydrite precipitated in the top and middle zones of the tailings. Increases in ferrihydrite φ corresponded to relatively high pore-water pH and low Fe^{3+} concentrations. Ferrihydrite φ values were little changed after pore-water pH dropped <3, which also corresponded to increases in Fe^{3+} concentrations. Dissolution/precipitation of ferrihydrite was the main mechanism contributing to pore water acid neutralization after the depletion of carbonates and gibbsite.

Natrojarosite φ followed a similar trend as jarosite φ so only jarosite φ was shown. Jarosite precipitated in minor amounts compared to ferrihydrite and gypsum. Steady precipitation of jarosite corresponded to low pH conditions in the tailings at the top and in the middle of the tailings, whereas jarosite did not precipitate at the bottom of the tailings.

Gypsum was the most abundant secondary mineral and precipitated throughout the 1-D domain. Increases in gypsum volume fractions occurred after calcite content depletion occurred in the top and the middle tailings zones, suggesting that gypsum precipitation was controlled by the availability of Ca^{2+} in the pore water. Despite abundant gypsum precipitation, aqueous concentrations of SO_4 remained elevated (up to 3 g L^{-1})

4.4.4 Trace element mobility after cover placement

Copper concentrations decreased markedly after cover placement (Figure 4-8); this is mainly due to enhanced sorption of Cu under higher pH (Table 4-3), in addition to slower chalcopyrite oxidation. In contrast, Zn concentrations increased after cover placement at the top of the tailings due to the inflow of elevated Zn concentrations in the pore water from the waste rock layer. Zinc concentrations were little changed in the middle and decreased at the bottom of the tailings. Although Zn sorption was also enhanced under higher pH, Zn has much less affinity for sorption than Cu (Table 4-3). Despite slower sphalerite oxidation rates and less downward transport, limited sorption capacity resulted in steady Zn concentrations in the tailings.

Dissolved As concentrations increased with time and the increasing trend continued at the top and in the middle of the tailings after cover placement. At the bottom of the tailings, As concentrations levelled off from an increasing trend due to the decline in As-bearing pyrite oxidation and less downward transport. Under higher pH, desorption of arsenite from hydrous ferric oxide can release As into the pore water (Dzombak and Morel 1991), which contributed to the mobility of As.

4.4.5 Cover defect scenario

An alternative tailings reactive transport scenario was simulated to represent a defective cover that did not effectively inhibit O_2 transport into the tailings, because pore-gas measurements and aqueous geochemical results suggest that defects in the cover may

have developed over time at KK4 (Chapter 3). This scenario was facilitated by prescribing 10% P_{O2} at the inflow boundary while maintaining all other input parameters consistent with the base model. The results in Figure 4-9 showed that when defects in the cover occur, sulfide oxidation and AMD generation continued at high rates and result in low pH and elevated concentrations of SO_4 and other species. Concentrations of Cu and Al were orders of magnitude higher than the base model, pH was markedly lower, and concentrations of SO_4 and Fe were also much higher. These results suggest that concentrations of Cu and Al were the most sensitive to the effectiveness of the cover, followed by pH and concentrations of SO_4 and Fe. Notably, Fe^{3+} dominated over Fe^{2+} at shallow depths similar to pre-cover conditions. In contrast, concentrations of Zn, As, Ca, Mg, and Si did not show pronounced differences from the base case, suggesting they are relatively insensitive to cover performance. Low concentrations of K and Na were largely due to enhanced precipitation of jarosite and natrojarosite under lower pH conditions, which sequestered aqueous Fe to a limited extent.

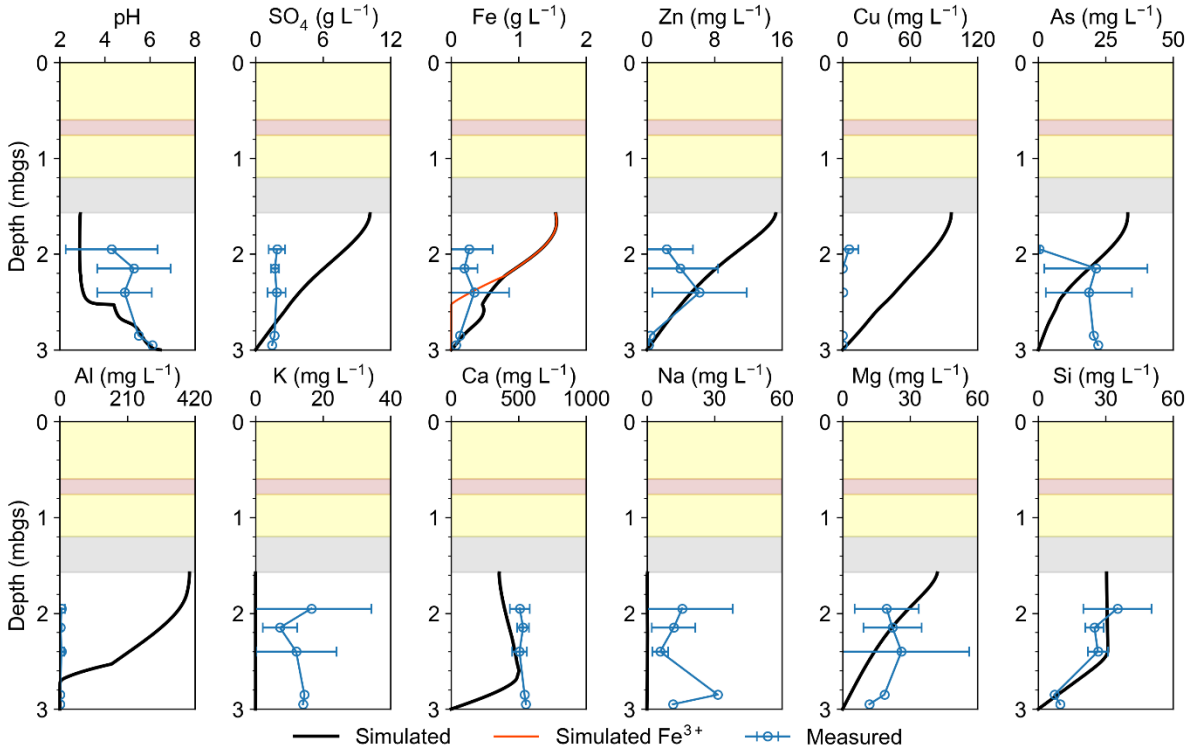

Figure 4-9. Simulated tailings aqueous geochemistry after approximately 50 years (early 2020) under defective cover condition (10% P_{O2}) compared to field results of six sampling events from 2017 to 2021 at KK4.

4.4.6 Future forecast

The duration of the current simulations was extended by another 50 years to forecast long-term tailings hydrogeochemistry under the composite cover. Transient upper boundary fluxes to the tailings were synthesized from monthly infiltration of previous years (2008-2020). All other parameters were the same as the base case, including the post-cover seasonal temperature cycle (Appendix G). Pore-water pH at all depths of the tailings stabilizes >7 approximately 53 years after the end of deposition (Figure 4-10). As well, concentrations of pore-water Fe^{2+}, Fe^{3+}, Al, Cu, and $O_{2(aq)}$ stabilize at all depths. A gradually decreasing trend was observed for aqueous As concentrations at all depths. A gradually increasing trend was observed for the concentrations of SO_4 and Zn in the top and middle zones of the tailings; together with stabilized rates of sulfide oxidation, this trend indicates that sulfide oxidation continues to occur at slow rates. Volume fractions for most primary and secondary minerals also stabilize over time. Calcite precipitation is enhanced at the top zone of the tailings under higher pH and availability of Ca^{2+}. Precipitation of gypsum and ferrihydrite remains stable in the top and middle zones of the tailings and gibbsite precipitation sequesters aqueous Al at all depths.

In the top zone of the tailings, a reversal in the trend of pyrite oxidation rate by $O_{2(aq)}$ was observed between year 49 and year 51, concomitant with a decrease in Fe^{2+} concentrations and an increase in $O_{2(aq)}$ concentrations. Immediately after cover placement, there was an accumulation of aqueous Fe^{2+} at all depths of the tailings, which is attributed to a lack of O_2 availability to facilitate the oxidation of Fe^{2+} to Fe^{3+}. As well, high aqueous Fe^{2+} promoted $O_{2(aq)}$ consumption and further reduced the rate of pyrite oxidation by $O_{2(aq)}$. At the start of the future simulation, a combination of slower sulfide oxidation and downward transport results in lower Fe^{2+} concentrations in the top zone of the tailings. Less O_2 consumption by reaction with Fe^{2+} causes $O_{2(aq)}$ to increase and stabilize to the same magnitude (10^{-7} mol L^{-1}) as those immediately after cover placement. Subsequently, the rate of pyrite oxidation by $O_{2(aq)}$ also increases to the same magnitude (10^{-9} mol L^{-1} d^{-1}) as those immediately after

cover placement. Similar trends in Fe^{2+} concentrations occur in the middle and lower zones of the tailings, albeit much less pronounced.

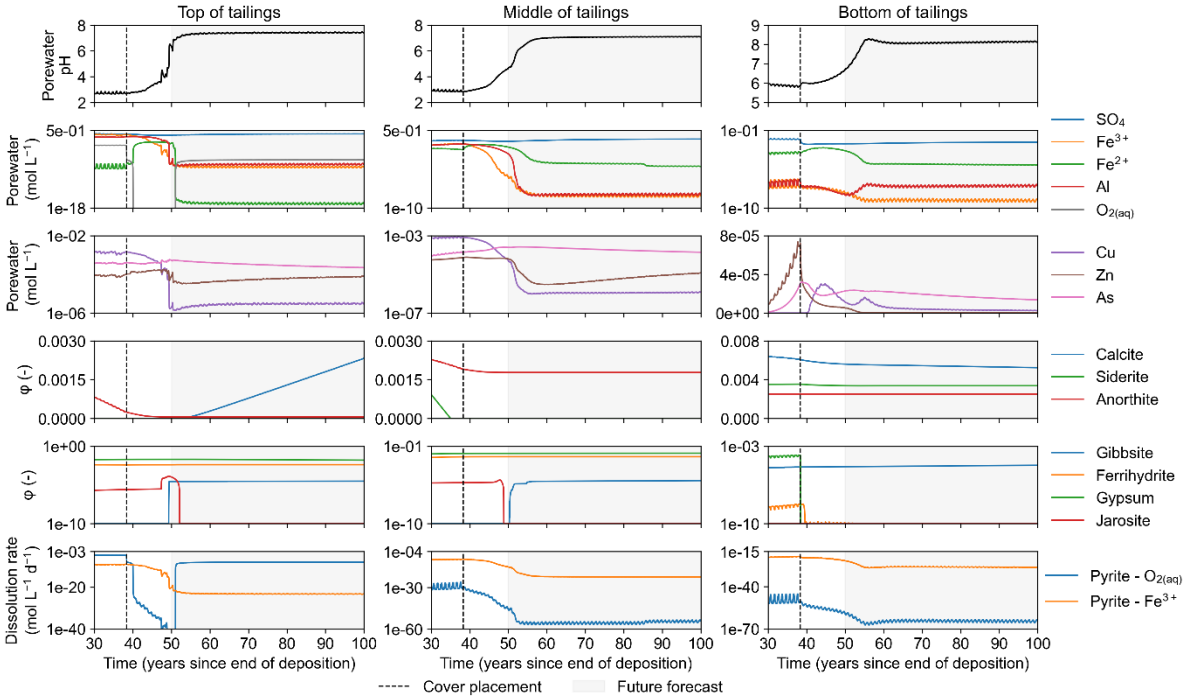

Figure 4-10. Future forecast (grey areas) of selected geochemical parameters in the top (inflow), middle, and bottom (outflow) zones of the tailings.

4.4.7 Model limitations

The lack of accurate mineralogy data on the tailings before deposition created challenges for initial volume fraction input. Mineralogy data from the deepest core intervals were adopted and adjusted for model input. However, these data were collected after 50 years of AMD impact and may not represent the initial mineralogy; this limitation is especially problematic for carbonate minerals, which were minor phases and reacted relatively rapidly in the presence of acidic drainage. The absence of reliable aqueous geochemical data in the tailings before cover placement was another challenge that added uncertainties to the simulations. Spatial heterogeneity within the tailings, the lack of reliable pre-cover field sampling and analysis techniques, and the lack of consistent monitoring programs all

contributed to the lack of data based on which accurate model calibrations can be conducted.

Uniqueness in the model parameters is unlikely, especially for the input parameters for the shrinking core model due to a large number of calibrated parameters. Laboratory- or field-based experiments that yield estimates of the effective diffusion coefficients or effective surface areas of sulfide minerals can better constrain the parameters and increase the validity of the simulations.

Many simplifications were made in the simulations because the complex hydrogeochemical processes cannot be comprehensively recreated in the simulations. Omitting seasonal water table fluctuations promoted model convergence but simplified the flow system. The degree of change in the water table position before and after cover placement was calibrated due to a lack of field measurements. Freeze-thaw and its impact on hydraulic conductivity and reaction rates were ignored. It was assumed that the mineralogy and material properties in the tailings and each of the cover layers were homogenous, despite observations of heterogeneity from field studies. Prescribing fixed concentrations of the average waste rock pore-water chemistry at the inflow reactive transport boundary after cover placement ignored transient changes in the geochemistry of the waste rock effluent. A gradual decline of the water table after cover placement, if present, was also not taken into consideration due to a lack of monitoring data.

Several relevant geochemical reactions were omitted from the simulation for simplification. Arsenate [H_3AsO_4] was not included as an aqueous component; the redox reaction between As(III) and As(V) is an important process in mine waste since As(III) is more mobile and toxic than As(V) (Smedley and Kinniburgh 2002). Wilson et al. (2018a, 2018b) incorporated intermediate S components to simulate biologically mediated sulfide oxidation more accurately; this was not included in the current study and oxidation was assumed to proceed directly to completion. Pyrrhotite was not included as a primary mineral due to similarities between the weathering products of pyrrhotite and pyrite. Precipitation of covellite under more reduced conditions acted as a sink for aqueous Cu (Chapter 3). Because the incorporation of sorption resulted in good agreement between simulated and measured aqueous Cu, covellite precipitation was omitted. Reductive dissolution and sulfate reduction

could play an important role in mine waste remediation assessment; nevertheless, they were not found to be significant at KK4, the simulated sampling location, due to very low organic carbon availability (Chapter 3). In the current simulations, sorption parameters for HFO were set as constant and were not related to the dissolution/precipitation of ferrihydrite. The lack of activation enthalpy or activation energy for sulfide oxidation ignored temperature dependency in sulfide oxidation reactions.

4.5 Conclusions

The overall agreement between the simulated and the measured post-cover aqueous geochemical parameters suggests that the conceptual model captured the hydrogeochemical evolution of the legacy tailings under a composite cover. Key processes incorporated in the conceptual model and interrogated by model calibration include transient monthly infiltration/influxes, a dynamic temperature regime, cover placement as a change in upper boundary flow and reactive transport, a decline in water-table elevation after cover placement, the application of the shrinking core model for the oxidation of As-bearing pyrite, chalcopyrite and sphalerite, acid neutralization by carbonates, Al hydroxides, and Fe oxyhydroxides, precipitation of secondary minerals, and sorption to HFO. Using the same diffusion coefficients for waste rock and tailings but different scaling factors ensured consistent sulfide oxidation mechanisms. A lack of reliable data on initial tailings mineralogy and hydrogeochemistry before cover placement confounded model calibration and increased uncertainty. A few key assumptions were made, such as homogeneous material properties and mineralogy for each layer, ignoring seasonal water-table fluctuations, and omitting geochemical processes that did not make meaningful differences in model output.

Modelled reaction rates reveal that where intact, the cover decreased sulfide oxidation rates by both $O_{2(aq)}$ and Fe^{3+}. Pore-water pH increased, and concentrations of Fe, Al, and Cu decreased at all depths of the tailings over time. These results indicate that the composite cover reduces AMD generation and transport in the long term. Concentrations of SO_4, Zn, and As continued to be elevated after cover placement. Simulation results of an alternative scenario with defects in the cover suggest that concentrations of Cu and Al were the most sensitive to changes in O_2 availability resulting from the decline in cover performance whereas the pH and concentrations of SO_4 and Fe were also affected. The results of 50-

year future forecast suggest that aqueous SO_4, Zn, and As continue to be elevated whereas other key parameters, including pyrite oxidation rates, stabilize with time.

The reactive transport simulations complement ongoing field and laboratory characterization of the complex hydrogeochemistry in the legacy tailings site and provided a quantitative evaluation of cover effectiveness. This study also indicates that site-specific hydrogeochemical characterization for reactive transport simulations of mine wastes and their remediation should include sufficient hydrological and hydrogeological monitoring, physical property characterization, the presence and content of key primary and secondary minerals, and pore-water and groundwater chemistry from multi-year sampling events.

References

Aachib, M., Mbonimpa, M., and Aubertin, M. 2004. Measurement and prediction of the oxygen diffusion coefficient in unsaturated media, with applications to soil covers. Water, Air, & Soil Pollution, **156**: 163–193. doi:10.1023/B:WATE.0000036803.84061.e5.

Adu-Wusu, C., and Yanful, E.K. 2006. Performance of engineered test covers on acid-generating waste rock at Whistle mine, Ontario. Canadian Geotechnical Journal, **43**: 1–18. doi:10.1139/t05-088.

Al, T.A., Martin, C.J., and Blowes, D.W. 2000. Carbonate-mineral/water interactions in sulfide-rich mine tailings. Geochimica et Cosmochimica Acta, **64**: 3933–3948. doi:10.1016/S0016-7037(00)00483-X.

Albrecht, B.A., and Benson, C.H. 2001. Effect of desiccation on compacted natural clays. Journal of Geotechnical and Geoenvironmental Engineering, **127**: 67–75. doi:10.1061/(ASCE)1090-0241(2001)127:1(67).

Allen, R.G., Pereira, L.S., Raes, D., and Smith, M. 1998. Crop evapotranspiration. Guidelines for computing crop water requirements. *In* FAO Irrigation and Drainage Paper 56. Food and Agriculture Organization of the United Nations, Rome.

Amirbahman, A., Schönenberger, R., Johnson, C.A., and Sigg, L. 1998. Aqueous- and solid-phase biogeochemistry of a calcareous aquifer system downgradient from a municipal solid waste landfill (Winterthur, Switzerland). Environmental Science & Technology, **32**. doi:10.1021/es970810j.

Amos, R.T., Blowes, D.W., Bailey, B.L., Sego, D.C., Smith, L., and Ritchie, A.I.M. 2015. Waste-rock hydrogeology and geochemistry. Applied Geochemistry, **57**: 140–156. doi:10.1016/j.apgeochem.2014.06.020.

ASTM. 2015. ASTM D5856-15. Standard Test Method for Measurement of Hydraulic Conductivity of Porous Material Using a Rigid-Wall, Compaction-Mold Permeameter. ASTM International, West Conshohocken, PA. Available from https://www.astm.org/d5856-15.html [accessed 7 July 2022].

ASTM. 2017. ASTM D6913/D6913M-17. Standard Test Methods for Particle-Size Distribution (Gradation) of Soils Using Sieve Analysis. ASTM International, West Conshohocken, PA. [accessed 2 January 2022].

Aubertin, M., Aachib, M., and Authier, K. 2000. Evaluation of diffusive gas flux through covers with a GCL. Geotextiles and Geomembranes, **18**: 215–233. doi:10.1016/S0266-1144(99)00028-X.

Aubertin, M., Bussière, B., Pabst, T., James, M., and Mbonimpa, M. 2016. Review of the reclamation techniques for acid-generating mine wastes upon closure of disposal sites. *In* Geo-Chicago 2016. American Society of Civil Engineers, Reston, VA. pp. 343–358. doi:10.1061/9780784480137.034.

Aubertin, M., Cifuentes, E., Apithy, S.A., Bussière, B., Molson, J., and Chapuis, R.P. 2009. Analyses of water diversion along inclined covers with capillary barrier effects. Canadian Geotechnical Journal, **46**: 1146–1164. doi:10.1139/T09-050.

Aubertin, M., Ricard, J.-F., and Chapuis, R.P. 1998. A predictive model for the water retention curve: application to tailings from hard-rock mines. Canadian Geotechnical Journal, **35**: 55–69. doi:10.1139/t97-080.

Baker, R.S., and Hillel, D. 1990. Laboratory tests of a theory of fingering during infiltration into layered soils. Soil Science Society of America Journal, **54**. doi:10.2136/sssaj1990.03615995005400010004x.

Ball, J.W., and Nordstrom, D.K. 1991. User's manual for WATEQ4F, with revised thermodynamic data base and test cases for calculating speciation of minor, trace and redox elements in natural. Menlo Park, California.

Bao, Z., Al, T., Bain, J., Shrimpton, H.K., Finfrock, Y.Z., Ptacek, C.J., and Blowes, D.W. 2022. Sphalerite weathering and controls on Zn and Cd migration in mine waste rock: An integrated study from the molecular scale to the field scale. Geochimica et Cosmochimica Acta, **318**: 1–18. doi:10.1016/j.gca.2021.11.007.

Benson, C.H., Abichou, T.H., Olson, M.A., and Bosscher, P.J. 1995. Winter effects on hydraulic conductivity of compacted clay. Journal of Geotechnical Engineering, **121**: 69–79. doi:10.1061/(ASCE)0733-9410(1995)121:1(69).

Benson, C.H., Thorstad, P.A., Jo, H.-Y., and Rock, S.A. 2007. Hydraulic performance of geosynthetic clay liners in a landfill final cover. Journal of Geotechnical and Geoenvironmental Engineering, **133**: 814–827. doi:10.1061/(ASCE)1090-0241(2007)133:7(814).

Bigham, J.M., and Nordstrom, D.K. 2000. Iron and aluminum hydroxysulfates from acid sulfate waters. Reviews in Mineralogy and Geochemistry, **40**: 351–403. doi:10.2138/rmg.2000.40.7.

Binning, P.J., Postma, D., Russell, T.F., Wesselingh, J.A., and Boulin, P.F. 2007. Advective and diffusive contributions to reactive gas transport during pyrite oxidation in the unsaturated zone. Water Resources Research, **43**. doi:10.1029/2005WR004474.

Blowes, D.W., and Jambor, J.L. 1990. The pore-water geochemistry and the mineralogy of the vadose zone of sulfide tailings, Waite Amulet, Quebec, Canada. Applied Geochemistry, **5**: 327–346. doi:10.1016/0883-2927(90)90008-S.

Blowes, D.W., Ptacek, C.J., Jambor, J.L., Weisener, C.G., Paktunc, D., Gould, W., and Johnson, D. 2014. The geochemistry of acid mine drainage. *In* Treatise on Geochemistry, 2nd edition. *Edited by* H.D. Holland and K.K. Turekian. Elsevier, San Diego. pp. 131–190. doi:http://dx.doi.org/10.1016/B978-0-08-095975-7.00905-0.

Boorman, R.S., and Watson, D.M. 1975. Chemical processes in abandoned sulfide tailings dumps and environmental implications for Northeastern New Brunswick. CIM Bulletin, **69**: 86–96.

Bouazza, A. 2002. Geosynthetic clay liners. Geotextiles and Geomembranes, **20**: 3–17. doi:10.1016/S0266-1144(01)00025-5.

Brookfield, A.E., Blowes, D.W., and Mayer, K.U. 2006. Integration of field measurements and reactive transport modelling to evaluate contaminant transport at a sulfide mine tailings impoundment. Journal of Contaminant Hydrology, **88**. doi:10.1016/j.jconhyd.2006.05.007.

Calder Engineering Ltd. 2013. Hydrological Assessment of the Kam Kotia Mine Site. Kleinburg, Ontario.

Chung, S.-O., and Horton, R. 1987. Soil heat and water flow with a partial surface mulch. Water Resources Research, **23**: 2175–2186. doi:10.1029/WR023i012p02175.

Collin, M. 1998. The Bersbo pilot project: numerical simulation of water and oxygen transport in the soil covers at the mine waste deposits. Swedish Environmental Protection Agency. Report 4763. Stockholm.

Collin, M., and Rasmuson, A. 1988. A comparison of gas diffusivity models for unsaturated porous media. Soil Science Society of America Journal, **52**. doi:10.2136/sssaj1988.03615995005200060007x.

Dansgaard, W. 1964. Stable isotopes in precipitation. Tellus, **16**: 436–468.

Davis, G.B., and Ritchie, A.I.M. 1986. A model of oxidation in pyritic mine wastes: part 1 equations and approximate solution. Applied Mathematical Modelling, **10**: 314–322. doi:10.1016/0307-904X(86)90090-9.

Dixit, S., and Hering, J.G. 2003. Comparison of arsenic(V) and arsenic(III) sorption onto iron oxide minerals: implications for arsenic mobility. Environmental Science & Technology, **37**: 4182–4189. doi:10.1021/es030309t.

Dove, P.M., and Czank, C.A. 1995. Crystal chemical controls on the dissolution kinetics of the isostructural sulfates: Celestite, anglesite, and barite. Geochimica et Cosmochimica Acta, **59**: 1907–1915. doi:10.1016/0016-7037(95)00116-6.

Dzombak, D.A., and Morel, F.M.M. 1991. Surface Complexation Modeling: Hydrous Ferric Oxide. John Wiley & Sons, New York.

Environment and Climate Change Canada. 2021. Canadian Climate Normals 1981-2010 Station Data - Timmins Victor Power A. Available from https://climate.weather.gc.ca/climate_normals/ [accessed 9 May 2022].

Environment and Climate Change Canada. 2022. Historical Data [Data set]. Available from https://climate.weather.gc.ca/historical_data/search_historic_data_e.html [accessed 9 May 2022].

ESRF ID21. 2022. Database inorganic sulfur compounds. Available from https://www.esrf.fr/home/UsersAndScience/Experiments/XNP/ID21/php.html [accessed 3 October 2022].

Fortin, D., Davis, B., and Beveridge, T.J. 1996. Role of Thiobacillus and sulfate-reducing bacteria in iron biocycling in oxic and acidic mine tailings. FEMS Microbiology Ecology, **21**: 11–24. doi:10.1016/0168-6496(96)00039-6.

Freeze, R.A., and Cherry, J.A. 1979. Groundwater. Prentice-Hall.

van Genuchten, M.Th. 1980. A closed-form equation for predicting the hydraulic conductivity of unsaturated soils. Soil Science Society of America Journal, **44**: 892–898. doi:10.2136/sssaj1980.03615995004400050002x.

Geologic Testing Consultants. 1984. Kam Katia Tailings Reclamation Project. Timmins, Ontario. Detailed Hydrogeological Investigations Program 1983-1984.

Gliński, J., and Stępniewski, W. 1985. Soil Aeration and its Role for Plants. CRC Press. doi:10.1201/9781351076685.

Goldhaber, M., and Kaplan, I. 1975. Controls and consequences of sulfate reduction rates in recent marine sediments. Soil Science, **119**: 42–55.

Graham, J., and Au, V.C.S. 1985. Effects of freeze–thaw and softening on a natural clay at low stresses. Canadian Geotechnical Journal, **22**: 69–78. doi:10.1139/t85-007.

Gunsinger, M.R., Ptacek, C.J., Blowes, D.W., Jambor, J.L., and Moncur, M.C. 2006. Mechanisms controlling acid neutralization and metal mobility within a Ni-rich tailings impoundment. Applied Geochemistry, **21**: 1301–1321. doi:10.1016/j.apgeochem.2006.06.006.

Hamblin, C.D. 2003. Ontario leads the way in abandoned mines rehabilitation. *In* Proceedings of the Sudbury 2003: Mining and the Environment Conference, Sudbury, Ontario, May 25 – 28, 2003.

Hamblin, C.D. 2008. The ongoing rehabilitation of Ontario's Kam Kotia mine: an abandoned acid generating tailings site. *In* MEND Manitoba Workshop. June 4-5, 2008.

Heron, Gorm., Crouzet, Catherine., Bourg, A.C.M., and Christensen, T.H. 1994. Speciation of Fe(II) and Fe(III) in contaminated aquifer sediments using chemical extraction techniques. Environmental Science & Technology, **28**. doi:10.1021/es00058a023.

Holmström, H., Salmon, U.J., Carlsson, E., Petrov, P., and Öhlander, B. 2001. Geochemical investigations of sulfide-bearing tailings at Kristineberg, northern Sweden, a few years after remediation. Science of The Total Environment, **273**. doi:10.1016/S0048-9697(00)00850-0.

Hosney, M.S., and Rowe, R.K. 2013. Changes in geosynthetic clay liner (GCL) properties after 2 years in a cover over arsenic-rich tailings. Canadian Geotechnical Journal, **50**: 326–342.

Hvorslev, M.J. 1951. Time lag and soil permeability in ground-water observations. US Army Corps of Engineers, Waterways Experiment Station Bulletin 36, Vicksburg, Mississippi.

IAEA/WMO. 2022. Global Network of Isotopes in Precipitation. The GNIP Database. Available from https://nucleus.iaea.org/wiser [accessed 20 March 2022].

Johnson, D.B., and Hallberg, K.B. 2008. Carbon, iron and sulfur metabolism in acidophilic micro-organisms. *In* Advances in Microbial Physiology. pp. 201–255. doi:10.1016/S0065-2911(08)00003-9.

Kalonji-Kabambi, A., Demers, I., and Bussière, B. 2020. Reactive transport modeling of the geochemical behavior of highly reactive tailings in different environmental conditions. Applied Geochemistry, **122**. doi:10.1016/j.apgeochem.2020.104761.

Kim, H., and Benson, C.H. 2004. Contributions of advective and diffusive oxygen transport through multilayer composite caps over mine waste. Journal of Contaminant Hydrology, **71**: 193–218. doi:10.1016/j.jconhyd.2003.10.001.

Kimball, B.A., and Lemon, E.R. 1971. Air turbulence effects upon soil gas exchange. Soil Science Society of America Journal, **35**. doi:10.2136/sssaj1971.03615995003500010013x.

Koerner, R.M., and Daniel, D.E. 1997. Final Covers for Solid Waste Landfills and Abandoned Dumps. Thomas Telford, London, U.K.

Lindsay, M.B.J., Blowes, D.W., Condon, P.D., and Ptacek, C.J. 2011. Organic carbon amendments for passive in situ treatment of mine drainage: Field experiments. Applied Geochemistry, **26**. doi:10.1016/j.apgeochem.2011.04.006.

Lovley, D.R., Baedecker, M.J., Lonergan, D.J., Cozzarelli, I.M., Phillips, E.J.P., and Siegel, D.I. 1989. Oxidation of aromatic contaminants coupled to microbial iron reduction. Nature, **339**. doi:10.1038/339297a0.

Mackasey, W.O. 2000. Abandoned Mines in Canada. MiningWatch Canada. Available from https://miningwatch.ca/sites/default/files/mackasey_abandoned_mines.pdf.

May, H.M., Helmke, P.A., and Jackson, M.L. 1979. Gibbsite solubility and thermodynamic properties of hydroxy-aluminum ions in aqueous solution at 25°C. Geochimica et Cosmochimica Acta, **43**: 861–868. doi:10.1016/0016-7037(79)90224-2.

Mayer, K.U., Frind, E.O., and Blowes, D.W. 2002. Multicomponent reactive transport modeling in variably saturated porous media using a generalized formulation for kinetically controlled reactions. Water Resources Research, **38**: 1174–1194. doi:10.1029/2001WR000862.

Mbonimpa, M., Aubertin, M., Aachib, M., and Bussière, B. 2003. Diffusion and consumption of oxygen in unsaturated cover materials. Canadian Geotechnical Journal, **40**: 916–932. doi:10.1139/t03-040.

McCreadie, H., Blowes, D.W., Ptacek, C.J., and Jambor, J.L. 2000. Influence of reduction reactions and solid-phase composition on porewater concentrations of arsenic. Environmental Science & Technology, **34**. doi:10.1021/es991194p.

MEND. 1999. Etude sur les Barrières Sèches Construites à partir des Résidus Miniers Phase II - Essais en Place. Rapport 2.22.2c. Charlesbourg, Canada.

MEND. 2004. Design, Construction and Performance Monitoring of Cover System for Waste Rock and Tailings. Report 2.21.4. Ottawa, Canada.

Millington, R.J. 1959. Gas diffusion in porous media. Science, **130**: 100–102. doi:10.1126/science.130.3367.100-a.

Millington, R.J., and Quirk, J.P. 1961. Permeability of porous solids. Transactions of the Faraday Society, **57**: 1200–1207. doi:10.1039/TF9615701200.

Molson, J., Aubertin, M., Bussière, B., and Benzaazoua, M. 2008. Geochemical transport modelling of drainage from experimental mine tailings cells covered by capillary barriers. Applied Geochemistry, **23**. doi:10.1016/j.apgeochem.2007.08.004.

Moncur, M.C., Jambor, J.L., Ptacek, C.J., and Blowes, D.W. 2009. Mine drainage from the weathering of sulfide minerals and magnetite. Applied Geochemistry, **24**. doi:10.1016/j.apgeochem.2009.09.013.

Moncur, M.C., Ptacek, C.J., Blowes, D.W., and Jambor, J.L. 2005. Release, transport and attenuation of metals from an old tailings impoundment. Applied Geochemistry, **20**: 639–659. doi:10.1016/j.apgeochem.2004.09.019.

Newville, M. 2013. Larch: an analysis package for XAFS and related spectroscopies. Journal of Physics: Conference Series, **430**: 012007. doi:10.1088/1742-6596/430/1/012007.

Nicholson, R.V., Gillham, R.W., Cherry, J.A., and Reardon, E.J. 1989. Reduction of acid generation in mine tailings through the use of moisture-retaining cover layers as oxygen barriers. Canadian Geotechnical Journal, **26**. doi:10.1139/t89-001.

Nordstrom, D.K., and Archer, D.G. 2003. Arsenic thermodynamic data and environmental geochemistry. *In* Arsenic in Ground Water. *Edited by* A.H. Welch and K.G. Stollenwerk. Kluwer Academic Publishers, Boston, MA. pp. 1–25.

Othman, M.A., and Benson, C.H. 1993. Effect of freeze–thaw on the hydraulic conductivity and morphology of compacted clay. Canadian Geotechnical Journal, **30**: 236–246. doi:10.1139/t93-020.

Pabst, T., Bussière, B., Aubertin, M., and Molson, J. 2018. Comparative performance of cover systems to prevent acid mine drainage from pre-oxidized tailings: A numerical hydro-geochemical assessment. Journal of Contaminant Hydrology, **214**: 39–53. Elsevier. doi:10.1016/j.jconhyd.2018.05.006.

Pabst, T., Molson, J., Aubertin, M., and Bussière, B. 2017. Reactive transport modelling of the hydro-geochemical behaviour of partially oxidized acid-generating mine tailings with a monolayer cover. Applied Geochemistry, **78**. doi:10.1016/j.apgeochem.2017.01.003.

Pakostova, E., Schmall, A.J., Holland, S.P., White, H., Ptacek, C.J., and Blowes, D.W. 2020. Performance of a geosynthetic-clay-liner cover system at a Cu/Zn mine tailings impoundment. Applied and Environmental Microbiology, **86**: 1–16. doi:10.1128/AEM.02846-19.

Parkhurst, D.L., and Appelo, C.A.J. 2013. Description of input and examples for PHREEQC version 3: a computer program for speciation, batch-reaction, one-dimensional transport, and inverse geochemical calculations. U.S. Geological Survey Techniques and Methods, 6-A43,: 497. doi:10.3133/tm6A43.

Persoff, P. 2006. Unstable and fingering gas flow in fractures. *In* Gas Transport in Porous Media. *Edited by* C.K. Ho and S.W. Webb. Springer Netherlands. pp. 169–178. doi:10.1007/1-4020-3962-X_9.

Power, C., Hersey, D., and MacPhee, J. 2021. Comparative analysis of defect leakage rates at geomembrane-lined cover systems in the Sydney Coalfield. *In* 28th Annual BC MEND Metal Leaching/Acid Rock Drainage Workshop. Vancouver, BC.

Pyke, D.R. 1982. Geology of the Timmins area, District of Cochrane. Ontario Geological Survey, Report 219,.

Renken, K., Yanful, E.K., and Mchaina, D.M. 2005. Effective oxygen diffusion coefficient and field oxygen concentrations below a geosynthetic clay liner (GCL) covering mine tailings. *In* Geo-Frontiers Congress 2005. doi:https://doi.org/10.1061/40789(168)24.

Renken, K., Yanful, E.K., and Mchaina, D.M. 2005. Field performance evaluation of soil-based cover systems to mitigate ARD for the closure of a potentially acid-generating tailings storage facility. *In* British Columbia Reclamation Symposium. Abbotsford, BC. pp. 19–22.

Ribet, I., Ptacek, C.J., Blowes, D.W., and Jambor, J.L. 1995. The potential for metal release by reductive dissolution of weathered mine tailings. Journal of Contaminant Hydrology, **17**: 239–273. doi:10.1016/0169-7722(94)00010-F.

Rickard, D., and Morse, J.W. 2005. Acid volatile sulfide (AVS). Marine Chemistry, **97**: 141–197. doi:10.1016/j.marchem.2005.08.004.

Rohwerder, T., Gehrke, T., Kinzler, K., and Sand, W. 2003. Bioleaching review part A: Applied Microbiology and Biotechnology, **63**: 239–248. doi:10.1007/s00253-003-1448-7.

Schaap, M.G., Leij, F.J., and van Genuchten, M.Th. 2001. Rosetta: a computer program for estimating soil hydraulic parameters with hierarchical pedotransfer functions. Journal of Hydrology, **251**: 163–176. doi:10.1016/S0022-1694(01)00466-8.

Schmall, A.J. 2020. An Evaluation of a Dry Cover Emplaced on the Northern Impounded Tailings at Kam Kotia Mine, Timmins, Ontario. University of Waterloo.

Seal, R.R. 2006. Sulfur isotope geochemistry of sulfide minerals. Reviews in Mineralogy and Geochemistry, **61**: 633–677. doi:10.2138/rmg.2006.61.12.

SENES Consultants Ltd., Lakefield Research Limited, ESG International Inc., and Denison Environmental Services. 2000. Kam Kotia Mine Property Rehabilitation Study Phase I.

Šimůnek, J., Šejna, M., Saito, H., Sakai, M., and van Genuchten, M.Th. 2013. The Hydrus-1D Software Package for Simulating the Movement of Water, Heat, and Multiple Solutes in Variably Saturated Media, Version 4.17, HYDRUS Software Series 3. Riverside, California, USA.

Smedley, P.L., and Kinniburgh, D.G. 2002. A review of the source, behaviour and distribution of arsenic in natural waters. Applied Geochemistry, **17**. doi:10.1016/S0883-2927(02)00018-5.

Smith, P.G., Koch, I., Gordon, R.A., Mandoli, D.F., Chapman, B.D., and Reimer, K.J. 2005. X-ray absorption near-edge structure analysis of arsenic species for application to biological environmental samples. Environmental Science & Technology, **39**: 248–254. doi:10.1021/es049358b.

Solé, V.A., Papillon, E., Cotte, M., Walter, Ph., and Susini, J. 2007. A multiplatform code for the analysis of energy-dispersive X-ray fluorescence spectra. Spectrochimica Acta Part B: Atomic Spectroscopy, **62**: 63–68. doi:10.1016/j.sab.2006.12.002.

Starr, R.C., and Ingleton, R.A. 1992. A new method for collecting core samples without a drilling rig. Groundwater Monitoring & Remediation, **12**: 91–95. doi:10.1111/j.1745-6592.1992.tb00413.x.

Steefel, C.I., Appelo, C.A.J., Arora, B., Jacques, D., Kalbacher, T., Kolditz, O., Lagneau, V., Lichtner, P.C., Mayer, K.U., Meeussen, J.C.L., Molins, S., Moulton, D., Shao, H., Šimůnek, J., Spycher, N., Yabusaki, S.B., and Yeh, G.T. 2015. Reactive transport codes for subsurface environmental simulation. Computational Geosciences, **19**: 445–478. doi:10.1007/s10596-014-9443-x.

Stormont, J.C., and Anderson, C.E. 1999. Capillary barrier effect from underlying coarser soil layer. Journal of Geotechnical and Geoenvironmental Engineering, **125**: 641–648. doi:10.1061/(ASCE)1090-0241(1999)125:8(641).

Topp, G.C., Davis, J.L., and Annan, A.P. 1980. Electromagnetic determination of soil water content: Measurements in coaxial transmission lines. Water Resources Research, **16**: 574–582. doi:10.1029/WR016i003p00574.

U.S. EPA. 1993. Method 300.0: Determination of Inorganic Anions by Ion Chromatography, Rev. 2.1. Cincinnati, OH.

U.S. EPA. 1994a. Method 200.7: Determination of Metals and Trace Elements in Water and Wastes by Inductively Coupled Plasma-Atomic Emission Spectrometry, Rev. 4.4. *In* 4.4. Cincinnati, OH.

U.S. EPA. 1994b. Method 200.8: Determination of Trace Elements in Waters and Wastes by Inductively Coupled Plasma-Mass Spectrometry, Rev. 5.4. *In* 5.4. Cincinnati, OH.

Wardrop Engineering Inc. 2005. Kam Kotia Mine North Impounded Tailings Composite Soil Cover Design Brief.

Webb, S.W. 2006. Gas transport mechanisms. *In* Gas Transport in Porous Media. *Edited by* C.K. Ho and S.W. Webb. Springer Netherlands. pp. 5–26. doi:10.1007/1-4020-3962-X_2.

Wilson, D., Amos, R.T., Blowes, D.W., Langman, J.B., Ptacek, C.J., Smith, L., and Sego, D.C. 2018a. Diavik waste rock project: A conceptual model for temperature and sulfide-

content dependent geochemical evolution of waste rock – Laboratory scale. Applied Geochemistry, **89**: 160–172. doi:10.1016/j.apgeochem.2017.12.007.

Wilson, D., Amos, R.T., Blowes, D.W., Langman, J.B., Smith, L., and Sego, D.C. 2018b. Diavik Waste Rock Project: Scale-up of a reactive transport model for temperature and sulfide-content dependent geochemical evolution of waste rock. Applied Geochemistry, **96**. doi:10.1016/j.apgeochem.2018.07.001.

Winterhalder, K. 1992. The experimental use of various covers and native transplants for the revegetation of the Kam-Kotia tailings site, Timmins, Ontario. *In* Achieving Land Use Potential through Reclamation: Proceedings of the 9th Annual National Meeting. *Edited by* D. Jordan. American Society for Surface Mining and Reclamation, Duluth, Minnesota. pp. 385–396. doi:10.21000/jasmr92010385.

Wunderly, M.D., Blowes, D.W., Frind, E.O., and Ptacek, C.J. 1996. Sulfide mineral oxidation and subsequent reactive transport of oxidation products in mine tailings impoundments: A numerical model. Water Resources Research, **32**: 3173–3187. doi:10.1029/96WR02105.

Yin, G., and Catalan, L.J.J. 2003. Use of alkaline extraction to quantify sulfate concentration in oxidized mine tailings. Journal of Environmental Quality, **32**: 2410–2413. doi:10.2134/jeq2003.2410.

Appendix A

Penman-Monteith calculations

The following calculations are adopted from FAO-56 (Allen et al. 1998). Daily reference evapotranspiration (ET_0) in mm d^{-1} can be calculated as:

$$ET_0 = \frac{0.408\Delta(R_n - G) + \gamma \frac{900}{T + 273} u_2 (e_s - e_a)}{\Delta + \gamma(1 + 0.34u_2)}$$

T is daily mean air temperature (°C)

u_2 is wind speed at 2 m above the ground (m s^{-1}), which can be converted from wind speed measured at another elevation (u_z) by:

$$u_2 = u_z \frac{4.87}{\ln(67.8z - 5.42)}$$

- where z is wind speed measurement elevation above ground (m)

G is soil heat flux density (MJ m^{-2} h^{-1}):

$$G = c_s \frac{T_i - T_{i-1}}{\Delta t} \Delta z$$

- c_s is soil heat capacity (MJ m^{-3} °C^{-1})
- T_i is air temperature at time i (°C)
- T_{i-1} is air temperature at time i-1 (°C)
- Δt is length of time interval (day)
- Δz is effective soil depth (m)
- For daily calculations, it can be assumed that G=0

e_s is saturation vapour pressure (kPa):

$$e_s = \frac{e^o(T_{max}) + e^o(T_{min})}{2}$$

- T_{max} is daily maximum air temperature
- T_{min} is daily minimum air temperature

- vapour pressure at a temperature T ($e^0(T)$) is:

$$e^o(T) = 0.6108\exp\left(\frac{17.27T}{T+237.3}\right)$$

e_a is actual vapour pressure (kPa):

$$e_a = \frac{RH_{mean}}{100}\left(\frac{e^o(T_{max}) + e^o(T_{min})}{2}\right) = e_s\frac{RH_{mean}}{100}$$

- RH_{mean} is daily average relative humidity (%)

Δ is the slope of the vapour pressure vs temp curve (kPa °C^{-1}):

$$\Delta = \frac{4098\left[0.6108\exp\left(\frac{17.27\,T}{T+237.3}\right)\right]}{(T+237.3)^2}$$

γ is psychrometric constant:

$$\gamma = \frac{c_p P}{\varepsilon\lambda} = 0.665\times10^{-3}P$$

- where P is atmospheric pressure (kPa):

$$P = 101.3\left(\frac{293-0.0065z}{293}\right)^{5.26}$$

  - z is elevation of the location above sea level (m)

R_n is net radiation (MJ m^{-2} d^{-1}):

$$R_n = R_{ns} - R_{nl}$$

R_{ns} is net solar or net shortwave radiation (MJ m^{-2} d^{-1}):

$$R_{ns} = R_s(1-\alpha)$$

- α is albedo (0.23 for grass reference crop)

R_{nl} is net longwave radiation (MJ m^{-2} d^{-1}):

$$R_{nl} = \sigma\left(\frac{{T_{max,K}}^4 + {T_{min,K}}^4}{2}\right)(0.34-0.14\sqrt{e_a})\left(1.35\frac{R_s}{R_{so}}-0.35\right)$$

- σ is Stefan-Boltzmann constant = 4.903E^{-9} MJ K^{-4} m^{-2} day^{-1}

- $T_{max,K}$ is maximum absolute temperature during the 24-hour period (K = °C + 273.16)
- $T_{min,K}$ is minimum absolute temperature during the 24-hour period
- e_a is actual vapour pressure (kPa)
- R_s/R_{so} <= 1.0

R_s is solar radiation (MJ m^{-2} d^{-1}):

$$R_s = \left(a_s + b_s \frac{n}{N}\right) R_a$$

- a_s = 0.25
- b_s = 0.50
- n is actual duration of sunshine (hour)
- N is daylight hours (hour):

$$N = \frac{24}{\pi} \omega_s$$

- In the absence of n, R_s can be estimated with Hargreaves' radiation formula:

$$R_s = k_{Rs} \sqrt{T_{max} - T_{min}} R_a$$

- k_{Rs} is adjustment coefficient between 0.16 and 0.19 (°$C^{-0.5}$). k_{Rs} ≈ 0.16 for inland

R_{so} is clear-sky solar radiation (MJ m^{-2} d^{-1}):

$$R_{so} = (0.75 + 2 \times 10^{-5} z) R_a$$

- z is station elevation above sea level [m]
- R_a is extraterrestrial radiation (MJ m^{-2} d^{-1}) and can be estimated as:

$$R_a = \frac{24(60)}{\pi} G_{SC} d_r (\omega_s \sin(\varphi) \sin(\delta) + \cos(\varphi) \cos(\delta) \sin(\omega_s))$$

  - G_{sc} is solar constant = 0.0820 MJ m^{-2} min^{-1}
  - d_r is inverse relative distance between the Earth and the Sun (-):

$$d_r = 1 + 0.033 \cos\left(\frac{2\pi}{365} J\right)$$

- J is the number of the day in the year between 1 (1 January) and 365 or 366 (31 December)
- ω_s is sunset hour angle (rad):

$$\omega_s = \arccos(-\tan(\varphi)\tan(\delta))$$

  - φ is latitude (rad):

$$radians = \frac{\pi}{180} degrees$$

  - δ is solar declination (rad):

$$\delta = 0.409 \sin\left(\frac{2\pi}{360} J - 1.39\right)$$

Since evapotranspiration under a snow cover is extremely small, reference evapotranspiration rate ET_0 is modified using a frozen ground coefficient (K_f). If the weather station records a positive value for snow on ground. K_f is determined to be 0. If no value is recorded, daily mean temperature is used to determine if K_f is 0 or 1:

$$K_f = \begin{cases} 0, snow\ on\ ground > 0 \\ \begin{cases} 1, T_{mean} > 0 \\ 0, T_{mean} \leq 0 \end{cases} \end{cases}$$

Actual evapotranspiration (ET) is calculated as:

$$ET = K_f \times ET_0$$

Appendix B

Additional groundwater elevation contour maps

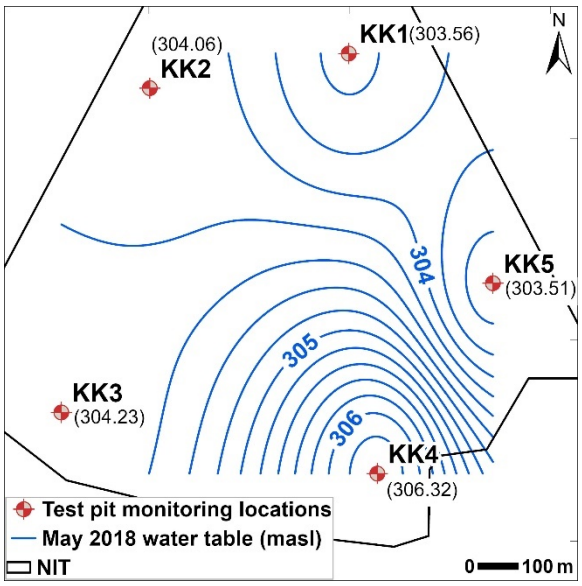

Figure S-B1. May 2018 perched water-table elevation contours above the clay layer. A contour interval of 0.2 m was used.

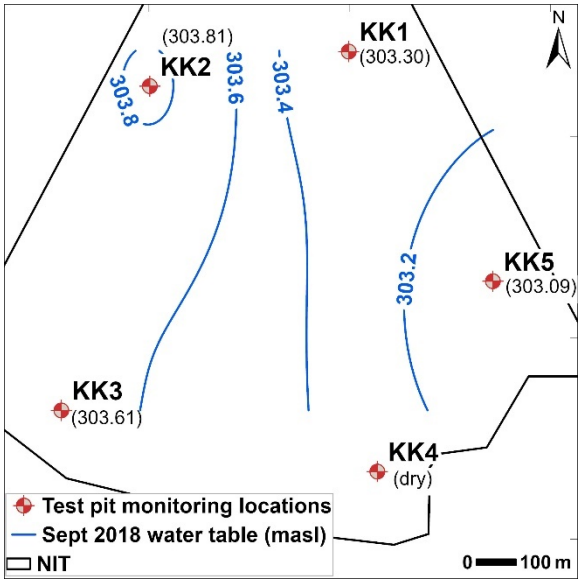

Figure S-B2. September 2018 water-table elevation contours in the tailings and sand aquifer at NIT. A contour interval of 0.2 m was used.

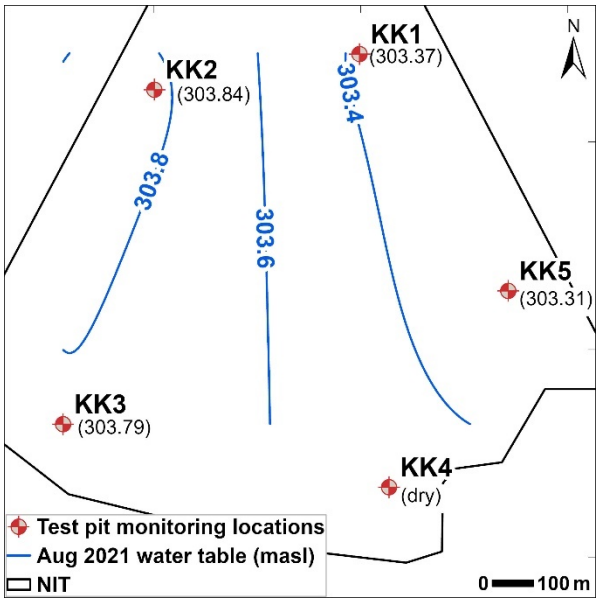

Figure S-B3. August 2021 water-table elevation contours in the tailings and sand aquifer at NIT. A contour interval of 0.2 m was used.

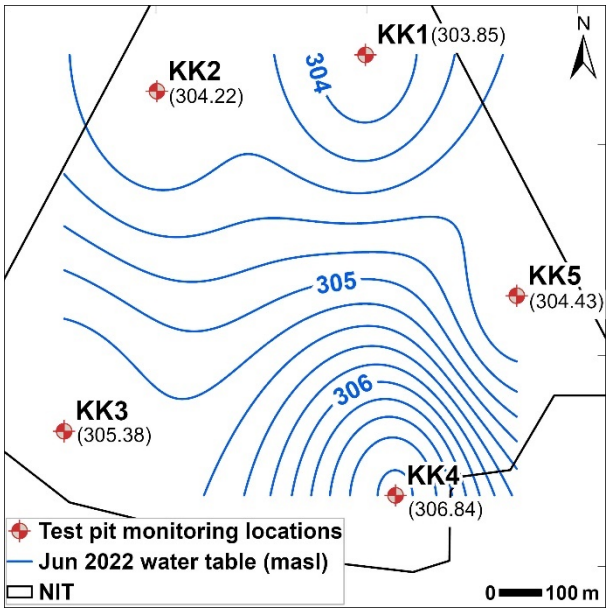

Figure S-B4. June 2022 water-table elevation contours in the tailings and sand aquifer at NIT. A contour interval of 0.2 m was used.

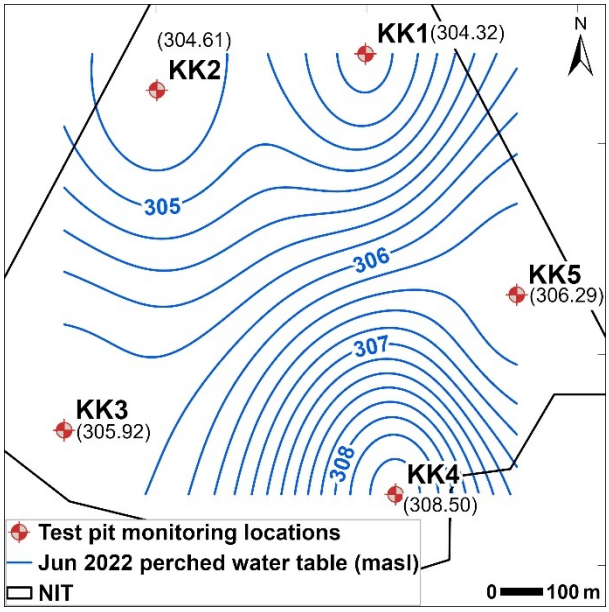

Figure S-B5. June 2022 perched water-table elevation contours above the clay layer. A contour interval of 0.2 m was used.

Appendix C

Additional *in situ* instrumentation data

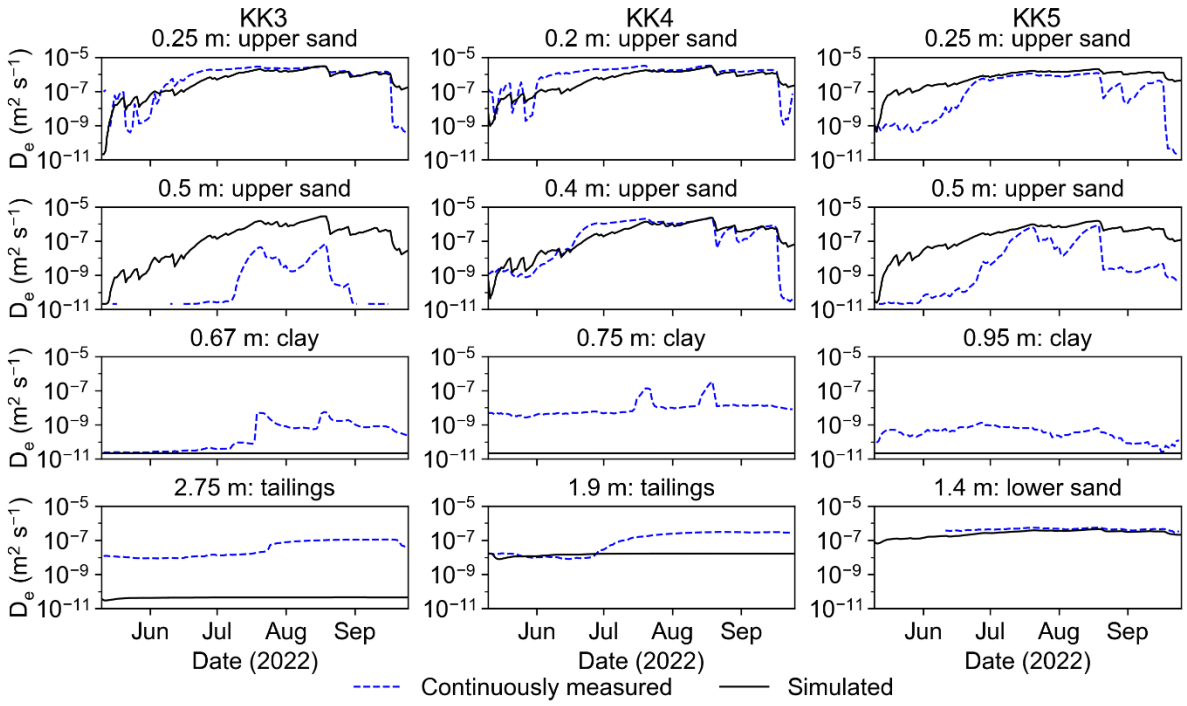

Figure S-C1. Time series of effective O_2 diffusion coefficient (D_e) between May 10th and September 25th, 2022, calculated from *in situ* continuously measured soil moisture content (θ_w) and Hydrus 1-D simulated θ_w.

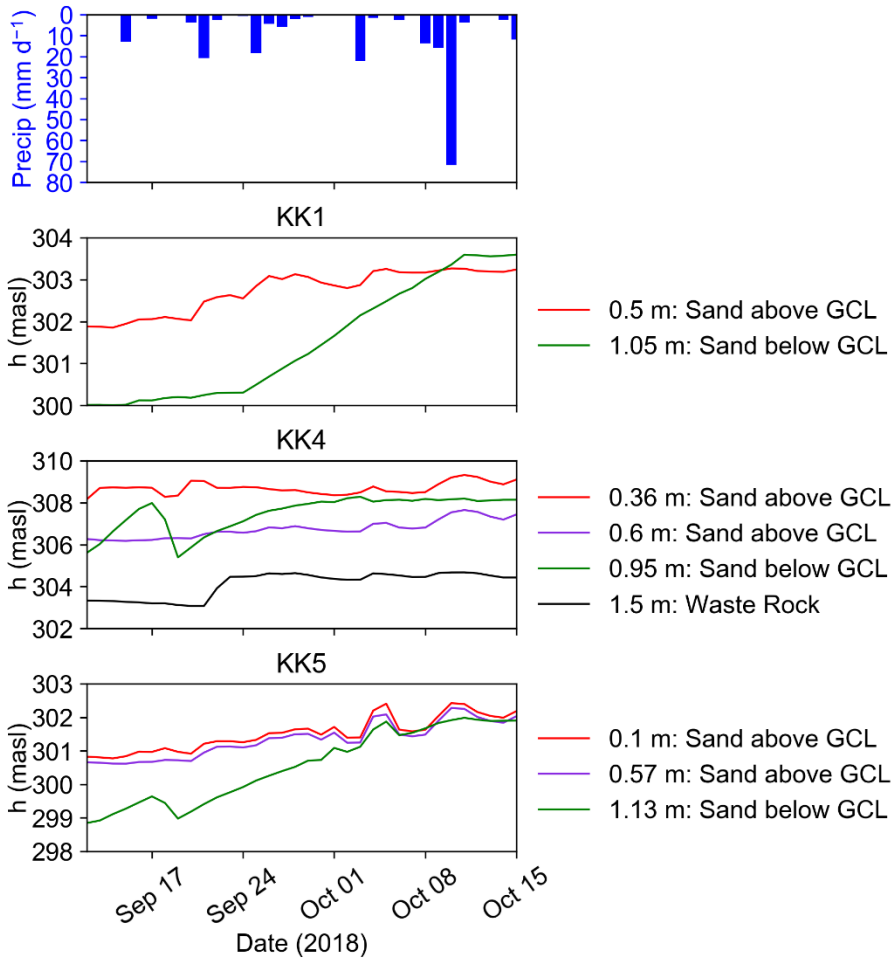

Figure S-C2. Time series of daily average hydraulic head (h) in meters above sea level (masl) calculated from matric suction recorded by tensiometers at three test pit locations in 2018.

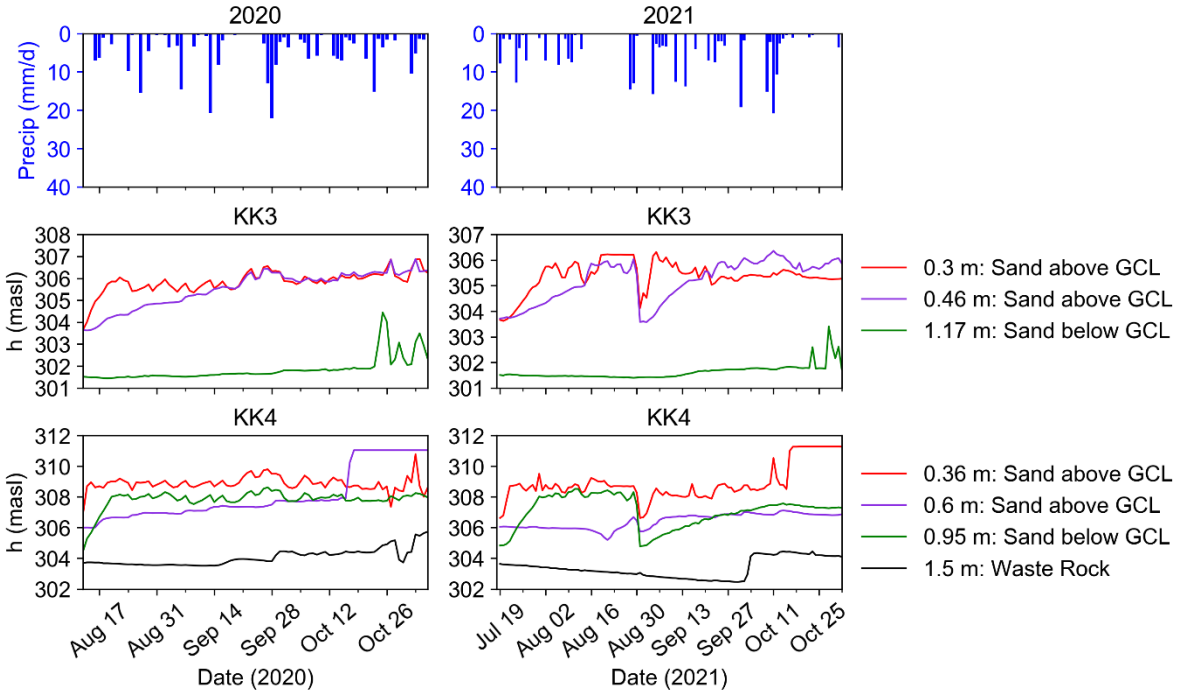

Figure S-C3. Time series of daily average hydraulic head (h) in meters above sea level (masl) calculated from matric suction recorded by tensiometers at three test pit locations in 2020 and 2021.

Appendix D

Additional mineralogical data, photomicrographs, BSE images, and SEM/EDX analysis results

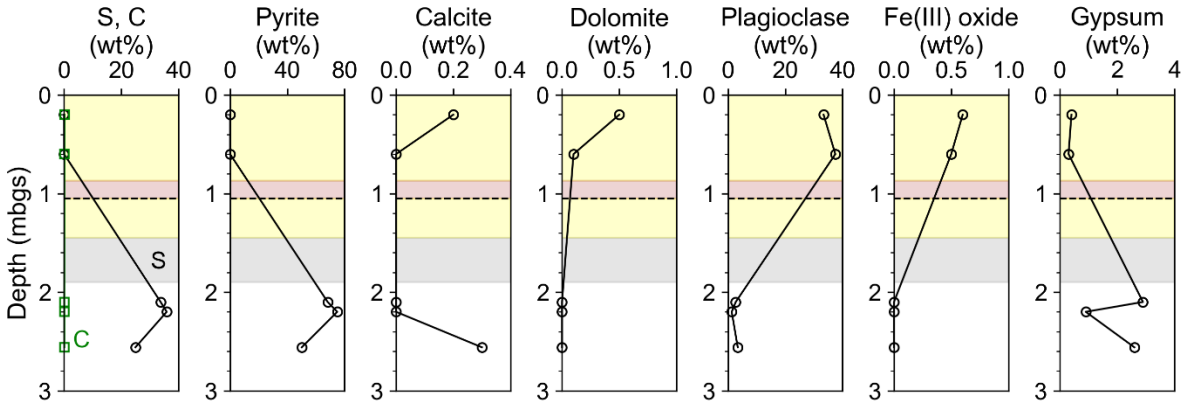

Figure S-D1. Depth profiles of C/S concentrations and major crystalline phases identified by X-ray diffraction (XRD) analysis conducted by Schmall (2020) at KK5.

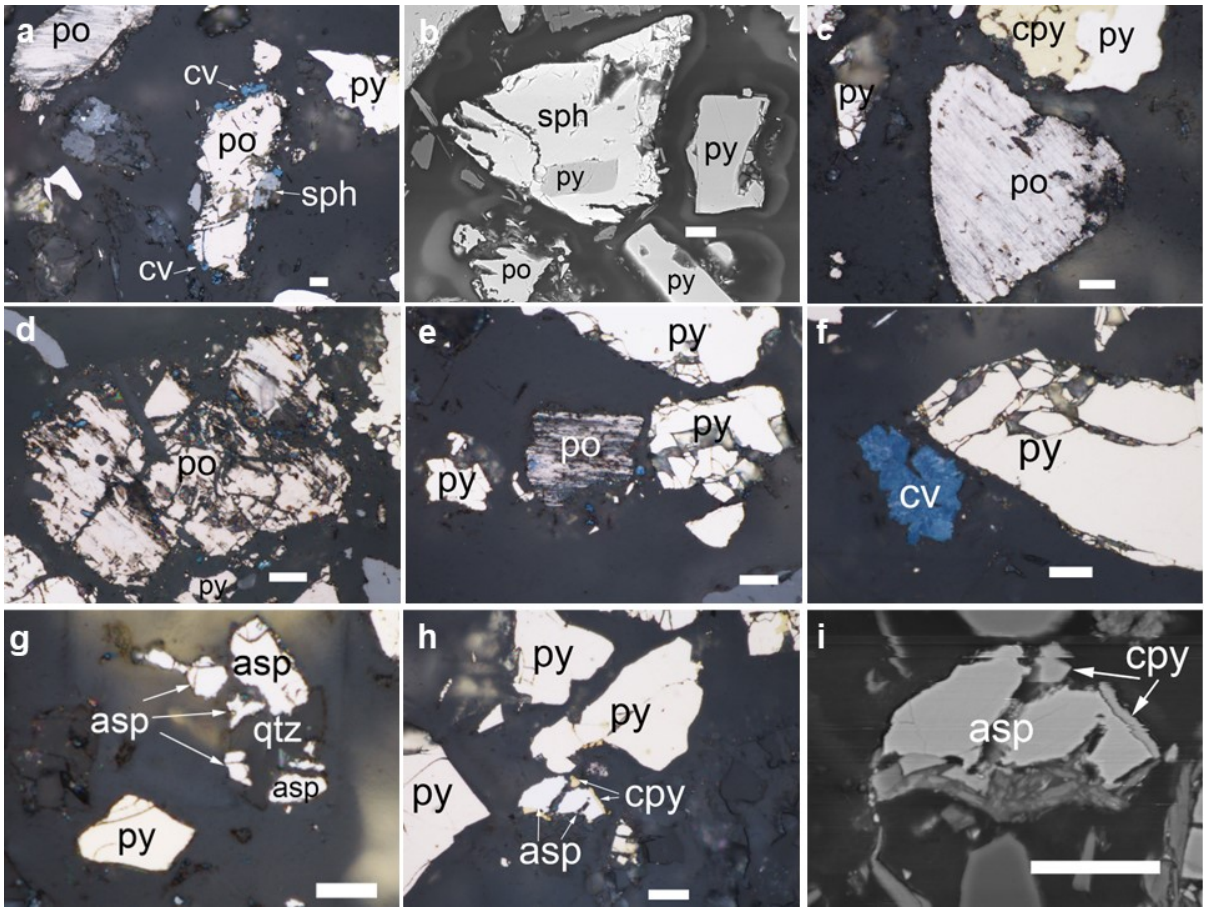

Figure S-D2. Photomicrographs under plain reflected light (a, c-h) and SEM backscattered electron (BSE) images (b, i) of polished grain-mounted thin section of KK4 tailings at 2.45 meters below ground surface (mbgs). Po=pyrrhotite, py=pyrite, cv=covellite, sph=sphalerite, cpy=chalcopyrite, asp=arsenopyrite, and qtz=quartz. (a) Centre: pyrrhotite grain with alteration along fracture, intergrown sphalerite, and small covellite grains around; upper left: pyrrhotite with alteration along parting (b) Unaltered sphalerite grain with pyrite inclusion; pyrrhotite showing alteration to Fe oxyhydroxides along the rim and fractures. (c) Centre: pyrrhotite grain with alteration along basal parting; upper: unaltered intergrown pyrite and chalcopyrite (d) Pyrrhotite altered to oxyhydroxides along fractures, rim, and parting. (e) Pyrrhotite with intensive alteration to marcasite and Fe oxyhydroxides, surrounded by unaltered pyrite grains (f) Covellite on pseudomorph after pyrrhotite, next to unaltered pyrite. (g) Unaltered arsenopyrite in quartz matrix. (h), (i) Arsenopyrite with rim of Fe oxyhydroxides at the bottom and small intergrown chalcopyrite.

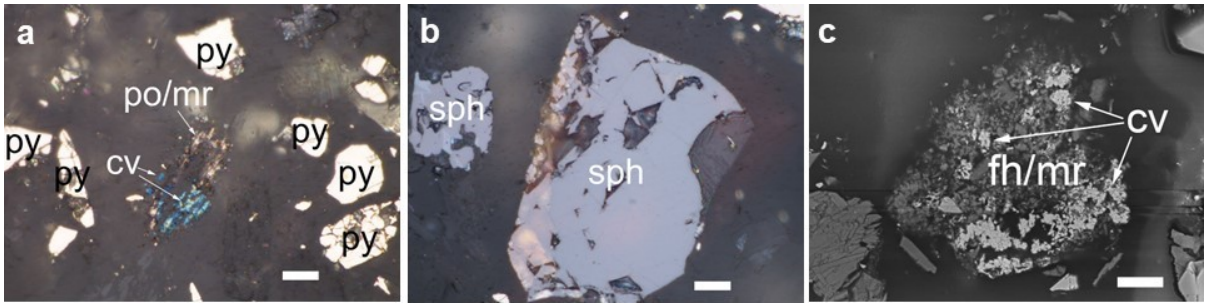

Figure S-D3. Photomicrographs under plain reflected light (a, b) and BSE images (c) of polished grain-mounted thin section of KK4 tailings at 2.2 meters below ground surface (mbgs). Each white scale bar represents 10 μm. Fh=ferrihydrite, mr=marcasite. (a) Marcasite and Fe oxyhydroxide pseudomorph after pyrrhotite with covellite precipitated on top. (b) Unaltered sphalerite. (c) Another marcasite and Fe oxyhydroxide pseudomorph after pyrrhotite with covellite precipitated on top.

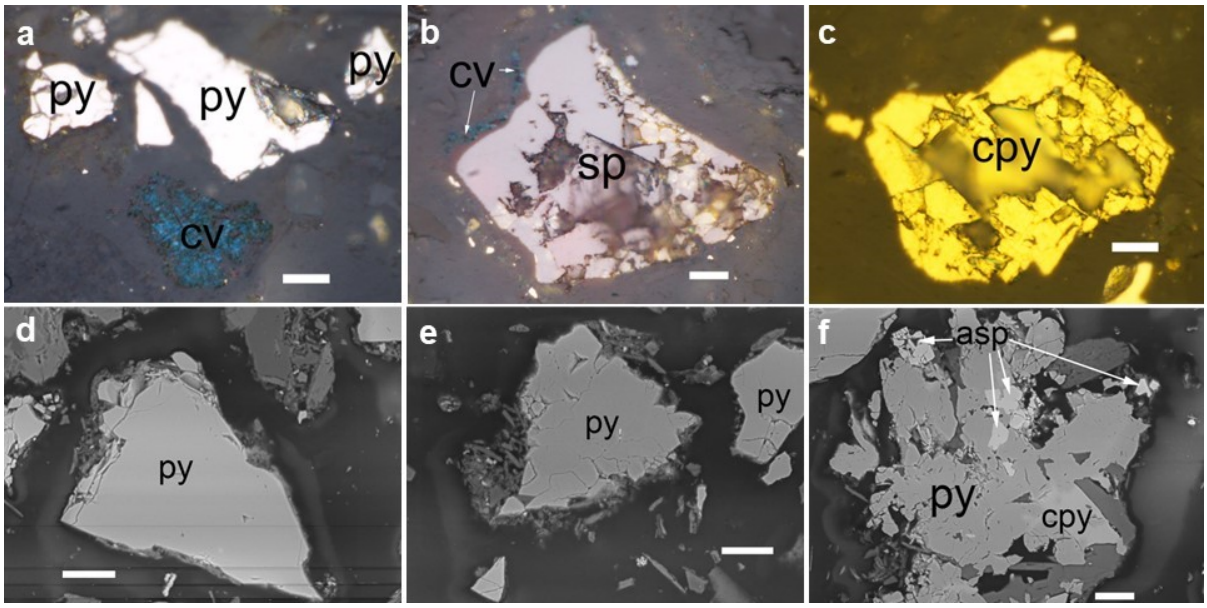

Figure S-D4. Photomicrographs under plain reflected light (a-c) and BSE images (d-f) of polished grain-mounted thin section of KK4 tailings at 2.0 meters below ground surface (mbgs). Each white scale bar represents 10 μm. (a) Unaltered pyrite grains and covellite

precipitated on former pyrrhotite grain. (b) Unaltered sphalerite grain surrounded by covellite. (c) unaltered chalcopyrite. (d) pyrite at the early stage of oxidation along the rim and outer fractures; thin rim of oxyhydroxides along the bottom and left rim. (e) Left: pyrite displaying oxidation with rim of Fe oxyhydroxides and hydroxysulfates; right: pyrite without alteration. (f) Arsenopyrite and chalcopyrite inclusions within pyrite.

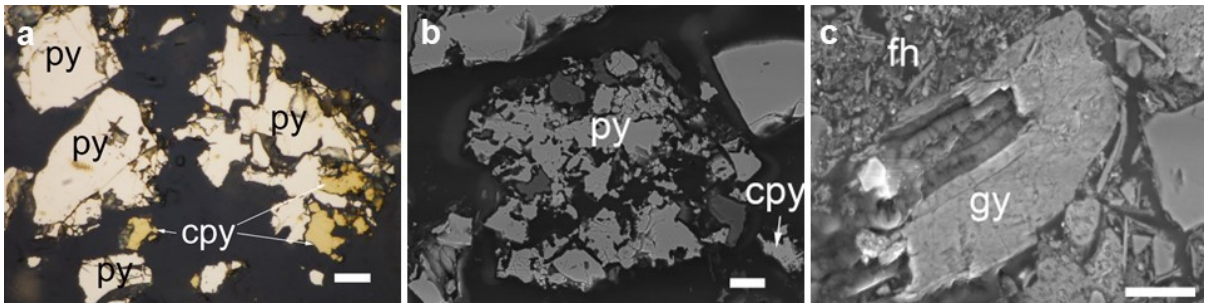

Figure S-D5. Photomicrographs under plain reflected light (a) and BSE images (b, c) of polished grain-mounted thin section of KK4 tailings at 1.8 meters below ground surface (mbgs). Each white scale bar represents 10 μm. Gy=gypsum. (a) Pyrite and chalcopyrite displaying congruent dissolution along fractures and rim. Sulfides were broken into smaller pieces without alteration rim. (b) Pyrite and chalcopyrite with congruent dissolution; Fe oxyhydroxide (dark grey) pseudomorphs in place of former sulfide (c) Gypsum surround by Fe oxyhydroxides.

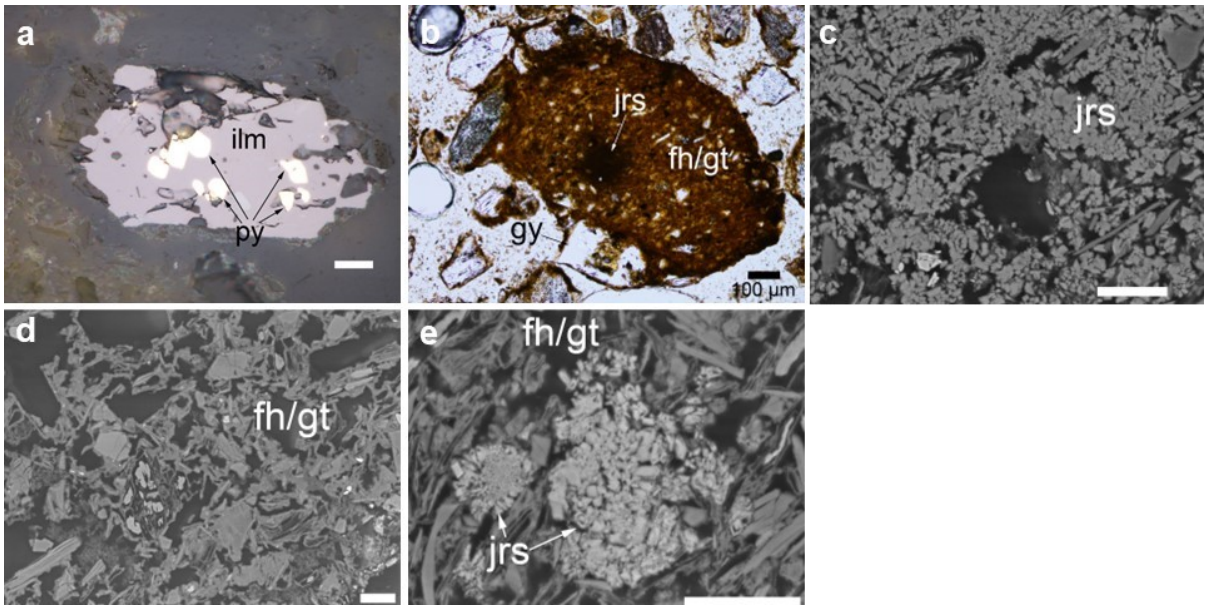

Figure S-D6. Photomicrographs under plain reflected light (a), transmitted light (b) and BSE images (c-e) of polished grain-mounted thin section of KK4 tailings at 1.65 meters below ground surface (mbgs) characterized by thin hardpan. Each white scale bar represents 10 µm. Ilm= ilmenite, jrs=jarosite, gt=goethite, gy=gypsum. (a) Remnant pyrite inclusions in ilmenite; no individual sulfide grains were present at this depth. (b) Jarosite at the centre of large ferrihydrite/goethite precipitate. Black scale bar represents 100 µm. (c) Zoomed in view of jarosite cluster in (b); void were likely casts of microbes. (d) ferrihydrite and goethite. (d) Another jarosite cluster surrounded by ferrihydrite/goethite.

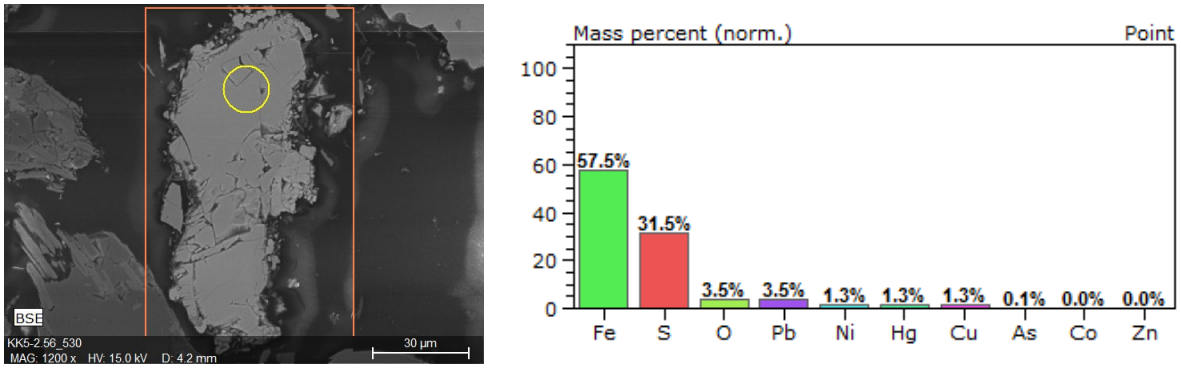

Figure S-D7. EDX spot analysis of elemental concentrations (in weight %) at an unoxidized pyrrhotite grain at 2.45 meters below ground surface (mbgs) of KK4.

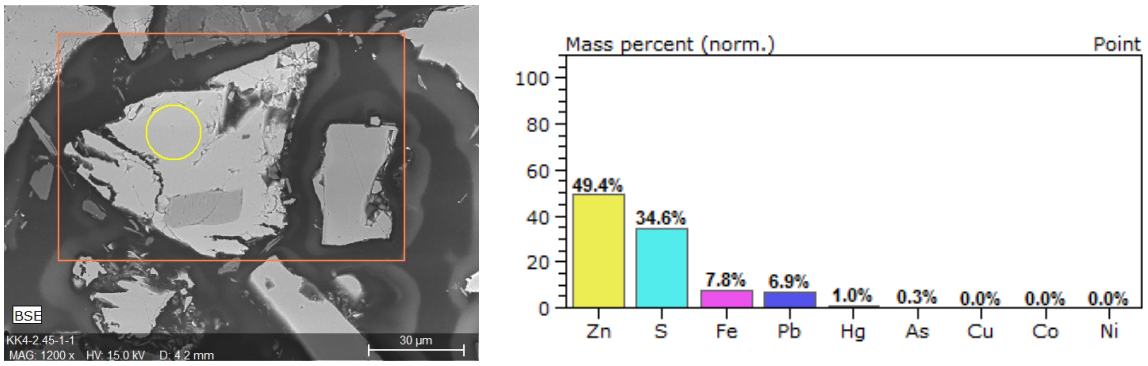

Figure S-D8. EDX spot analysis of elemental concentrations (in weight %) at an unoxidized sphalerite grain at 2.45 meters below ground surface (mbgs) of KK4.

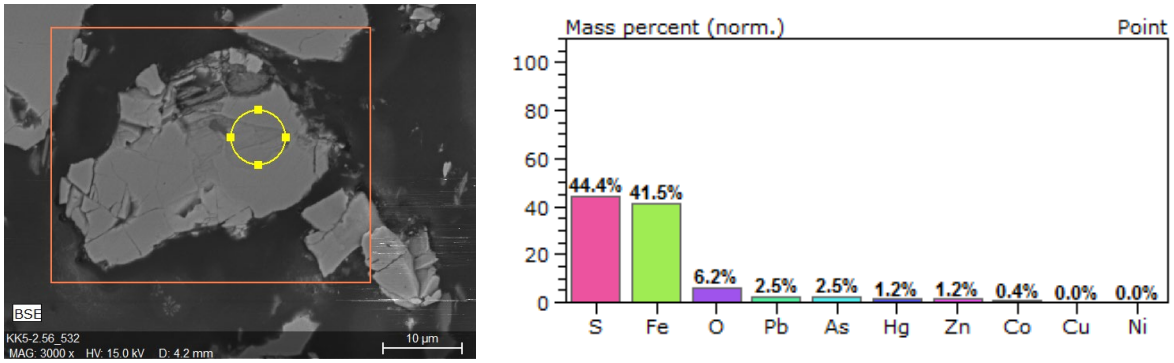

Figure S-D9. EDX spot analysis of elemental concentrations (in weight %) at an unoxidized pyrite grain at 2.45 meters below ground surface (mbgs) of KK4.

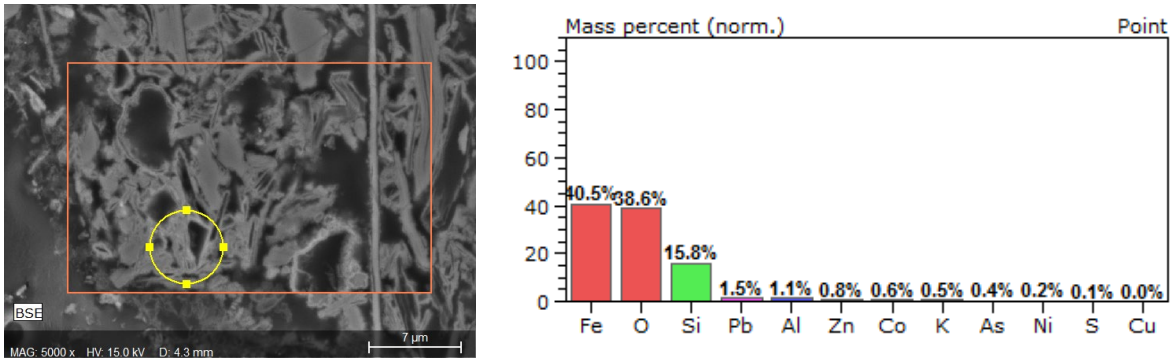

Figure S-D10. EDX spot analysis of elemental concentrations (in weight %) at Fe oxide at 1.65 mbgs of KK4.

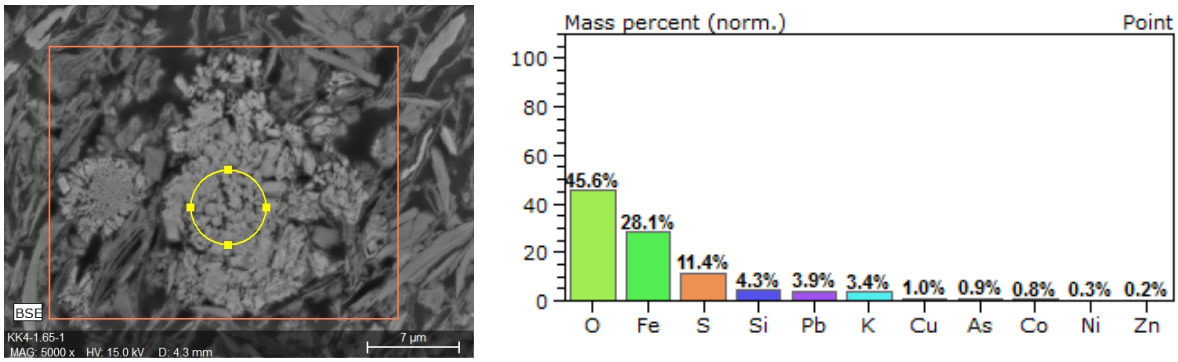

Figure S-D11. EDX spot analysis of elemental concentrations (in weight %) at jarosite at 1.65 mbgs of KK4.

Appendix E

Additional pore-water and selective chemical extraction data

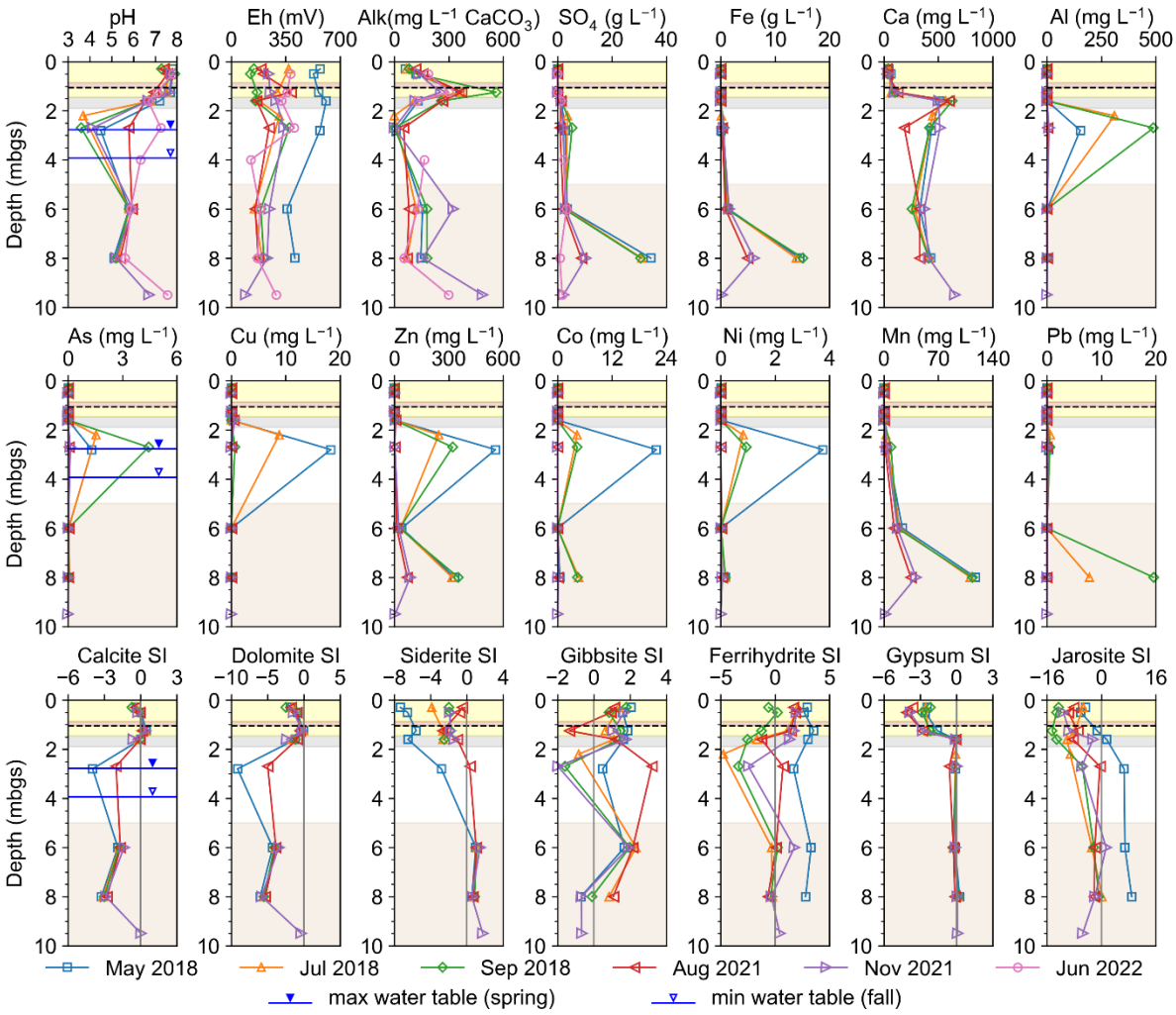

Figure S-E1. Vertical profiles of aqueous geochemical results and calculated SI at KK5 from six pore-water and groundwater sampling events. Background colours represent different layers: yellow for sand, brown for clay, black dashed line for GCL, grey for waste rock, white for tailings, green for peat, and tan for quaternary sand.

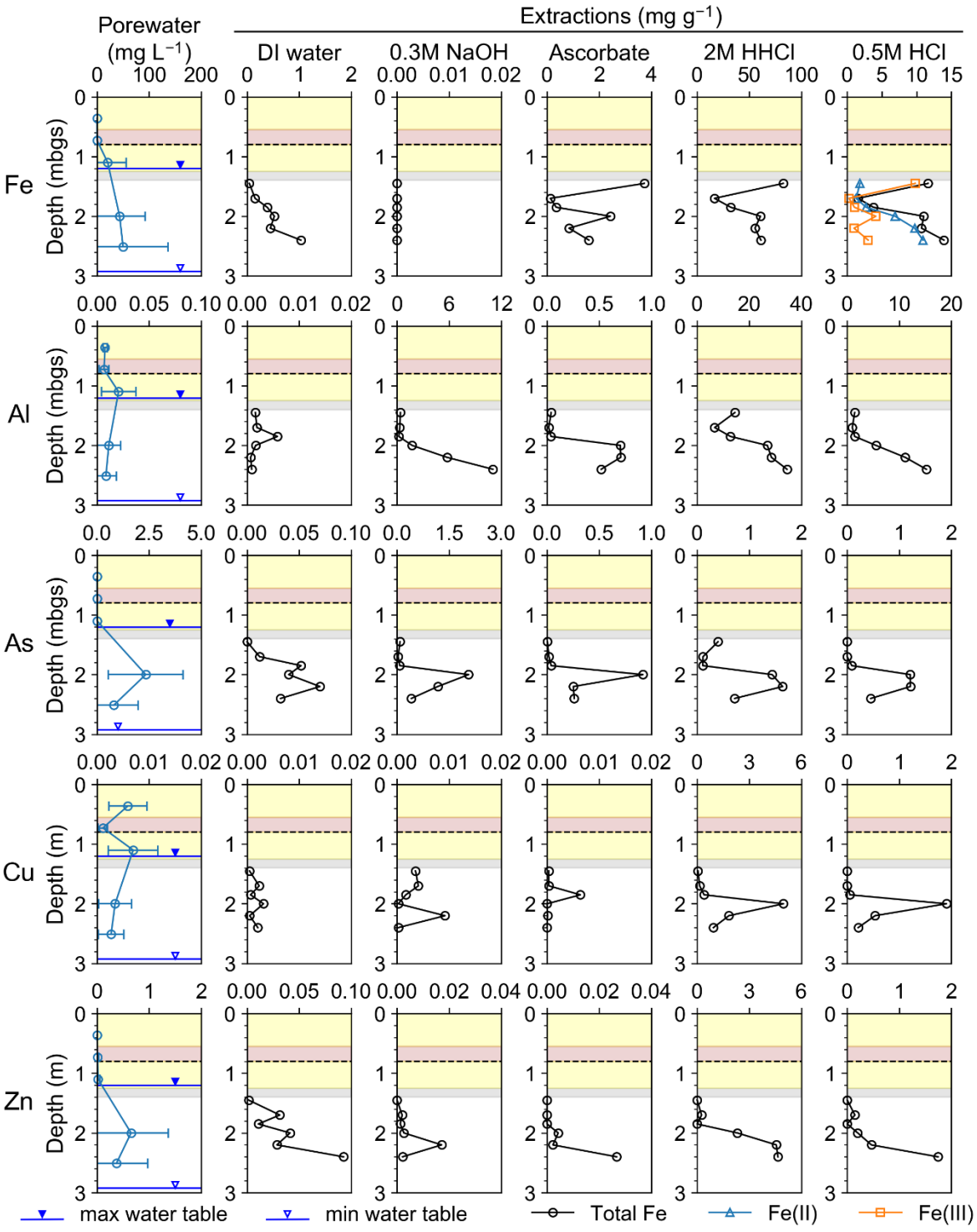
Porewater
(mg L^{-1})
Extractions (mg g^{-1})
DI water
0.3M NaOH
Ascorbate
2M HHCl
0.5M HCl
Fe
Al
As
Cu
Zn
Depth (mbgs)
Depth (m)
max water table
min water table
Total Fe
Fe(II)
Fe(III)

Figure S-E2. Selectively extracted Fe, Al, As, Cu, and Zn concentrations compared to average and standard deviation of aqueous concentrations at KK3.

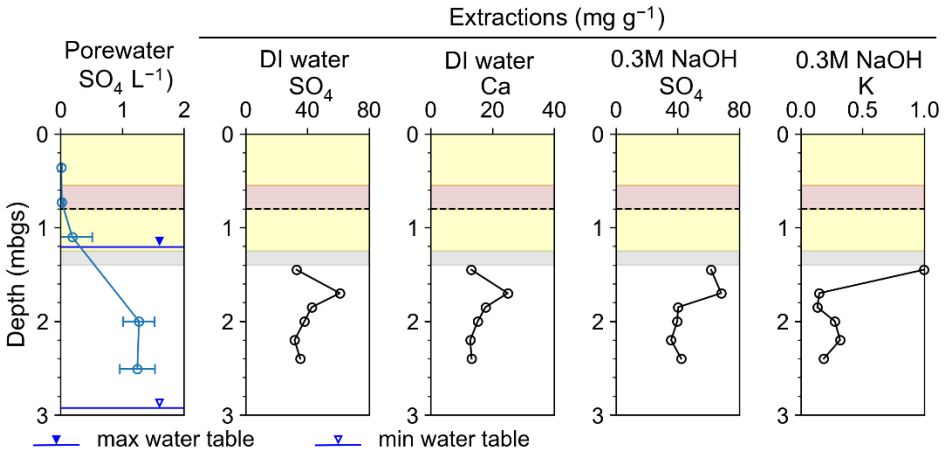

Figure S-E3. Selectively extracted SO_4, Ca, and K concentrations compared to average and standard deviation of aqueous concentrations at KK3.

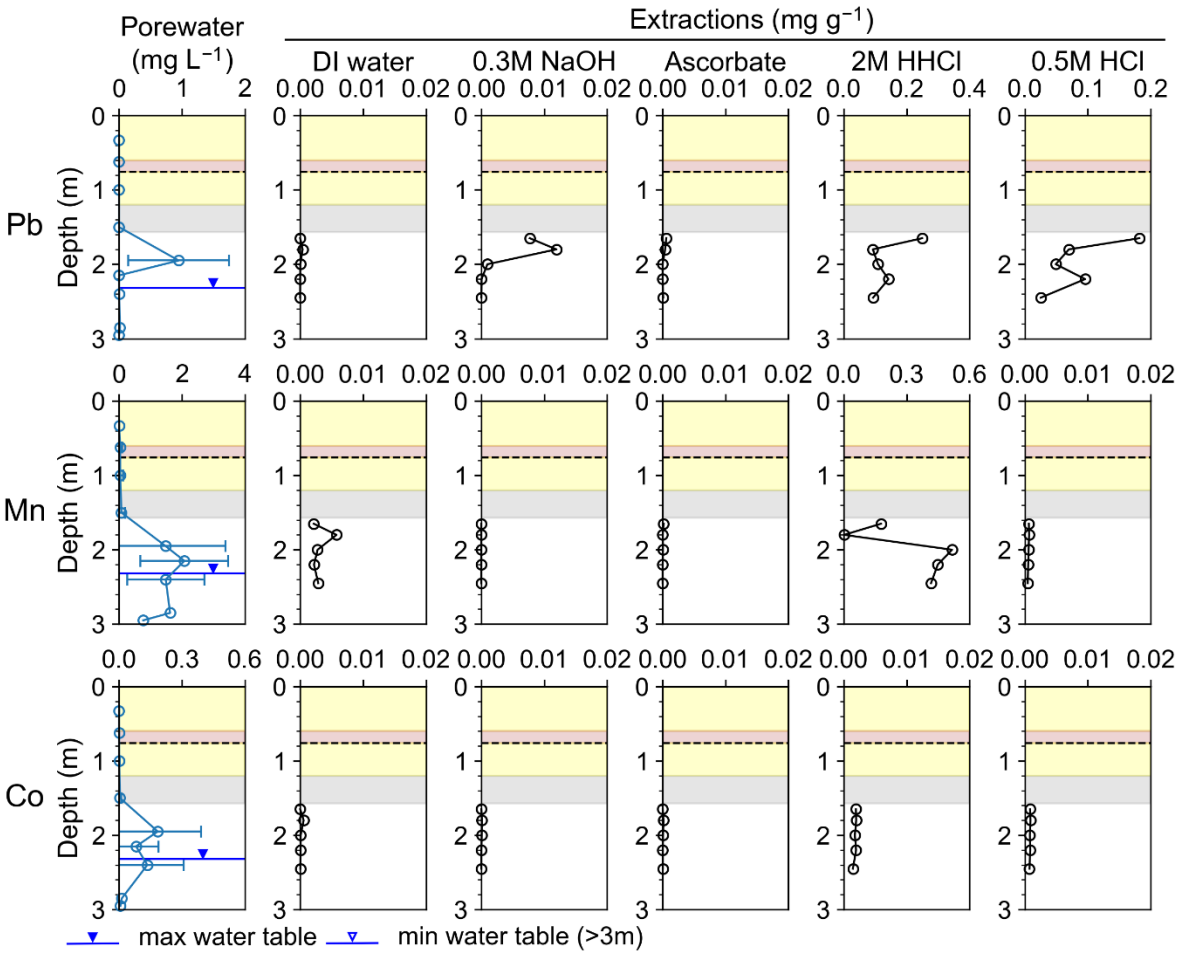

Figure S-E4. Selectively extracted Pb, Mn, and Co concentrations compared to average and standard deviation of aqueous concentrations at KK4.

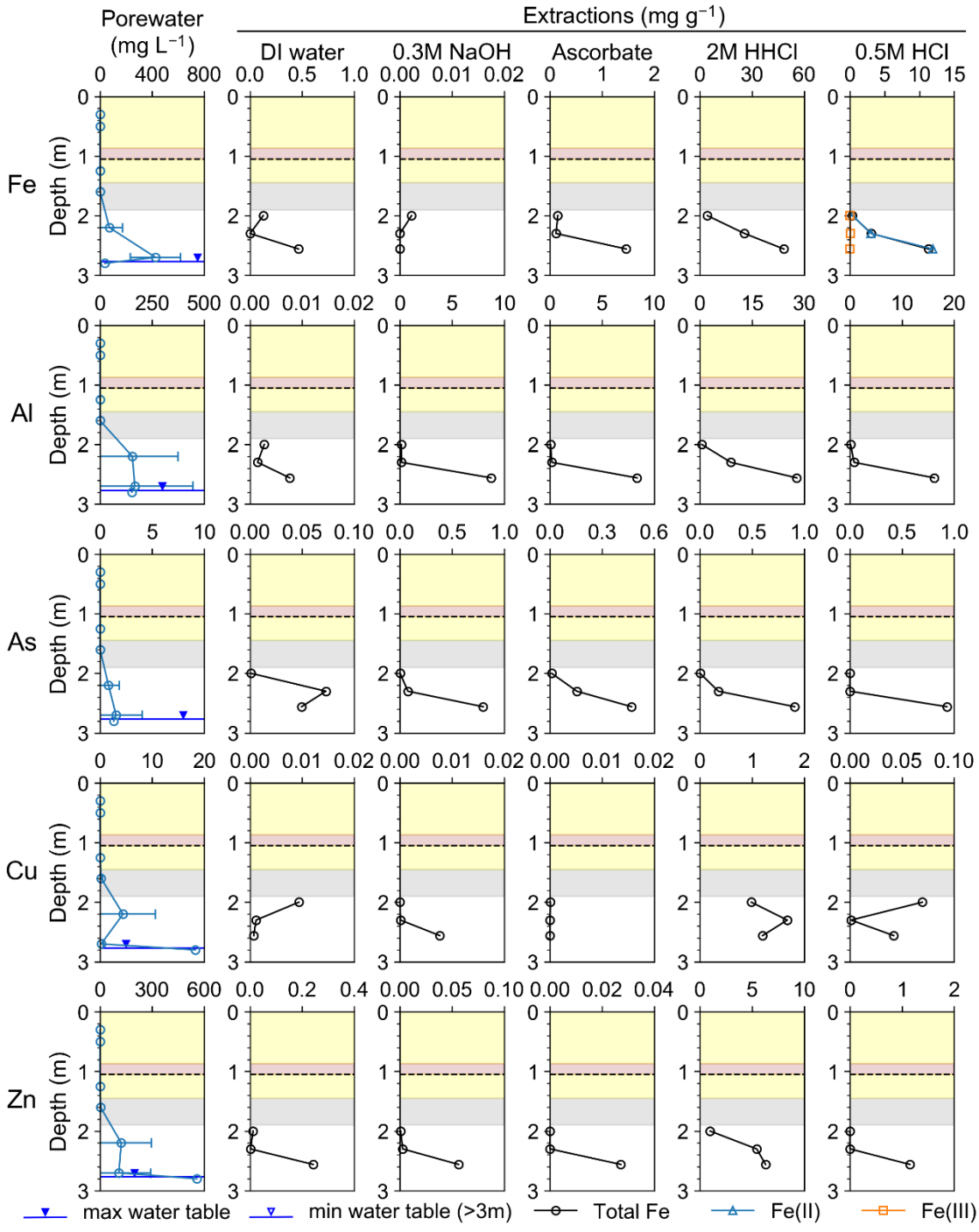

Figure S-E5. Selectively extracted Fe, Al, As, Cu, and Zn concentrations compared to average and standard deviation of aqueous concentrations at KK5.

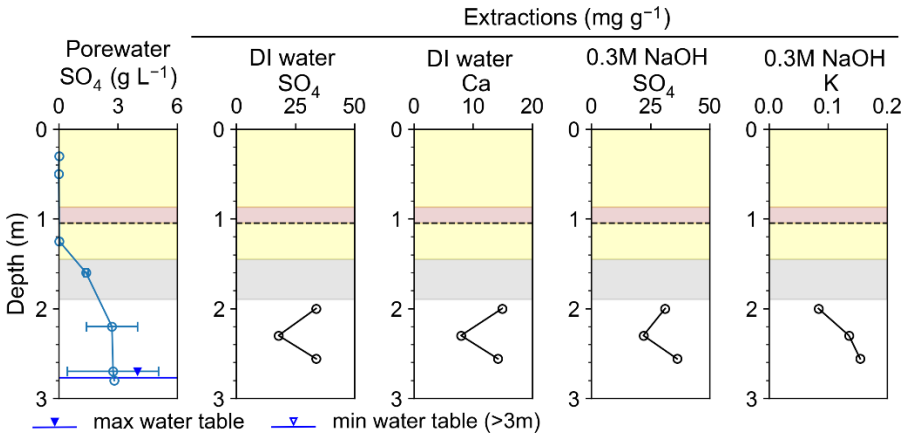

Figure S-E6. Selectively extracted SO_4, Ca, and K concentrations compared to average and standard deviation of aqueous concentrations at KK5.

Appendix F

Additional synchrotron-based X-ray absorption spectroscopy data

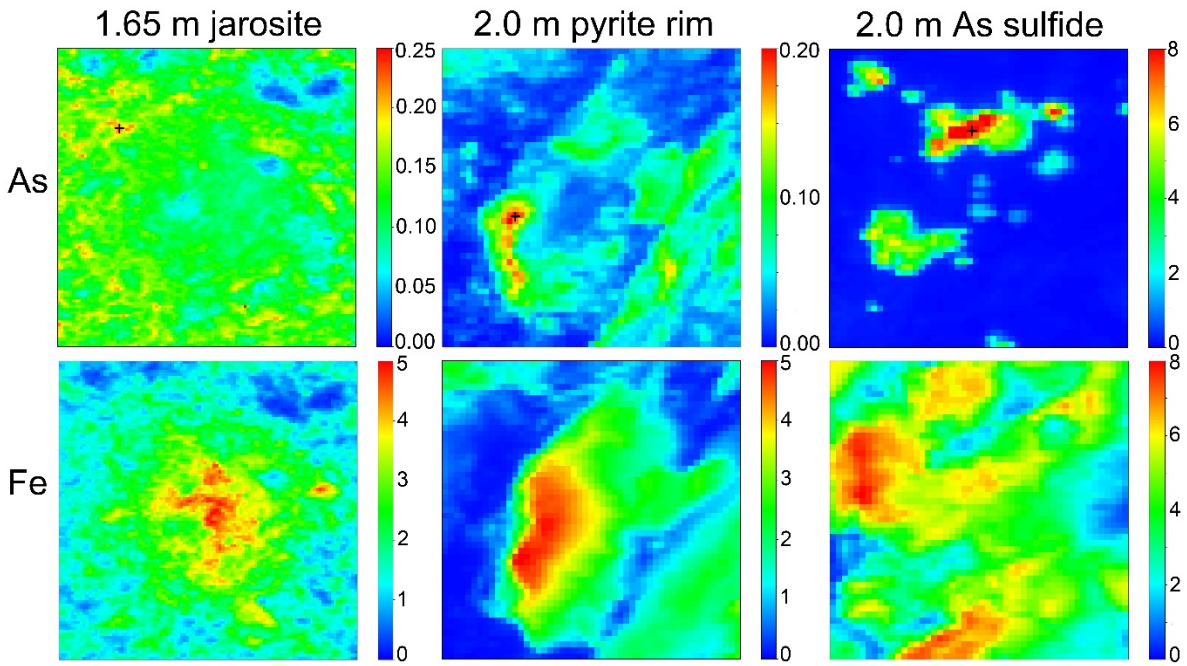

Figure S-F1. Arsenic and Fe μXRF maps of normalized relative intensity at three different grains at KK4: 1.65 m (oxidized zone, hardpan) and 2.0 m (transition zone between oxidized and reduced environment). Black crosses mark the locations of As μXANES measurements.

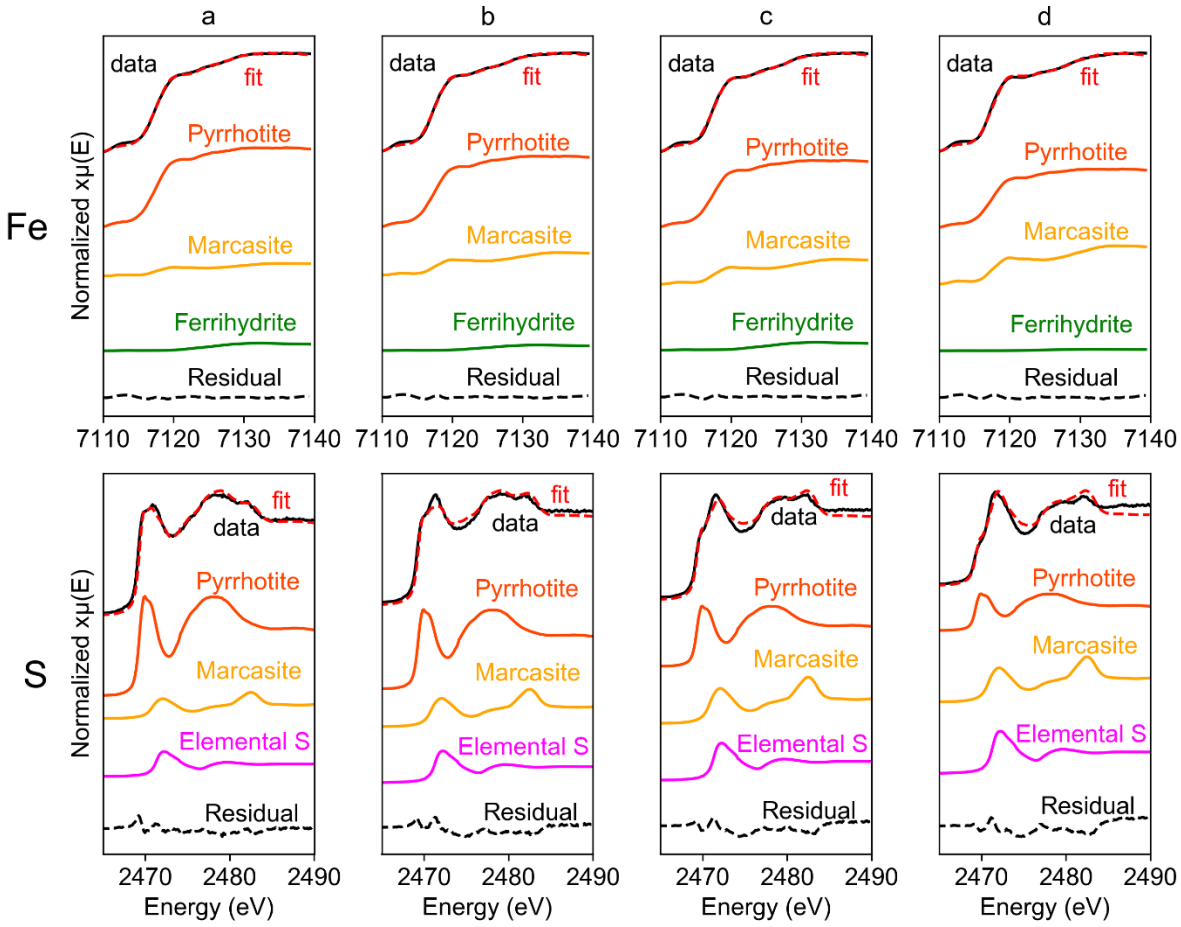

Figure S-F2. Iron and S μXANES raw linear combination fitting at four spots across a pyrrhotite grain at 2.45 mbgs of KK4.

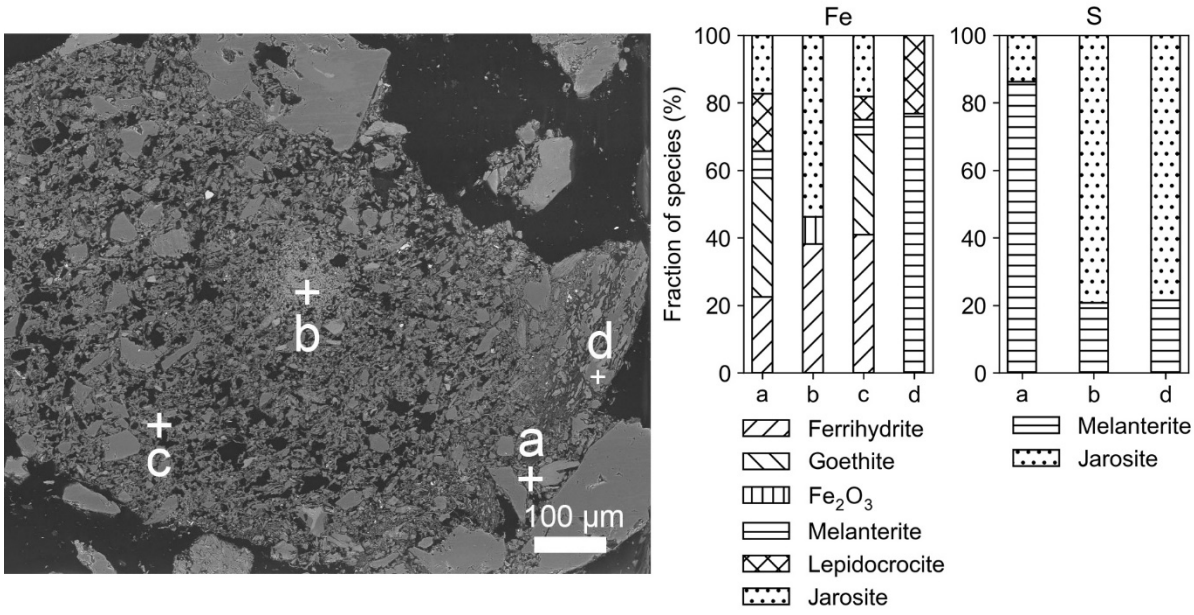

Figure S-F3. Iron and S µXANES linear combination fitting results at four spots across Fe(III) oxyhydroxide at 1.65 mbgs of KK4.

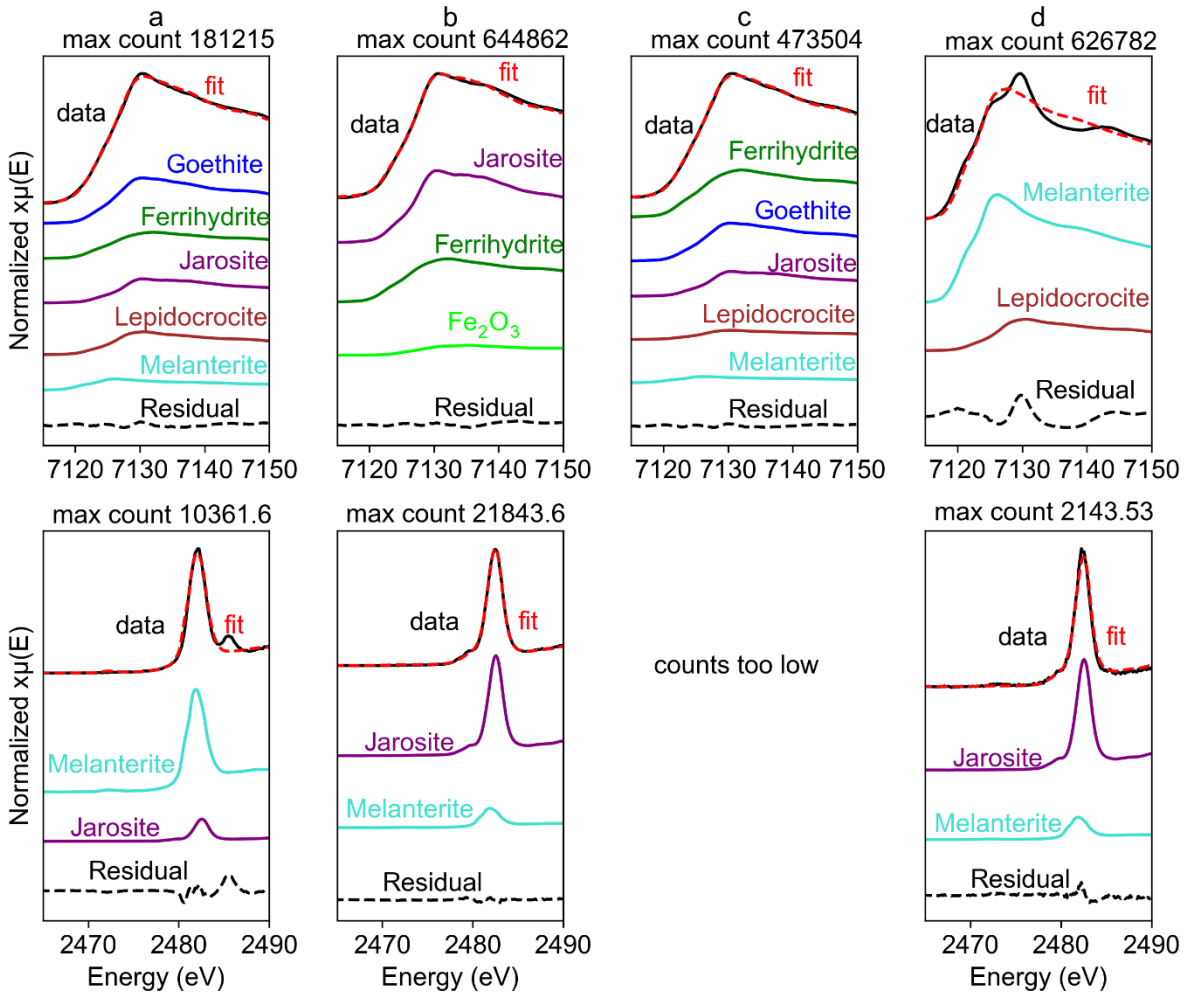

Figure S-F4. Iron μXANES raw linear combination fitting at four spots across Fe(III) oxyhydroxide at 1.65 mbgs of KK4. At point c, counts for S were too low. At point d, counts for S were also an order of magnitude lower than point a and b.

Appendix G

Additional reactive transport simulation results

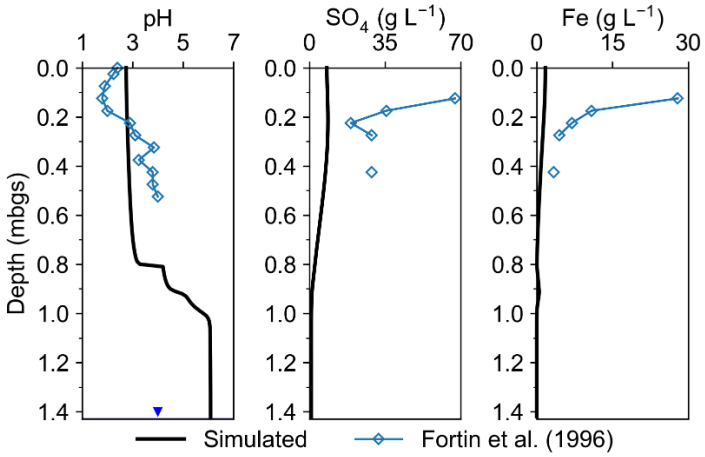

Figure S-G1. Simulated tailings aqueous geochemistry after approximately 24 years compared to field data collected in 1994 from Fortin et al., (1996) under alternative simulation scenario where water table was constantly at the bottom of the tailings.

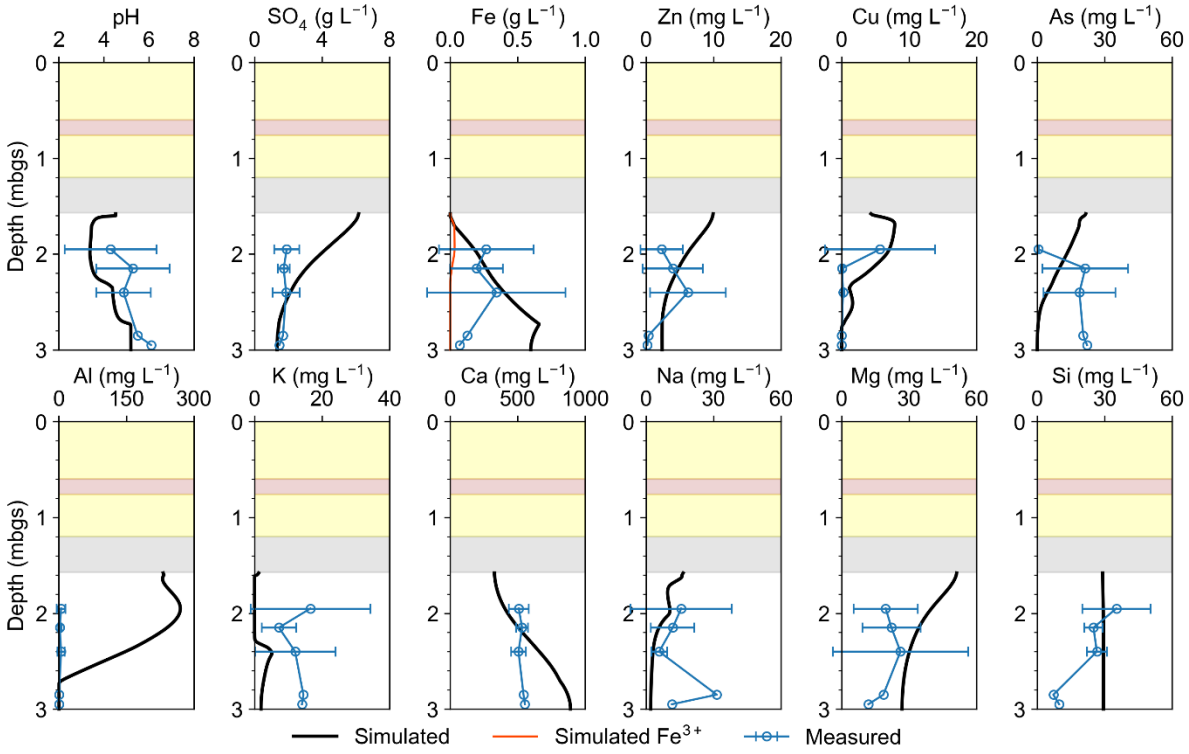

Figure S-G2. Simulated tailings aqueous geochemistry after approximately 50 years (early 2020) under ideal cover condition (0.01% P_{O2}) compared to field results of six sampling events from 2017 to 2021, under alternative scenario where water table was constantly at the bottom of the tailings.

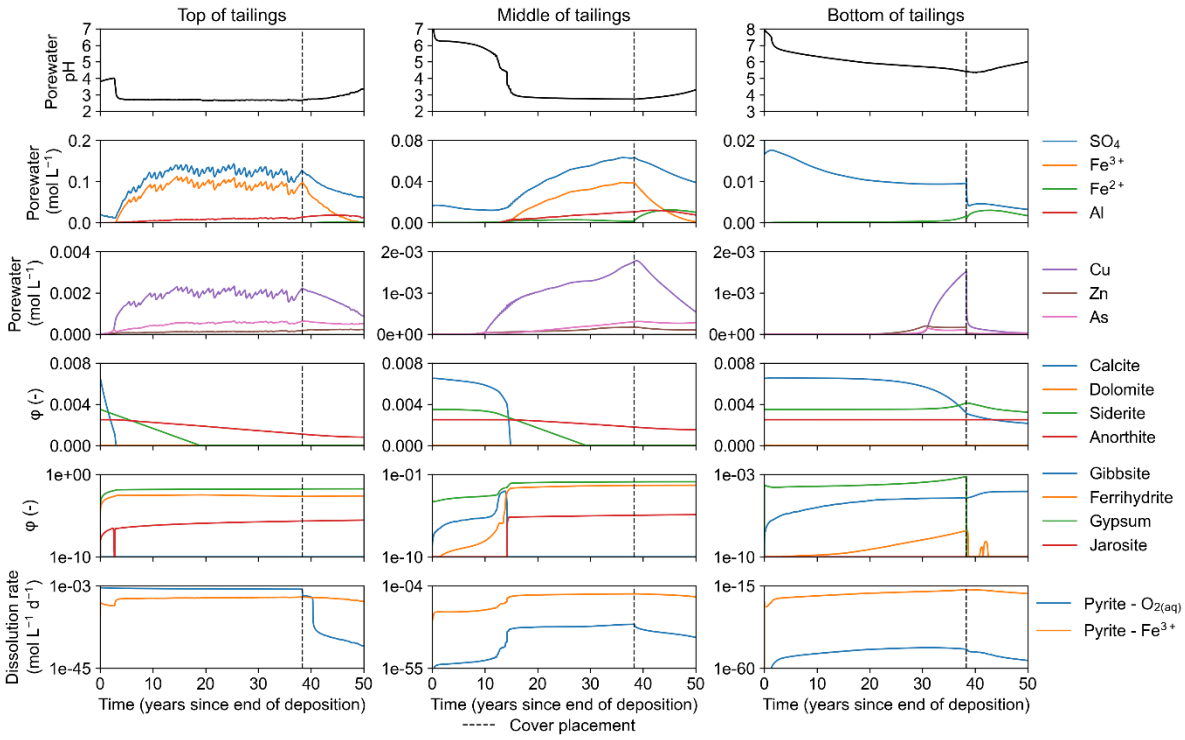

Figure. S-G3. Alteranatively simulated evolution of selected geochemical parameters in the top, middle, and bottom zones of the tailings under a constant temeperature of 5 °C throughout the domain and duration of the simulation.

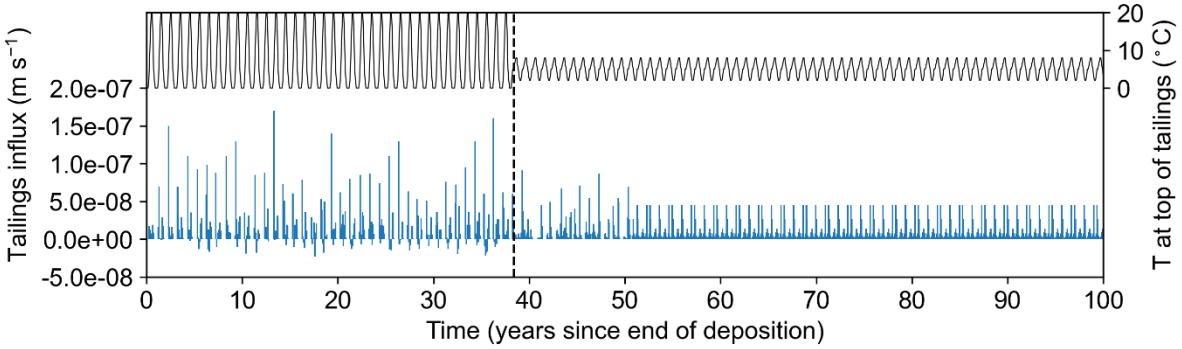

Figure S-G4. Monthly infiltration and temperature from 1970 (year 0) to 2070 (year 100) prescribed at the upper boundary of the future scenario for tailings. The vertical dashed line indicates the time of cover placement.